

國立臺灣大學電資學院電機工程研究所

博士論文

Department or Graduate Institute of Electrical Engineering College of
Electrical Engineering and Computer Science

National Taiwan University

Doctoral Dissertation

多模式小動物影像於腫瘤研究之技術開發與應用

**Techniques and Applications of Multi-modality Small
Animal Imaging in Cancer
Research**



研究生：廖愛禾 (Liao Ai-Ho)

指導教授：李百祺教授

中華民國 九十八年 一 月

Jan 2009

致謝

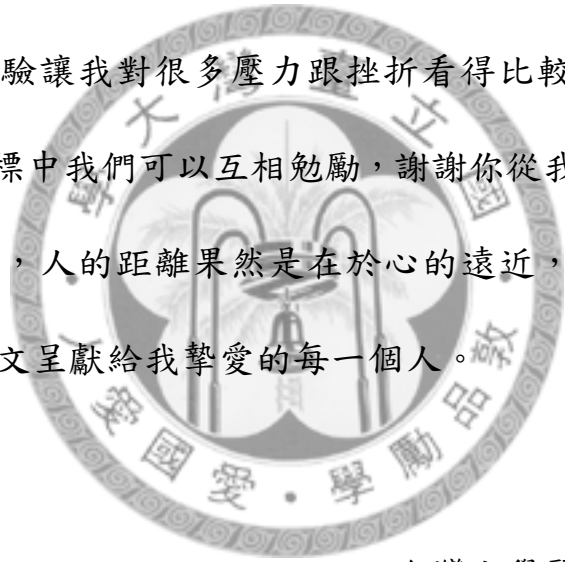
博士班的五年歲月在我優柔寡斷的個性中，心情不斷的翻滾煎熬，終於將要成為記憶的一部份；第一年時初為新鮮人的我只想考好資格考然後每天不停的用超音波量小老鼠腫瘤大小，第二年經歷同年好友的結婚生育潮，開始無力覺得自己倒底該不該繼續求學還是就業，邁入第三年以後正是我最痛苦的時期，畢竟辛苦的研究成果正在自己感到得意時被夢寐以求的國際期刊一次次的拒絕，那種震撼感原來就是失眠的滋味；我在夜闌人靜的時候問自己，你要放棄還是繼續？如果要繼續，就要拿出最堅強的毅力，就在這關鍵的時刻老師給我臨門的一腳(往內踢！)，於是我硬著頭皮留下來；就這樣第四年、第五年很快的度過，不知不覺中也開始有文章被接受，新的研究也慢慢的有了眉目，直到有一天，老師說，你開始找工作吧！

感謝李百祺老師，無論是在專業知識的教導，或是為學處事的方法與態度上，老師豐沛的學識涵養與為人師表的身教最令我們折服，在我們對研究感到力不從心時，老師一直給我們強而有力的後盾。非常感謝黃正仲老師，在研究工作上給我寶貴的協助與建議；感謝鄭文芳醫師和葉秀慧老師，提供我們最好的癌症模式，讓我可以安心的作研究，感謝江惠華老師細心修正論文上的缺點。

研究上的兩個階段最要感謝的是承翰與立言的幫忙，有了你們的

幫助我才可以順利完成許多的研究。此外，許多的學長，諸如秩光、哲州、葉文俊醫師、夢麟與聖文，在研究工作上都給了我許多的指導建議與協助，維寧、振瑋、俊延、珣力、曄琳、慧敏、博文、博冠、乾修以及其他學弟妹們，感謝你們的幫助與陪伴，謝謝你們。

最後要感謝我的父母，自幼及長一路的照顧與培育我，我知道並不是所有的人都能像我一樣這麼幸福的在工作幾年後可以完全辭去工作專心當學生的，再來要感謝在生化所取得博士學位的二姐瓊禾，你以過來人的經驗讓我對很多壓力跟挫折看得比較開，最後感謝賀喬，在相同的目標中我們可以互相勉勵，謝謝你從我博士班第三年開始加入我的生活，人的距離果然是在於心的遠近，終於我們都畢業了！僅將此篇論文呈獻給我摯愛的每一個人。



廖愛禾 謹誌於
台灣大學醫學卓越研究中心
中華民國九十八年一月

摘要

近幾年來，小動物模式被廣泛的運用在臨床前人類疾病治療、基因體研究以及藥物開發等生物醫學領域；在這些研究中，想要立即觀察到效果，非侵入式影像系統便顯得重要，而非侵入式的影像系統中，結合結構性以及功能性兩大類的多重影像系統能同時獲得不同的影像資訊，而使研究觀察層面更加深入及徹底。

本論文主要是結合高頻超音波影像系統以及微正子兩套影像系統，並建立兩者結合時的醫學影像定位方式，以壓克力以及瓊膠分別作為製作植有體表腫瘤的小動物定位固定裝置和仿體的材質，然後在相同定位點位置上，放置六個直徑 0.43~0.60 mm 的玻璃球和 0.1 μl [^{18}F]FDG 核醫藥物在腫瘤上方，作為能同時成像於兩種影像上的定位點；並使用 orthogonal Procrustes algorithm，作為本研究剛體定位的演算法，我們得到的定位點平均誤差為 0.31 mm，並進一步呈現融合影像，最後設計測試仿體，將誤差分為定位點誤差以及標的點誤差來評估實驗結果。

結合這兩套系統在小動物腫瘤研究中，我們以非侵入式的高頻超音波影像系統獲得腫瘤活體內的生長曲線，另一方面在腫瘤生長的每個時期，同時進行微正子造影。本研究使用 [^{18}F]FDG 進行腫瘤功能性微正子造影，所使用之動物腫瘤模式為植有 WF-3 卵巢癌細胞的 C57BL/6J 小黑鼠。在獲得兩種影像資料後，接著進行影像區隔(Tumor Segmentation)以及三維影像重建腫瘤影像並運算體積，最後；由腫瘤的生長曲線獲得腫瘤活體內的體積倍增時間為 7.46 天，此結果我們將與傳統文獻上直接以尺量測腫瘤大小的結果予以比較。而另一方面，我們由腫瘤的微正子造影獲得的核醫藥物放射線比活度曲線獲得腫瘤每週對周遭組織的藥物比率在第五週到達最高，綜合這些資訊，期能提供更多藥物治療癌症時機的資訊。

為了使高頻超音波造影亦具有功能性影像資訊，使兩者影像能不但在結構與功能上互補，亦能比對其功能性的效果，本研究使用自製的高頻超音波對比劑進行肝腫瘤內對比劑的變化週期，以開發高頻超音波影像的功能性影像效果。在這

部分，本研究使用本實驗室團隊研發之高頻率超音波影像系統以及研究團隊所合成的高頻超音波對比劑進行對比劑注射 B 型肝炎基因轉植小鼠超音波造影來診斷肝腫瘤三個血管脈相時期。本研究成功的辨識對比劑注射後腫瘤區塊影像明顯增強的肝腫瘤動脈期以及緊接著門脈期的快速減退，以時間影像強度曲線量化各時期影像強度，並成功的判讀辨識出 13 隻疑似有肝腫瘤病變的 B 型肝炎基因轉植小鼠其肝腫瘤類型、良性或惡性，最後以病理組織切片鑑定結果做為標準，計算高頻超音波對比劑成像結果對偵測小鼠肝腫瘤的靈敏度、特異性以及準確度，提供進入臨床前的小動物肝腫瘤研究良好而準確的鑑定造影工具以及技術，並探討微正子影像與高頻超音波影像的結合在腫瘤研究與技術開發之可行性。

最後，本研究使用整合型經驗模態分解法(Ensemble Empirical Mode Decomposition, EEMD)來增強超音波對比劑影像上對血流灌流區的偵測能力，並加入白色噪音(white noise)方式可以產生濾波的效果，解決模態混合的問題得到模態一致的內建模態函數(Intrinsic Mode Function, IMF)，結果發現原始訊號經過整合型經驗模態分解法運算後產生的部分本質模態函數相較於傳統之脈衝反相(pulse inversion)影像，能提升血流灌流區和周遭組織的對比度(contrast-to-tissue ratio)。本研究以模擬組織與對比劑訊號和實驗影像來實現經驗模態分解法在非線性成像增強的效果，實驗影像架構也適當的修正移動雜訊對於分解過程中雜訊的放大的問題，並期此方法能提升超音波對比劑影像之效能。

本研究以結合高頻超音波影像系統以及微正子兩套影像系統為基礎，未來將延伸建構兩套影像系統結合模式，實現各種影像系統(如磁振掃描、光學冷光、光學螢光、自動放射顯影術)影像資訊結合，以目前開發出之超音波對比劑為基礎，研發多模式影像造影劑，實現多模式腫瘤影像之開發。

關鍵詞：高頻超音波影像系統、微正子斷層掃描小動物影像、三維影像定位、多模式小動物影像、小動物腫瘤、高頻超音波對比劑成像、經驗模態分解法、脈衝反相。

Abstract

Small-animal models are used extensively in disease research, genomics research, drug development, and developmental biology. The development of noninvasive small-animal imaging techniques with adequate spatial resolution and sensitivity is therefore of prime importance. In particular, multimodality small-animal imaging can provide complementary information.

This paper presents a method for registering high-frequency ultrasonic (microUS) images with small-animal positron-emission tomography (microPET) images. Registration is performed using six external multimodality markers, each being a glass bead with a diameter of 0.43–0.60 mm, with 0.1 μl of [^{18}F]FDG placed in each marker holder. A small-animal holder is used to transfer mice between the microPET and microUS systems. Multimodality imaging was performed on C57BL/6J black mice bearing WF-3 ovary cancer cells in the second week after tumor implantation, and rigid-body image registration of the six markers was also performed. The average registration error was 0.31 mm when all six markers were used, and increased as the number of markers decreased. After image registration, image segmentation and fusion are performed on the tumor. Our multimodality small-animal imaging method allows structural information from microUS to be combined with functional information from microPET, with the preliminary results showing it to be an effective tool for cancer research.

In this study, we used a microUS system that we developed in-house as an alternative method for tumor growth calipers. In addition, microUS was combined with small-animal positron-emission tomography (microPET) for tumor metastatic assessment. MicroUS provides anatomical information that can be used for tumor volume measurements while microPET is a functional imaging method with

positron-emitting radiopharmaceuticals, such as ^{18}F -labeled deoxyglucose, [^{18}F]FDG. In this study, microUS and microPET were performed in a mouse tumor longitudinal study (2-8 weeks), both with 3D tumor segmentation and volume measurements. The average tumor volume doubling time as determined during the exponential phase was 7.46 days by microUS. MicroUS and microPET are complementary to each other as microUS has superior spatial resolution and microPET provides functional information such as hypoxia or necrosis in the progression of the tumor. With image registration and fusion, the combination can be a valuable tool for cancer research.

To investigate the feasibility of the functional information which provided from microUS, we used the contrast enhanced ultrasound (CEUS) techniques to characterize liver focal lesions and detect three vascular contrast phases in Hepatitis B virus X (HBx) transgenic mice. Specifically, high-frequency ultrasound liver imaging with albumin-shelled microbubbles was employed to detect three vascular contrast phases and characterize focal liver lesions that developed in thirteen HBx transgenic mice at around 14 to 16 months of age. In the thirteen mice, the arterial phase ranges from 2 to 60 seconds post contrast injection. The time period from 10 to 30 minutes post contrast injection was defined as the parenchyma phase in this study. Comparing the imaging and the pathology results, the sensitivity, specificity and accuracy of CEUS for the detection of malignant focal liver lesion in HBx transgenic mice were 91%, 100% and 92%. To characterize the features of the focal liver lesion and detect the three vascular contrast phases of malignant focal liver lesions, the results were arranged according to the guidelines of European Federation of Societies for Ultrasound in Medicine and Biology. Histopathology investigations confirmed the development of the lesion in these thirteen mice.

Finally, we propose to use a novel technique, called the ensemble empirical mode decomposition (EEMD) for contrast nonlinear imaging, to improve the contrast

in CEUS imaging. Compared with the results based on the traditional nonlinear imaging technique, the new approach obtains improved performance for tissue components removal from the mixed signals effectively and objectively, and provides us with more accurate contrast nonlinear signals.

These results demonstrated that high-frequency CEUS imaging is potentially for characterizing malignant focal liver lesions in mice and is valuable to provide functional information for preclinical study. The CEUS technique can combine with microPET imaging in the future. The combining methods of microUS and microPET multimodality imaging systems could be extended and other imaging modalities (ex: MRI, in vivo bioluminescent imaging, in vivo fluorescent imaging, autoradiography) integrate into these new techniques. The homemade microbubbles could be constructed as a multimodality contrast agent. A multiplicity of ligands may be coupled to microbubbles directly via covalent bonds or indirectly through avidin-biotin interactions. Ultrasonically reflective particles can be complexed to paramagnetics for MR or radionuclide for nuclear or D-luciferin for bioluminescent or fluorescence for microscope multimodal imaging. The new technique provides an alternative method for cancer research in small animal.

Key words : High frequency ultrasound, MicroPET, 3-D reconstruction, Multi-modality small animal imaging, WF-3 ovary cancer, Hepatocellular Carcinoma, Contrast enhanced ultrasound, Empirical mode decomposition, Pulse inversion.

CONTENTS

中文摘要.....	I
ABSTRACT.....	II
CONTENTS.....	III
LIST OF FIGURES	IV
LIST OF TABLES.....	V
CH 1. INTRODUCTION	1
1.1 Multimodality Small Animal Imaging.....	4
1.2 High Frequency Ultrasound Imaging System.....	5
1.3 MicroPET Imaging System.....	7
1.4 Imaging Registration for MicroUS/MicroPET	9
1.5 Basics of Ultrasound Contrast Agents	9
1.6 Contrast-Enhanced Ultrasound of HCC.....	10
1.7 Contrast Improvement in Ultrasound Nonlinear Imaging Using EEMD.....	11
1.8 Scope and Organization of the Dissertation	12
CH 2. A THREE-DIMENSIONAL REGISTRATION METHOD FOR MICROUS/MICROPET MULTIMODALITY SMALL ANIMAL IMAGING.....	14
2.1 Small-Animal Model.....	15
2.2 Registration Phantom and Animal Holder Designed.....	15
2.3 Experimental Setup for MicroPET and MicroUS.....	18
2.4 MicroUS/microPET Data Processing and 3D Reconstruction .	19
2.5 Test Phantom Design and Estimation	23
2.6 Rigid-Body Transformation and Error Estimation	24
2.7 Discussions.....	27

CH 3. NONINVASIVE TUMOR IMAGING WITH HIGH FREQUENCY ULTRASOUND AND MICROPET IN SMALL ANIMALS.....29

3.1 Small-Animal Model.....31

3.2 Small-Animal High-Frequency Ultrasound Imaging31

3.3 Small-Animal MicroPET Imaging.....33

3.4 MicroUS/microPET Data Acquisition, 3D Tumor Reconstruction, and Volume Measurement.....34

3.5 In Vivo Growth Curve.....40

3.6 Discussions.....42

CH 4. CHARACTERIZATION OF MALIGNANT FOCAL LIVER LESIONS WITH CONTRAST-ENHANCED 40 MHZ ULTRASOUND IMAGING IN HEPATITIS B VIRUS X TRANSGENIC MICE: A FEASIBILITY STUDY.....46

4.1 Hepatocellular Carcinomas in Human46

4.1.1 Pathology and Hepatocarcinogenesis46

4.1.2 Unenhanced Sonography48

4.1.3 Contrast Enhanced Sonography48

4.2 Transgenic Mouse Model.....50

4.3 Microbubbles for High-Frequency Ultrasound Imaging51

4.4 Small-Animal High-Frequency Ultrasound Imaging53

4.5 Contrast-Enhanced Ultrasound Imaging at 40 MHz54

4.6 Time–Intensity Curves.....62

4.7 Histopathology.....64

4.8 Characterization of Focal Liver Lesion64

4.9 Discussions.....65

CH 5. CONTRAST IMPROVEMENT IN ULTRASOUND

NONLINEAR IMAGING USING EEMD.....	68
5.1 Empirical Mode Decomposition.....	71
5.2 Ensemble Empirical Mode Decomposition.....	72
5.3 Simulation.....	73
5.4 Experiments.....	77
5.5 Denoising.....	82
5.6 Discussions.....	83
CH 6. CONCLUSIONS AND FUTURE WORKS.....	90
6.1 MicroUS/MicroPET Multimodality Small Animal Imaging ...	90
6.2 Feasibility of Using Contrast-Enhanced 40 MHz Ultrasound Imaging to Characterize Hepatocellular Carcinomas in Small Animal.....	91
6.3 Future Works.....	92
6.3.1 Applications of the Three-Dimensional Registration Method for MicroUS/MicroPET Multimodality Small Animal Imaging.....	92
6.3.2 Microbubbles for Therapeutic Application in Hepatocellular Carcinomas.....	92
6.3.2.1 Production of Anticancer Microbubbles.....	94
6.3.2.2 Potential of Multimodality Microbubbles.....	94
6.3.3 Evaluation Blood Flow Changes with Contrast Enhanced 40 MHz Ultrasound in HBx Transgenic Mice.....	95
REFERENCES.....	97
APPENDIX.....	110
Positron Emission and Annihilation.....	110
MicroPET Image Processing.....	111

A-1 Ordered Subsets Expectation Maximization (OS-EM) . 111
A-2 Filtered Back Projection (FBP) 112
Histology of Liver Focal Lesion in HBx Transgenic Mice 114

PUBLICATION LIST 115



LIST OF FIGURES

Fig. 1-1 Estimated number of new cancer cases by world area, 2007.....	1
Fig. 1-2. The wealth of multi-modality imaging techniques currently available for studying various aspects of cancer.....	3
Fig. 1-3. MicroUS system block diagram.....	6
Fig. 1-4. Pulse-echo imaging processing.....	6
Fig. 1-5. Positron annihilation and coincidence detection in a PET camera	8
Fig. 1-6. A photograph of the Concorde microPET R4 system installed at the Taipei Veterans General Hospital.	8
Fig. 1-7. A diagram of the home-made microbubble used in this study.	10
Fig. 2-1. Schematic (a) and photograph (b) of the registration phantom and the small-animal holder	17
Fig. 2-2. Flow chart of the procedure for constructing the registration phantom.....	17
Fig. 2-3. Flow chart of microUS/microPET image acquisition and processing	19
Fig. 2-4. Making the voxel size the same in the two imaging systems.....	20
Fig. 2-5. 3D image reconstruction using Amira software: (a) selection of central slices for the three orientations, and (b) detection of the contours of the tumor boundary (white).....	21
Fig. 2-6. MicroUS (a) and microPET (b) transverse (top), sagittal (middle), and coronal (bottom) images of the tumor region with the registration markers. (c) The microUS/microPET fused images.....	22
Fig. 2-7. 3D reconstruction of the tumor (bottom) and the six registration markers (top) for (a) microUS, (b) microPET, and (c) microUS (white blobs)/microPET (dark blobs) fused images after registration. The three projection images are shown in (d)	22
Fig. 2-8. Design of the test phantom containing six markers. The phantom consisted of a graphite-agarose region and an agarose region. The glass capillary tube was held within the graphite-agarose region. Each region contained three markers.....	23

Fig. 2-9. Geometry of the transformation matrix.....	25
Fig. 2-10. FRE and TRE values as functions of the number of markers used in registration	26
Fig. 3-1. MicroUS system block diagram.....	32
Fig. 3-2. MicroUS/microPET image acquisition and processing	34
Fig. 3-3. 3D image reconstruction using Amira software: (a) selection of central slices for the three orientations in microPET, and (b) detection of the contours of the tumor boundary (red). (c) selection of central slices for the three orientations in microUS, and (d) detection of the contours of the tumor boundary (red).....	35
Fig. 3-4. (a) Parenchyma of a tumor at the 8th week after tumor implantation. (b) B-mode microUS image (left, partial transverse section), tumor segmentation (middle), and the corresponding 3D representation (right) at the 8th week. (c) MicroPET image (left, whole-body transverse section), tumor segmentation (middle), and the corresponding 3D representation (right) of the 8th-week tumor	37
Fig. 3-5. Time–activity curves obtained by microPET of [¹⁸ F]FDG for C57BL/6J mice bearing WF-3 mouse ovarian carcinoma	38
Fig. 3-6. In vivo tumor growth curve by microUS and vernier caliper. Means and standard deviations are shown	39
Fig. 3-7. 3D tumor volume reconstruction by microPET imaging based on the radioactivity	42
Fig. 4-1. The features of HCC development.....	47
Fig. 4-2. Ultrasound B-mode images of the region in the agarose phantom containing albumin-shelled microbubbles using ultrasound at 50 MHz (a), 40 MHz (b), 25 MHz (c), and 20 MHz (d)	52
Fig. 4-3. Block diagram of the 40 MHz ultrasound imaging system.....	53
Fig. 4-4. Protocol for CEUS imaging of HBx transgenic mice	54
Fig. 4-5. Regions of interest (ROIs) were selected in the suspected focal lesions (a), vessels within the lesions (b), and liver parenchyma (c)	55
Fig. 4-6. Hypervascular metastases lesion in mouse 2 before contrast injection (a), at	

19 seconds (b), at 61 seconds (c), and 2 minutes (d) after contrast injection 58

Fig. 4-7. Hypervascular metastases lesion in mouse 2 before contrast injection (a) and at 2 minutes (b) and 30 minutes (c) after contrast injection. Arrows point to margins of lesion enhancement as clearly evident at 30 minutes after contrast injection. Box indicates the vessels in the hypervascular metastases lesion. Panel (d) shows the anatomy of the hypervascular metastases lesion after fixation in 10% formalin 58

Fig. 4-8. Images of HCC lesion in mouse 5 before contrast injection (a) and at 14 seconds (b), 16 seconds (c) and 2 minutes (d) after contrast injection. Panels (c) and (d) show the characteristics of chaotic vessels. Panel (d) shows the histology result of the HCC lesion..... 59

Fig. 4-9. HCC lesion in mouse 6 before contrast injection (a) and the hyper-enhancing feature during the arterial phase (b). Panel (c) shows the hypo-enhancing feature at 30 minutes after contrast injection..... 59

Fig. 4-10. The hypovascular metastases lesion in mouse 9 before contrast injection is shown in panel (a). Panel (b) shows the hyper-enhancing, rim enhancing, and non-enhancing (necrosis) features during the arterial phase. Panel (c) is the hypo-enhancing feature at 30 minutes after contrast injection..... 59

Fig. 4-11. HCC lesion in mouse 13 before contrast injection (a) and the hyper-enhancing feature during arterial phase (b) 60

Fig. 4-12. The focal nodular hyperplasia (FNH) lesion in mouse 11 before (a) and after (b) contrast injection..... 60

Fig. 4-13. Mean TICs of the focal liver lesions in the ten male mice were drawn within 90 seconds after contrast injection. The baseline value was calculated by the mean value of the baseline image from the ten mice. The arterial phase was defined as the time period that the image intensity increases and recovers to the baseline... 63

Fig. 4-14. This figure shows that the mean contrast between focal lesion and liver parenchyma reached the maximum at 30 minutes after contrast injection. During 10 to 30 minutes, the slope increases and is defined as the late phase in this study..... 63

Fig. 4-15. This figure shows the mean image intensity of vessels in focal lesion in

mouse 2, 5, 7, 10 within 30 minutes after contrast injection. The image intensity increases within 30 minutes 64

Fig. 5-1. Original tissue harmonic and 1-5 IMFs components of simulated PI signals (left column). Original tissue-microbubble mixed harmonic and 1-5 IMFs components of PI simulated signals (right column)..... 75

Fig. 5-2. (a) shows the spectra from the original tissue harmonic (solid line) and tissue-microbubble mixed (dashed line) simulated PI signals. (b) shows the spectra from 2 IMFs component. All amplitudes were normalized to the focal fundamental amplitudes in tissue and tissue-microbubble mixed PI signals..... 76

Fig. 5-3. Schematic diagram of the experimental setup for measurement of M-mode harmonic signal..... 78

Fig. 5-4. (a) M-mode PI images and axial projections in fundamental mode, all 5 IMFs were extracted with EMD algorithm. (b) M-mode PI images and axial projections in second harmonic mode, all 5 IMFs were also extracted with EMD algorithm..... 79

Fig. 5-5. (a) M-mode PI images and axial projections in fundamental mode, all 5 IMFs were extracted with de-noising EEMD algorithm. (b) M-mode PI images and axial projections in second harmonic mode, all 5 IMFs were also extracted with de-noising EEMD algorithm..... 80

Fig. 5-6. (a) Comparison of CTR values in M-mode PI images by PI fundamental (1 IMF) and PI second harmonic (1 IMF) and groups with EMD algorithm. (b) Comparison of CTR values in M-mode PI images by PI fundamental (1 IMF) and PI second harmonic (3 IMF) and groups with EEMD algorithm..... 81

Fig. 5-7. (a) Comparison of CTR and CNR improvement values in PI M-mode images in fundamental mode with EMD algorithm. 1-5 IMFs were extracted with EMD algorithm. (b) Comparison of CTR and CNR improvement values in PI M-mode images in fundamental mode with EEMD algorithm. 1-5 IMFs were extracted with EEMD algorithm..... 82

Fig. 5-8. (a) Comparison of CTR and CNR improvement values in PI M-mode images

in second harmonic mode with EMD algorithm. 1-5 IMFs were extracted with EMD algorithm. (b) Comparison of CTR and CNR improvement values in PI M-mode images in second harmonic mode with EEMD algorithm. 1-5 IMFs were extracted with EEMD algorithm..... 82

Fig. 5-9. With EMD, original tissue harmonic and 1-5 IMFs components of conventional simulated signals are shown in left column. Original tissue-microbubble mixed harmonic and 1-5 IMFs components of conventional simulated signals are shown in right column 83

Fig. 5-10. With EEMD, original tissue harmonic and 1-5 IMFs components of conventional simulated signals are shown in left column. Original tissue-microbubble mixed harmonic and 1-5 IMFs components of conventional simulated signals are shown in right column 84

Fig. 5-11. With EMD, original tissue harmonic and 1-10 IMFs components of conventional simulated signals added uniform noise are shown in left column. Original tissue-microbubble mixed harmonic and 1-10 IMFs components of conventional simulated signals added uniform noise are shown in right column 85

Fig. 5-12. With EEMD, original tissue harmonic and 1-10 IMFs components of conventional simulated signals added uniform noise are shown in left column. Original tissue-microbubble mixed harmonic and 1-10 IMFs components of conventional simulated signals added uniform noise are shown in right column 86

Fig. 6-1. Destruction of microbubbles by ultrasound 93

Fig. 6-2. Capillary rupture by microbubble expansion in the ultrasound field..... 94

Fig. 6-3. Conception of anticancer-drug enclosed by microbubble..... 94

Fig. A-1. Projections generated from a single central point source (3 projections shown).....113

Fig. A-2. HCC lesion in mouse 6 before contrast injection (a) and the hyper-enhancing feature during the arterial phase (b). Panel (c) shows the hypo-enhancing feature at 30 minutes after contrast injection. (d) shows the histology result.....114

Fig. A-3. The hypervascular metastases lesion in mouse 9 before contrast injection is

shown in panel (a). Panel (b) shows the hyper-enhancing, rim enhancing, and non-enhancing (necrosis) features during the arterial phase. Panel (c) is the hypo-enhancing feature at 30 minutes after contrast injection. (d) shows the histology result.....114



LIST OF TABLES

Table 1-1. Sensitivity, spatial resolution and clinical translation of molecular-functional imaging modalities.....	2
Table 2-1. FRE values after image registration	26
Table 2-2. FRE and TRE values for the test phantoms (means from all six markers)	26
Table 3-1. Tumor volumes and radioactivity measurements	39
Table 3-2. Characteristics of microUS and microPET imaging modalities.....	45
Table 4-1. Characterization of focal liver lesions according to the guidelines of EFSUMB (E: Enhancement).....	61
Table A-1. Properties of commonly used positron emitting radio-isotope	110



CH 1. INTRODUCTION

Cancer is a disease caused by normal cells changing so that they grow in an uncontrolled way. The uncontrolled growth causes a lump called a tumor to form. There are over 200 different types of cancer because there are over 200 different types of body cells. One in eight deaths worldwide is due to cancer. Cancer is the second leading cause of death in economically developed countries (following heart diseases) and the third leading cause of death in developing countries [1]. Figure 1-1 shows that there will be more than 12 million new cancer cases in 2007 worldwide, of which 5.4 million will occur in economically developed countries and 6.7 million in economically developing countries. By 2050, the global burden is expected to grow to 27 million new cancer cases and 17.5 million cancer deaths simply due information on survival.



Fig. 1-1 Estimated number of new cancer cases by world area, 2007.

(American Cancer Society, http://www.cancer.org/downloads/STT/Global_Cancer_Facts_and_Figures_2007_rev.pdf)

Prevention, early diagnosis and treatment are the three broad challenges for cancer. The early diagnosis of cancer improves the prognosis for treatment. Medical and diagnostic imaging equipment includes MRI, PET, ultrasound and CT scans that allow us to diagnose cancer and plan medical treatment for the patient. Early diagnosis has also made a significant contribution to the reduced number of deaths from cancer. It provides a greater chance that treatment will be successful [2]. The early-diagnosis technique requires high sensitivity and specificity. To the purpose, a combined molecular–functional–anatomic approach will provide the highest benefit and would probably require a combination of multiple imaging modalities because each has its own strengths and weaknesses (Table 1-1).

Table 1-1. Sensitivity, spatial resolution and clinical translation of molecular-functional imaging modalities.

Imaging modality	Sensitivity of detection in MFI	Spatial resolution <i>in vivo</i>	Advantages	Disadvantages
CT	500 micromolar (Gd-DTPA)–low millimolar (Iodine) range	>10 μm	High spatial resolution	Patients are exposed to radiation
MRI	T_2 -contrast, iron oxide nano-particles: nanomolar–micromolar range	4 μm (experimental MRI), 250 μm in plane (clinical MRI)	High spatial resolution	Particle size is often large, which restricts <i>in vivo</i> delivery
	T_1 -contrast, multilabeled targeted Gd-DTPA macromolecules: >10 μM	4 μm (experimental MRI), 250 μm in plane (clinical MRI)	High spatial resolution	Particle size of contrast agent or reporters is relatively large
MRS	Millimolar range (^1H at 4.7–11 Tesla)	≥ 0.5 cm (3 Tesla), 0.7 cm (1.5 Tesla)	Detection of endogenous metabolites	Low sensitivity results in low spatial resolution
Optical	Nanomolar range: ≥ 50 cells (fluorescence); ≥ 1000 cells (bioluminescence)	>25 μm , intravital microscopy: 1–15 μm	High sensitivity, high spatial resolution	Restricted depth detection
PET	Picomolar range	≥ 1 mm (microPET), ~ 4 –5 mm (clinical PET)	High sensitivity, short-lived isotopes	Low spatial resolution, cyclotron required for generating some isotopes
SPECT	Picomolar range	>1 mm (microSPECT), ≥ 3 mm (clinical SPECT)	High sensitivity	Low spatial resolution, long-lived isotopes
Ultrasound	$>10^8$ microbubbles per ml blood	>40 μm	High spatial resolution, cost effective	Few probes available

For example, Positron Emission Tomography/Computed Tomography (PET-CT) helps physicians provide an accurate and automatic diagnosis for the staging and treatment of cancer. It is to be able to successfully treat cancer, and several promising molecular-targeted therapies are already being tested in the clinic [3]. Create a useful imaging modality with greater accuracy for cancer detection is very important. Figure 1-2 shows examples of imaging modalities and their ability to image processes ranging from the subcellular level up to intact tissue in vivo [2].

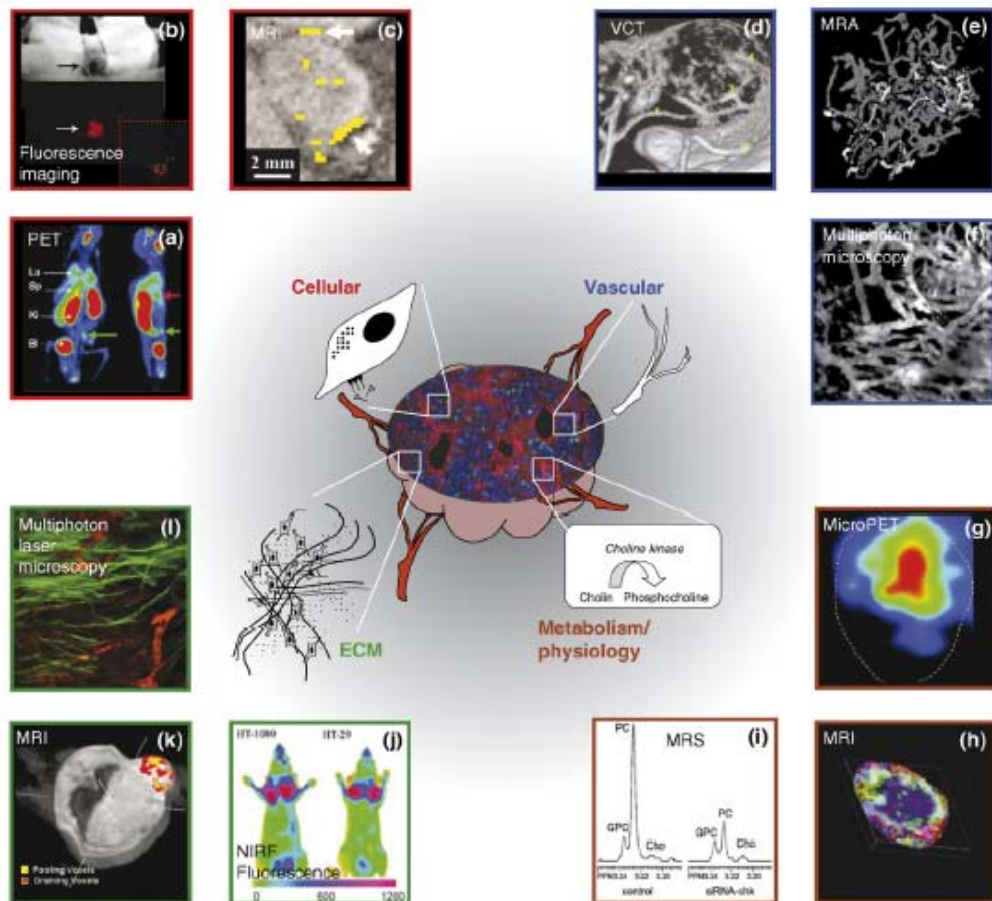


Fig. 1-2. The wealth of multi-modality imaging techniques currently available for studying various aspects of cancer.

1.1 Multimodality Small Animal Imaging

Small-animal models are used extensively in disease research, genomics research, drug development, and developmental biology [4], which has resulted in the evolution of many clinical imaging modalities in recent years for imaging small laboratory animal models [5]. For example, small-animal positron-emission tomography (microPET) and single-photon-emission tomography have become essential tools for evaluating new therapeutic approaches in animal models of human disease [6]. A combined positron-emission tomography (PET)/computed tomography scanner has also triggered substantial interest in the noninvasive imaging of small laboratory animals [7]. These noninvasive imaging techniques can be divided into two categories: structural imaging and functional imaging. Combining these two types of imaging methods (i.e., multimodality imaging) can provide complementary information that is especially beneficial to cancer research [8]. In this dissertation, a method for registering high-frequency ultrasonic (microUS) images with small-animal positron-emission tomography (microPET) images is presented. MicroUS and microPET were also performed in a mouse tumor longitudinal study, both with 3D tumor segmentation and volume measurements.

1.2 High Frequency Ultrasound Imaging System

High frequency ultrasound refers to the frequency range higher than 20 MHz [9]-[11]. High frequency ultrasonic micro-imaging (microUS) is an important tool for obtaining non-invasive real-time images of small animals. A spatial resolution of less than 100 μm can be achieved when high-frequency ultrasound is used. The center frequency used in this study was 40 MHz and the corresponding spatial resolution is around 75 μm at the focus [12]. MicroUS system has been applied to imaging the eye and skin. It has also been used in anatomical and hemodynamic studies on small animals, such as mouse development from the early embryonic period to adulthood, *in vivo* transgenic mouse disease models, and image-guided interventions on mice. Three dimensional (3D) microUS imaging and segmentation were reported and shown to be a reliable tool in the early detection and longitudinal growth analysis of xenograft tumor in mice. Figure 1-3 shows a block diagram of the microUS system briefly. B-mode ultrasound image was displayed in this study. The pulse echo signal processing is showed in Fig. 1-4. In Fig. 1-4, the ultrasonic impulse signal propagates into the object and reflected by the differences in acoustic impedance. The received signal is also converted into an electrical signal. Typically, only the envelope of the received signal is displayed and demodulated down to baseband. The demodulated signal is selected by low pass filter and converted into the dB data. For B-mode images, a two-dimensional image consists of many one-dimensional dB data signals.

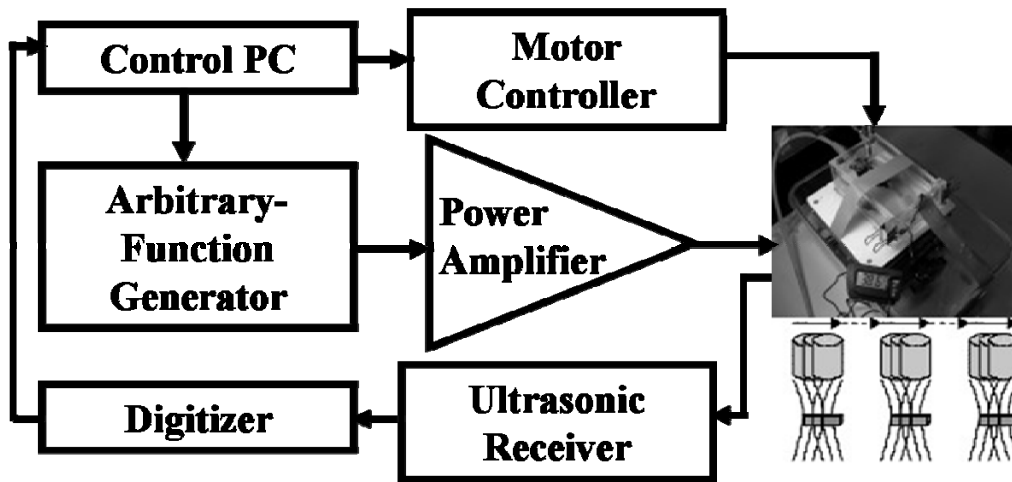


Fig. 1-3. MicroUS system block diagram.

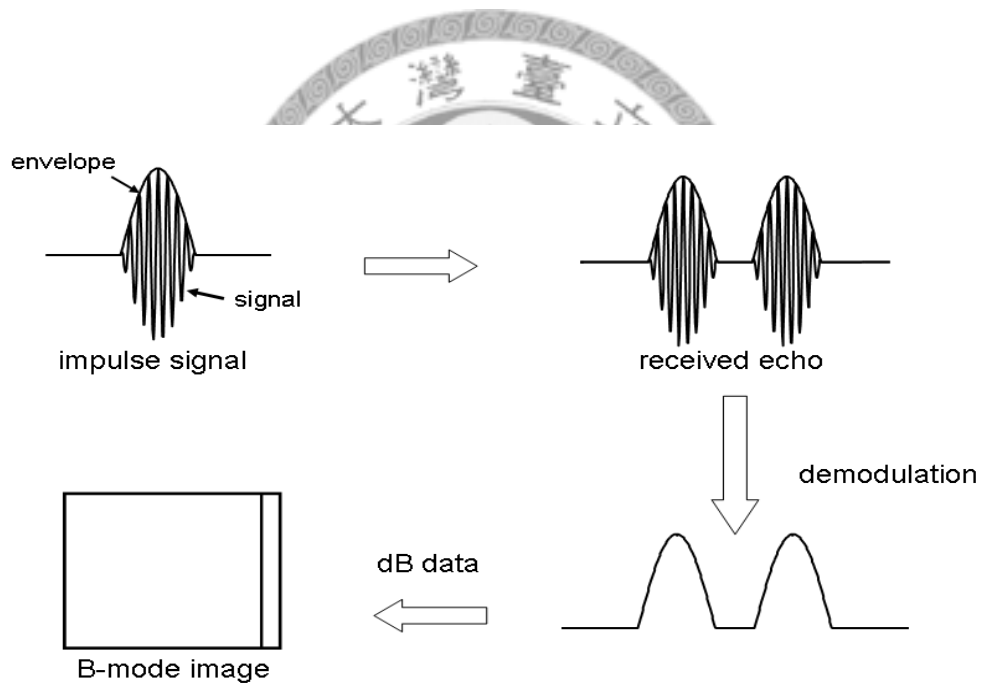


Fig. 1-4. Pulse-echo imaging processing.

1.3 MicroPET Imaging System

Positron-emission tomography (PET) provides 3D distribution of positron-emitting radiopharmaceuticals. Using radiolabeled biomolecules and kinetics models, PET can be used for quantitative measurements of many metabolic functions in living animals, such as brain, heart and tumors. PET requires radioactive tracers to generate annihilation photons signals which are detected by instrumentation. The theory of PET is described in Fig. 1-5. In Fig. 1-5, positron-emitting radioisotopes have an excess of protons. This unstable state ends once the excess positron (β^+) is emitted. It travels a certain distance (1-3 mm) before it undergoes an annihilation with an electron (β^-) creating a pair of collinear gamma rays. While the emitted positrons travelling in tissue, a positron loses energy in collisions with atomic electrons. It eventually annihilates with an atomic electron, resulting in the emission of two 511 keV photons leaving in opposite directions. In a PET camera, each detector generates a timed pulse when it registers an incident photon. These pulses are then combined in coincidence circuitry, and if the pulses fall within a short time-window, they are deemed to be coincident (Fig. 1-5).

For small animal studies, microPET [13]-[14] was designed with improved spatial resolution over clinical PET. The spatial resolution of microPET used in this study (R4, Concord Microsystems, Knoxville, TN, USA) is about 1.8 mm at the center of the field of view and dropped to 2.5 mm (radial component) at 25 mm off-center. Such resolution is inferior to that of microUS. Although microPET is unable to obtain anatomical information of small animals, it is an ideal tool for assessing tumor metabolism. The microPET R4 has a detector material for both scanner models LSO. The ring diameter is 148 mm and the axial FOV is 80 mm. Photograph of the microPET R4 scanner is shown in Fig. 1-6.

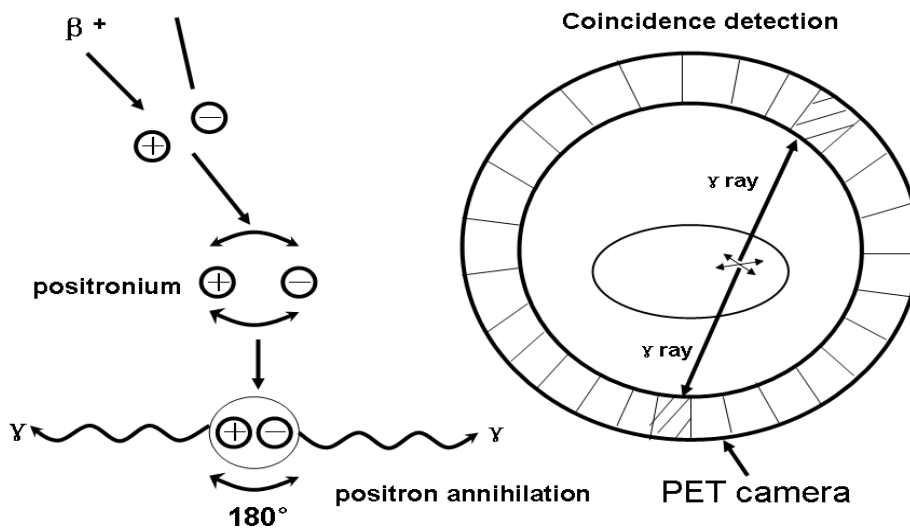


Fig. 1-5. Positron annihilation and coincidence detection in a PET camera.

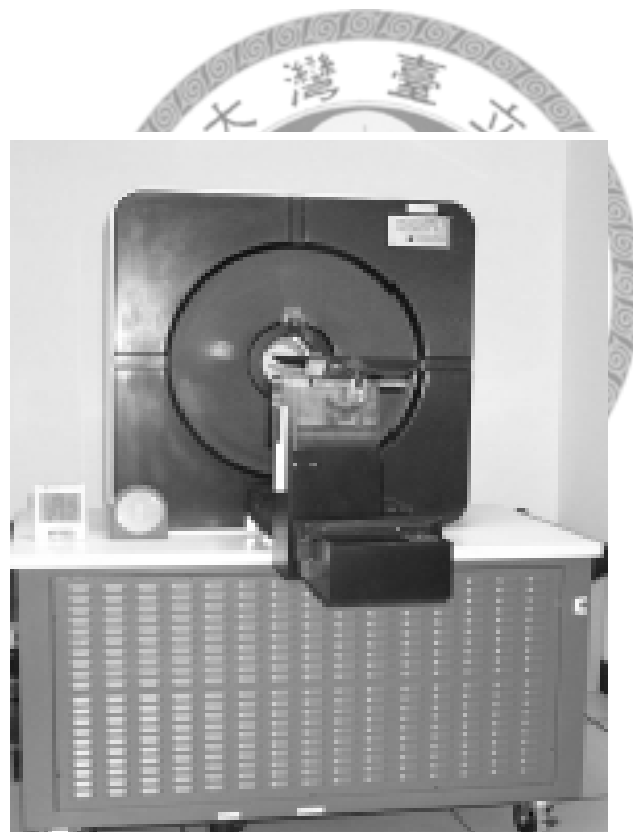


Fig. 1-6. A photograph of the Concorde microPET R4 system installed at the Taipei Veterans General Hospital.

1.4 Imaging Registration for MicroUS/MicroPET

Image registration refers to bringing two or more sets of image data into geometric congruence through spatial transformation [15], and is a necessary step prior to performing image fusion. In order to transform the source to match the reference, it is necessary to determine a mapping from each voxel position in the reference to a corresponding position in the source [16]-[19]. The present study employed rigid-body transformation [20] combined with a multimodality phantom containing six image markers. These six markers were matched in the microUS and microPET images using three image processing steps: (1) making the voxel size the same in the two imaging systems, (2) rigid-body image registration, and (3) fusing the images from the two systems.

1.5 Basics of Ultrasound Contrast Agents

The clinical use of ultrasound contrast agent started in the 1960s, the microbubble enhancement after injection of indocyanine into a cardiac catheter during M-mode scanning of the aortic valve was observed by Gramiak and Shah [21]. In 1984, a method of producing smaller bubbles with a reasonably narrow size distribution was developed. The principal characteristic of microbubble-based ultrasound contrast media is their backscatter effect. Many contrast agents are either air-filled or contain gases that dissolve poorly in the blood with a mean diameter on the order of 1 to 10 μm . The high echogenicity feature of microbubbles is useful in increasing the backscattered signal intensity (15-20 dB) from blood. Moreover, the echogenicity of a contrast media, or degree of backscatter, is dependent on the medium's scattering strength. This can be expressed in terms of a parameter known as its scattering cross section: an index of the efficiency of a scattering medium defined as the power

scattered from a single source (bubble) divided by the intensity of the incident ultrasound.

In this dissertation, home-made microbubble coated with albumin is similar to the commercial ultrasound contrast media, OptisonTM. The gas enclosed in the microbubbles is perfluoropropane (C_3F_8). The microbubbles are in the mean size of $1.2 \mu m$ in diameter. Figure 1-7 shows the diagram of the microbubble composition used in this study.

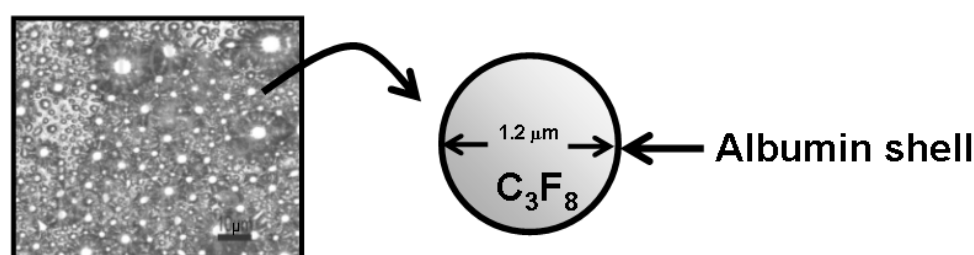


Fig. 1-7. A diagram of the home-made microbubble used in this study.

1.6 Contrast-Enhanced Ultrasound of HCC

Contrast-enhanced ultrasound (CEUS) has been used to evaluate known or suspected focal liver lesions. In this technique, the contrast between the lesion and normal liver parenchyma was evaluated during three vascular contrast phases, i.e. arterial, portal-venous and late phase [22]. Hepatocellular carcinoma (HCC) is a primary liver malignancy in humans that most often occurs in association with cirrhosis or chronic hepatitis [21]. The portal vein carries most (75%) of the afferent blood volume in the normal liver, where HCC results in cirrhosis-induced arterial neoangiogenesis [23] and thus hypervascularity. The increased arterial supply in HCC is proportional to its size and grade. In contrast, the blood supply of the portal vein decreases during the early steps of carcinogenesis [24]-[25]. CEUS imaging plays an

important role in the clinical diagnosis of this disease, providing information on the hemodynamic changes of the HCC and aiding detection of the blood supply peculiar to HCC. The real-time scanning capabilities of ultrasound also allow the evaluation of small lesions that are unclear on computed tomography or magnetic resonance imaging [26]-[27]. Previous studies have found that HCC can be characterized by rapid intensity enhancement in the arterial phase (15–25 seconds after contrast injection), a rapid washout in the portal phase (45–90 seconds after contrast injection), and intensity enhancement of liver parenchyma in the parenchyma phase (90–240 seconds after contrast injection) [21].

1.7 Contrast Improvement in Ultrasound Nonlinear Imaging Using EEMD

Ultrasound harmonic imaging with contrast agents takes the advantage of the nonlinear response of the contrast agent. However, the contrast-to-tissue ratio (CTR) is still limited because significant harmonic echoes are also present in surrounding tissues. Hilbert-Huang transform (HHT) is a data analysis designed specifically for analyzing nonlinear and non-stationary data. Ensemble empirical mode decomposition (EEMD) method is a new part of HHT which allows decomposing the non-stationary, nonlinear data into a finite number of intrinsic scale modes accurately. In this paper, we propose EEMD as an alternative technique for ultrasound contrast imaging, to extract the contrast agent components from the harmonic echoes. Compared to the significantly better contrast detection than fundamental and second harmonic imaging obtained using pulse-inversion (PI) based nonlinear imaging, the CTRs in fundamental and second harmonic bands are improved by 5.2 and 6.5 dB after EEMD decomposing. The contrast-to-noise ratio (CNR) is improved by 9 dB in fundamental

band after EEMD decomposing. The new approach obtains improved performance for contrast agent components extracts either in fundamental band or in second harmonic band.

1.8 Scope and Organization of the Dissertation

The purpose of this dissertation is to investigate performance and relevant issues of ultrasound multimodality tumor imaging in small animal. The feasibility of contrast enhanced 40 MHz ultrasound to characterize hepatocellular carcinoma in small animal is also demonstrated. Three major topics are discussed in this dissertation.

In chapter 2, the potential of three-dimensional registration method for microUS/microPET multimodality small animal imaging is explored. In this chapter, rigid body registration is performed using six external multimodality markers, each being a glass bead placed in each marker holder for microUS, with 0.1 μl of [^{18}F]FDG placed in each marker holder for microPET. Multimodality imaging was performed on C57BL/6J black mice bearing WF-3 ovary cancer cells in the second week after tumor implantation, and rigid-body image registration of the six markers was also performed. Section 2.1 introduces the small animal model used in this study. The registration phantom and small animal holder design is illustrated in section 2.2. In section 2.3, the experimental procedure is described. Data processing and three-dimensional image reconstruction is demonstrated in section 2.4. The test phantom design and estimation for the registration method is described in section 2.5. Section 2.6 introduces the rigid body registration algorithm used in this study and the error estimation of this registration method. The brief concludes in section 2.7.

In chapter 3, the microUS/microPET tumor imaging was applied for long term observation in small animal. The tumor growth was observed by microUS and

microPET system at the same stage. Chapter 4 introduces the feasibility of the contrast enhanced ultrasound technique applied for liver focal lesion characterization in small animal model. Chapter 5 evaluates EEMD method for contrast improvement in nonlinear imaging. Chapter 6 includes the overall discussion and future works of this dissertation.



CH 2. A THREE-DIMENSIONAL REGISTRATION METHOD FOR MICROUS/MICROPET MULTIMODALITY SMALL ANIMAL IMAGING

The present study combined high-frequency ultrasound imaging, which provides real-time and high-resolution anatomical information, with microPET, which provides functional information. An effective registration method is necessary since it is difficult to perform both imaging procedures simultaneously with a known geometry relationship between them. In addition, the fundamental differences in the information provided by ultrasonic imaging and PET require external multimodality markers to the small animal to be used for registration, rather than a mutual information approach [28]. Such multimodality markers need to be both acoustically and radioactively active.

High-frequency ultrasound (microUS) imaging is an emerging tool that employs frequencies above 20 MHz to provide resolutions of less than 100 μm , and has been applied to imaging the eye and skin [29]-[31]. It has also been used in anatomical and hemodynamic studies on small animals, such as mouse development from the early embryonic period to adulthood, *in vivo* transgenic mouse disease models, and image-guided interventions on mice [9]-[11]. The present study combined ultrasound with microPET, which was used to obtain the three-dimensional (3D) distribution of positron-emitting isotopes with an improved spatial resolution relative to clinical PET [13].

Image registration refers to bringing two or more sets of image data into geometric congruence through spatial transformation [15], and is a necessary step prior to

performing image fusion. In order to transform the source to match the reference, it is necessary to determine a mapping from each voxel position in the reference to a corresponding position in the source [16]-[18]. The present study employed rigid-body transformation [19] combined with a multimodality phantom containing six image markers. These six markers were matched in the microUS and microPET images using three image processing steps: (1) making the voxel size the same in the two imaging systems, (2) rigid-body image registration, and (3) fusing the images from the two systems. The orthogonal Procrustes algorithm [32] was used for rigid-body transformation, with the “fiducial registration error” (FRE) and the “target registration error” (TRE) used to quantify the registration precision. Finally, the tumors in the images were segmented for the reconstruction of 3D volume data.

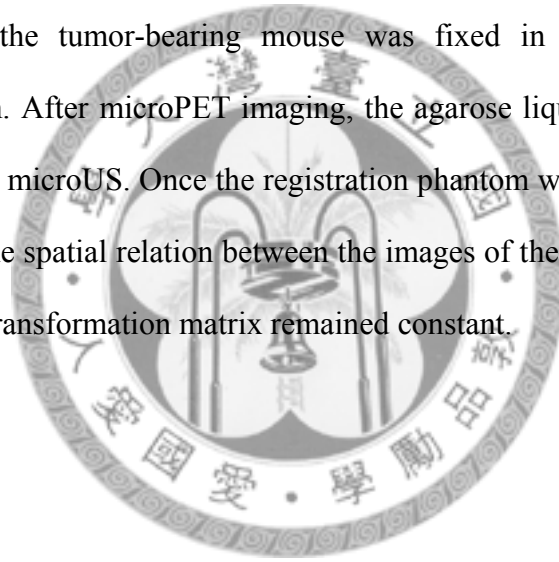
2.1 Small-Animal Model

C57BL/6 mouse peritoneal cells were collected and transfected with the HPV-16 E6 and E7 and activated human c-Ha-*ras* gene. This tumor cell line has been named WF-3 [33]. In this study, female C57BL/6J black mice were anesthetized using ether, and WF-3 cells (5×10^4 in 0.1 ml of phosphate-buffered saline) were injected subcutaneously into the right shoulder of each animal. MicroUS and [^{18}F]FDG microPET imaging were subsequently performed during the second week after injection.

2.2 Registration Phantom and Animal Holder Designed

A registration phantom with six markers was designed so that it could be placed in a small-animal holder, as shown in Fig. 2-1. The small-animal holder was 80×80×40 mm. The procedure for constructing the registration phantoms is outlined in Fig. 2-2. The phantom was constructed from 2% agarose solution (2 g of agarose

powder mixed with 98 ml of pure water in a beaker). The clear agarose solution was heated in a microwave oven and then poured into the small-animal holder. After waiting 2 hours to allow any bubbles that may have formed to rise to the surface, the agarose phantom was molded into the appropriate shape for fixing the animal. To prepare the alignment markers, six glass beads with a diameter of 0.43–0.60 mm (Sigma-Aldrich, MO, USA) were placed inside six holes created in the phantom. The holes were created with a diameter of 1 mm. The length of the column was around 3 mm. The six markers were positioned around the tumor surface and were separated by at least 4–5 mm. In addition, 0.1 μl of [^{18}F]FDG was injected into each hole using a microinjector, and the tumor-bearing mouse was fixed in the holder with the registration phantom. After microPET imaging, the agarose liquid was used again to seal the six holes for microUS. Once the registration phantom within the small-animal holder was set up, the spatial relation between the images of these two modalities was fixed and hence its transformation matrix remained constant.



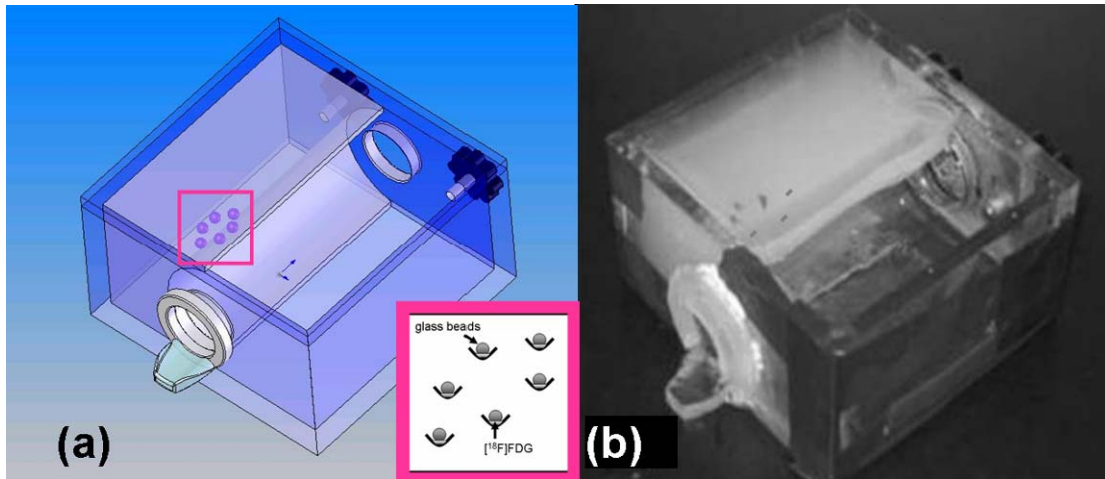


Fig. 2-1. Schematic (a) and photograph (b) of the registration phantom and the small-animal holder.

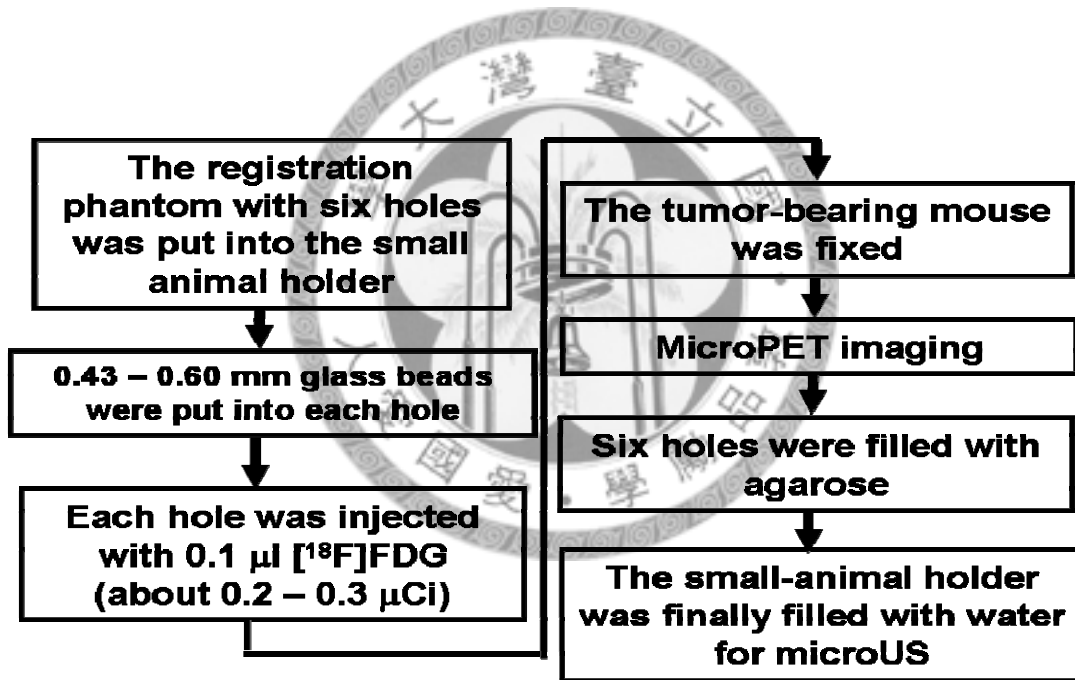


Fig. 2-2. Flow chart of the procedure for constructing the registration phantom.

2.3 Experimental Setup for MicroPET and MicroUS

The flow chart for image acquisition and processing is shown in Fig. 2-3. The tumor-bearing mouse was fixed in the animal holder 30 minutes after 200–300 μCi [^{18}F]FDG was injected into the lateral tail. For microPET scans, the tumor-bearing mouse was anesthetized with halothane vapor using a vaporizer system (Fluosorber, Market Supply, London, UK), with the scans being performed for 10 minutes. The small-animal PET imaging system was a microPET system (R4, Concord Microsystems, Knoxville, TN) with an axial extent of 7.8 cm, a field of view of 9.4 cm, and an animal port with a diameter of 12 cm. In the microPET system, the spatial resolution slowly decreased as the isotope was moved away from the center of the field of view. The spatial resolution of the x, y, z axes is around 1.6–1.8 mm FWHM in the center of the field of view. At 5 mm radial offset, these values decreased to 2.2–2.5 mm FWHM. The system consisted of 96 detector modules, each comprising an 8×8 array of $2.2 \times 2.2 \times 10 \text{ mm}^3$ lutetium oxyorthosilicate crystals, arranged as 32 crystal rings in a diameter of 14.8 cm. The peak sensitivity of this system is 2.1% at the center of the field of view with a 250–750 keV energy window [34].

After microPET imaging was performed, the six holes in the registration phantom were filled with agarose solution. Meanwhile, the C57BL/6J black mouse bearing WF-3 tumor cells was also fixed and laid down in the small animal holder. After the agarose solution had solidified, the holder was filled with warm water (38°C). MicroUS imaging was performed using a personal computer (PC)-based imaging subsystem (CLI 1500Ti, Capistrano Labs, San Clemente, CA). In our measurements, the sound velocity of 98 wt% agarose phantom is around 1519 m/s at 38 °C. The sound velocity of graphite-agarose phantom (graphite 0.2 wt%, agarose 98 wt%) is around 1532 m/s at 38 °C. The default ultrasound velocity is set at 1.519 or 1.532 mm

per microsecond from CLI's UltraView software. The transmit frequency was 20 MHz, the transducer had a diameter of 7 mm and a fixed focus at 12 mm, and the lateral scanning range was 35° in sector format. 3D volume data were acquired with an elevational spacing between frames of 0.15 mm.

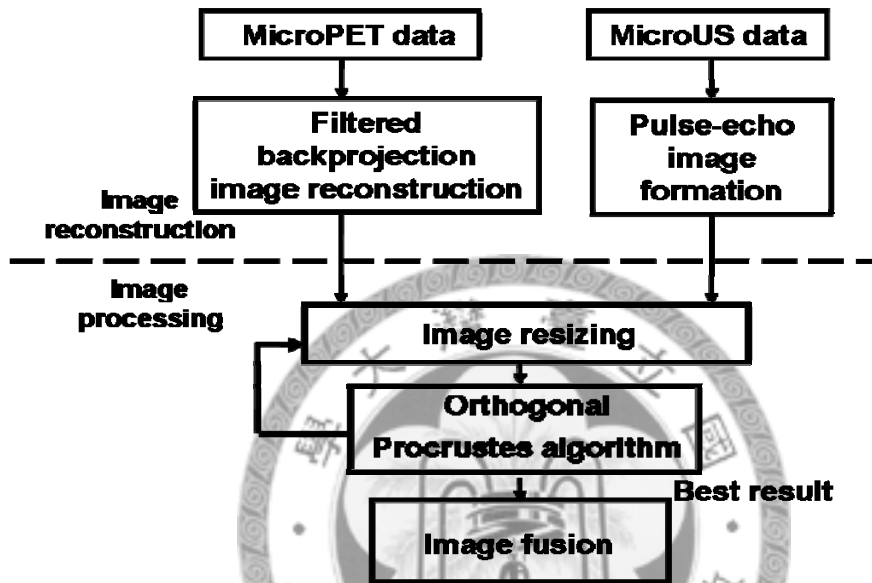


Fig. 2-3. Flow chart of microUS/microPET image acquisition and processing.

2.4 MicroUS/microPET Data Processing and 3D Reconstruction

As outlined in Fig. 2-3, the microPET system was operated in full 3D mode, permitting coincidence between any two detector rings. The list-mode data were sorted into full 3D sinograms, and all image data were reconstructed using a filtered backprojection method with a 256×256×63-voxel matrix [35]. The voxel size was 0.42×0.42×1.2 mm³.

For microUS imaging, the received echoes were sampled and stored on a PC. The envelope signal was detected, and the B-mode image was displayed using MATLAB

(MathWorks, MA, USA). The 3D image data were obtained with a $2089 \times 1401 \times 160$ -voxel matrix, with a voxel size of $0.0187 \times 0.01875 \times 0.15 \text{ mm}^3$. Both microUS and microPET images were then adjusted to the same voxel size of $0.075 \times 0.075 \times 0.075 \text{ mm}^3$ before image registration (Fig. 2-4).

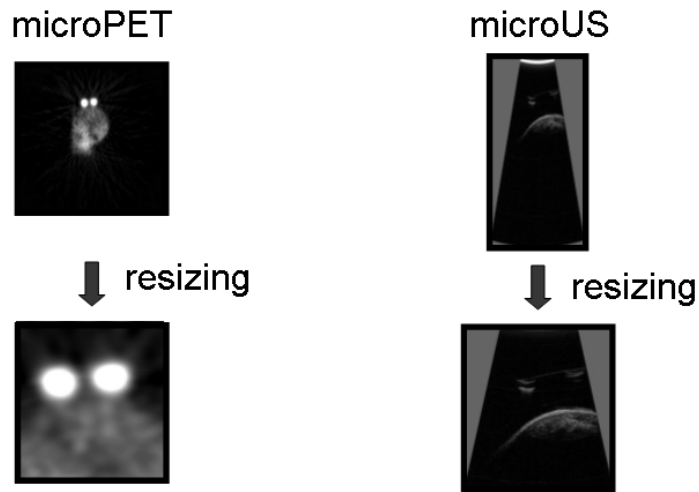


Fig. 2-4. Making the voxel size the same in the two imaging systems.

The boundaries of six markers were contoured and the center of gravity of each marker was calculated, and then the center of gravity of the six markers was used to perform the rigid-body registration transformation. The microUS/microPET images containing markers and tumors were fused and visualized using Amira software (version 3.1.1, Template Graphics Software, CA, USA). 3D image reconstruction was performed using Amira software, which required manual contour detection on each 2D image. A typical example is shown in Fig. 2-5. Fig. 2-5(a) shows a cross-sectional image and three projections on the x - y , y - z , and x - z planes, and Fig. 2-5(b) shows the corresponding results for contour detection.

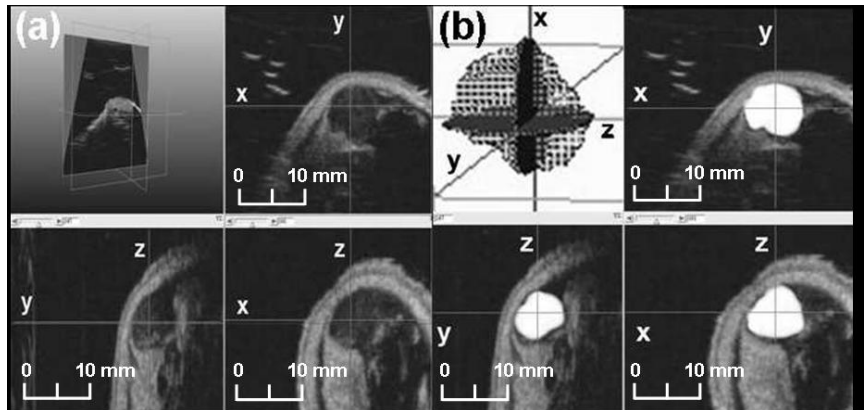


Fig. 2-5. 3D image reconstruction using Amira software: (a) selection of central slices for the three orientations, and (b) detection of the contours of the tumor boundary (white).

Fig. 2-6 shows typical transverse (top), sagittal (middle), and coronal (bottom) views of a second-week tumor with registration markers. The left, middle, and right panels in Fig. 2-6 show the microUS, microPET, and microUS/microPET fused images, respectively. Fig. 2-7(a), (b) and (c) show the results for contour detection for microUS, microPET, and both registration and image fusion, respectively, and Fig. 2-7(d) shows the three projections onto x - y , y - z , and x - z planes.

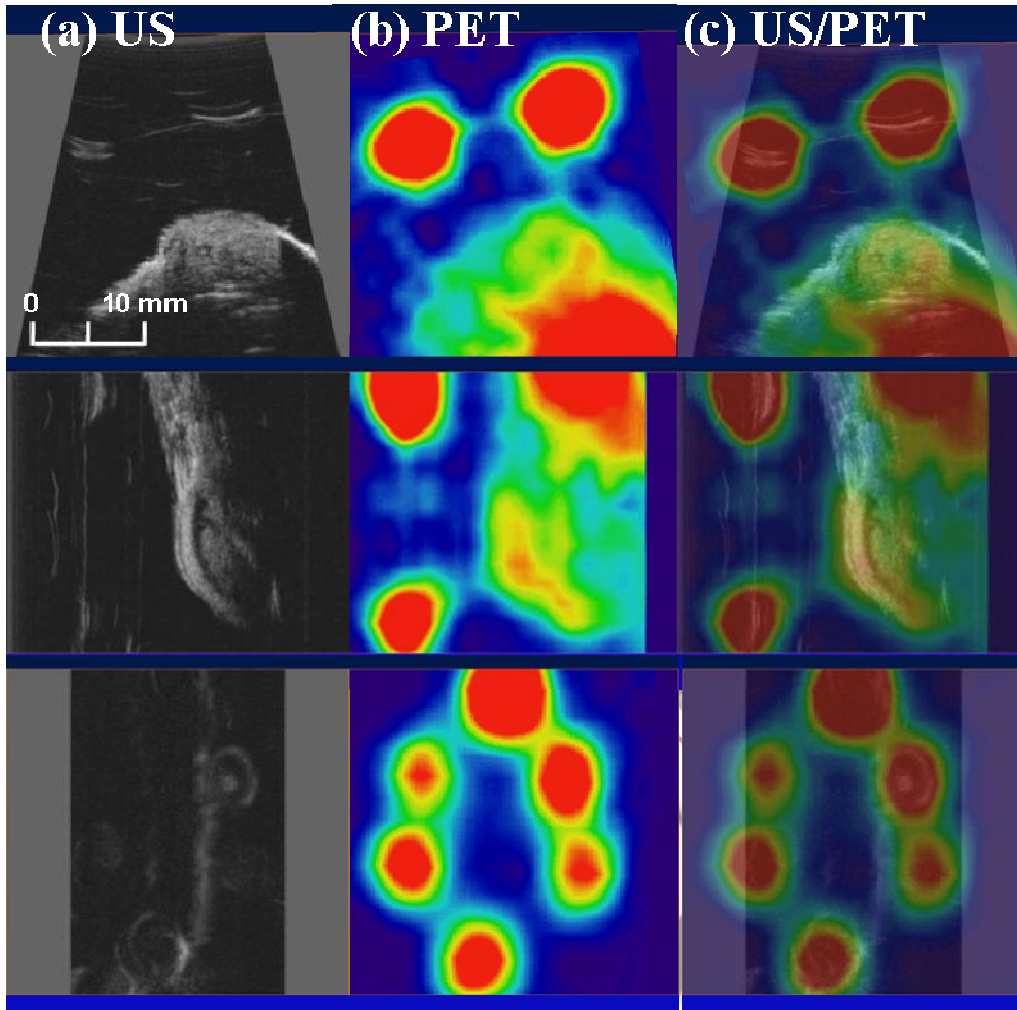


Fig. 2-6. MicroUS (a) and microPET (b) transverse (top), sagittal (middle), and coronal (bottom) images of the tumor region with the registration markers. (c) The microUS/microPET fused images.

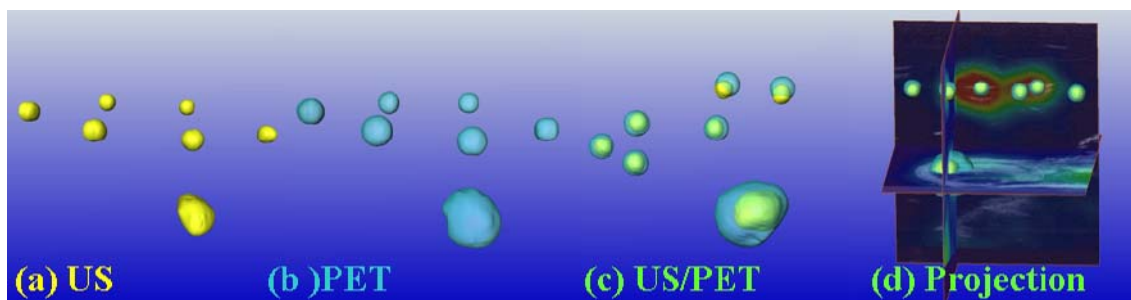


Fig. 2-7. 3D reconstruction of the tumor (bottom) and the six registration markers (top) for (a) microUS, (b) microPET, and (c) microUS (white blobs)/microPET (dark blobs) fused images after registration. The three projection images are shown in (d).

2.5 Test Phantom Design and Estimation

In principle, TRE is a direct measure of the registration performance. However, due to microUS and microPET images containing distinctly different information, in practice it is difficult to compute TRE. We therefore used FRE to quantify the performance of our technique. In addition, a test phantom was built with a known object for TRE calculations. The test phantom, including the target point and the six markers, is shown in Fig. 2-8. The test phantom consisted of a graphite-agarose region and an agarose region. The purpose of the graphite-agarose region was to hold a glass capillary for microUS imaging. The target point in the test phantom was fixed by positioning the end point of the glass capillary at the boundary between the two regions. Also, three markers were placed in each of the graphite-agarose and agarose regions. Three such test phantoms were constructed to allow three sets of independent experiments to be performed.

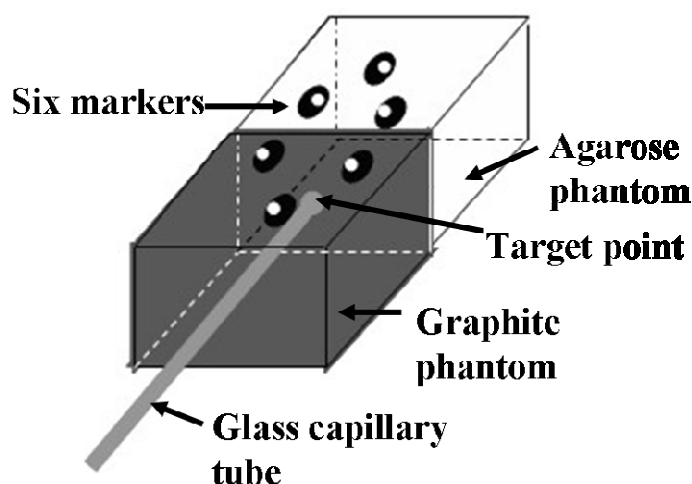


Fig. 2-8. Design of the test phantom containing six markers. The phantom consisted of a graphite-agarose region and an agarose region. The glass capillary tube was held within the graphite-agarose region. Each region contained three markers.

2.6 Rigid-Body Transformation and Error Estimation

A rigid-body transformation algorithm was used for the image registration between microUS and microPET using only rotations and translations (i.e., no deformations). In other words, a point $p_i = (x_i, y_i, z_i)$ in the test image was transformed into a point $q_i = (x_r, y_r, z_r)$ in the reference image using

$$q_i = T(p_i) = Rp_i + t, \quad (\text{Eq. 2-1})$$

$$= \begin{bmatrix} 1 & 0 & 0 \\ 0 & \cos(\sigma) & \sin(\sigma) \\ 0 & -\sin(\sigma) & \cos(\sigma) \end{bmatrix} \begin{bmatrix} \cos(\varphi) & 0 & \sin(\varphi) \\ 0 & 1 & 0 \\ -\sin(\varphi) & 0 & \cos(\varphi) \end{bmatrix} \begin{bmatrix} \cos(\theta) & \sin(\theta) & 0 \\ -\sin(\theta) & \cos(\theta) & 0 \\ 0 & 0 & 1 \end{bmatrix} p + \begin{bmatrix} t_x \\ t_y \\ t_z \end{bmatrix}, \quad (\text{Eq. 2-2})$$

where $i = 1-6$ (since there were six markers), $t = (t_x, t_y, t_z)^T$ is the translation vector, and R is the rotation matrix for angles σ , φ , and θ about the x , y , and z axes, respectively. The geometry is also shown in Fig. 2-9, where $t_x, t_y, t_z, \sigma, \varphi$, and θ are the six unknowns to be solved by the following least-squares method:

$$\min_{R, t} \sum_{i=1}^N \|q_i - (Rp_i + t)\|^2, \quad (\text{Eq. 2-3})$$

R and t in (Eq. 2-3) were solved using the orthogonal Procrustes algorithm [36]-[37] with the following steps. First, the new coordinates q' and p' are obtained by subtracting the coordinates of the center of gravity from the markers:

$$q_i' = q_i - \bar{q}, \quad (\text{Eq. 2-4})$$

$$p_i' = p_i - \bar{p}, \quad (\text{Eq. 2-5})$$

where \bar{p} and \bar{q} are the coordinates of the center of gravity calculated from all markers. Second, the correlation matrix H is obtained by calculating the correlation coefficients of q' and p' :

$$H = \sum_{i=1}^N p_i' q_i'^T, \quad (\text{Eq. 2-6})$$

Third, singular value decomposition is performed on H:

$$H = UDV^T, \quad (\text{Eq. 2-7})$$

where U and V are orthogonal matrices and D is the diagonal matrix with singular values. Fourth, the rotation matrix is obtained using

$$R = VU^T, \quad (\text{Eq. 2-8})$$

and finally the translation matrix is obtained as

$$t = \bar{q} - R\bar{p}. \quad (\text{Eq. 2-9})$$

The purpose of the above registration method was to minimize the FRE, defined as the root-mean-square distance between corresponding fiducial points (i.e., markers), before and after registration. The other important error measure was the TRE, which is the distance between target points before and after registration [38].

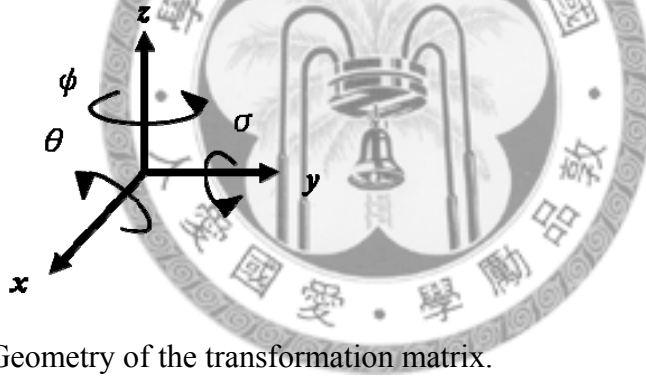


Fig. 2-9. Geometry of the transformation matrix.

The calculated values of FRE and TRE are listed in Tables 2-1 and 2-2. Table 2-1 lists the FRE values of a tumor-bearing mouse from all six registration markers after registration, and their mean value. The FRE ranged from 0.12 to 0.58 mm, with a mean of 0.31 mm. These results demonstrate the efficacy of the proposed method, given the size of the image markers and the resolution of the imaging systems. Table II summarizes the FRE and TRE results by listing the mean values for the three testing phantoms. The mean FRE and TRE of the three phantoms are 0.68 and 1.05 mm, respectively. TRE is generally larger than FRE, which is due to the registration being performed based on the markers rather than the target. Finally, Fig. 2-10 plots

FRE and TRE as functions of the number of markers used in registration. As expected, FRE increases with the number of markers; however, TRE decreases as the number of markers increases.

Table 2-1. FRE values after image registration.

	Marker 1	Marker 2	Marker 3	Marker 4	Marker 5	Marker 6	Mean±SD
FRE (mm)	0.21	0.34	0.58	0.36	0.27	0.12	0.31±0.11

Table 2-2. FRE and TRE values for the test phantoms (means from all six markers).

	FRE (mm)	TRE (mm)
Phantom 1	0.49	0.75
Phantom 2	0.80	0.94
Phantom 3	0.76	1.46
Overall mean	0.68	1.05

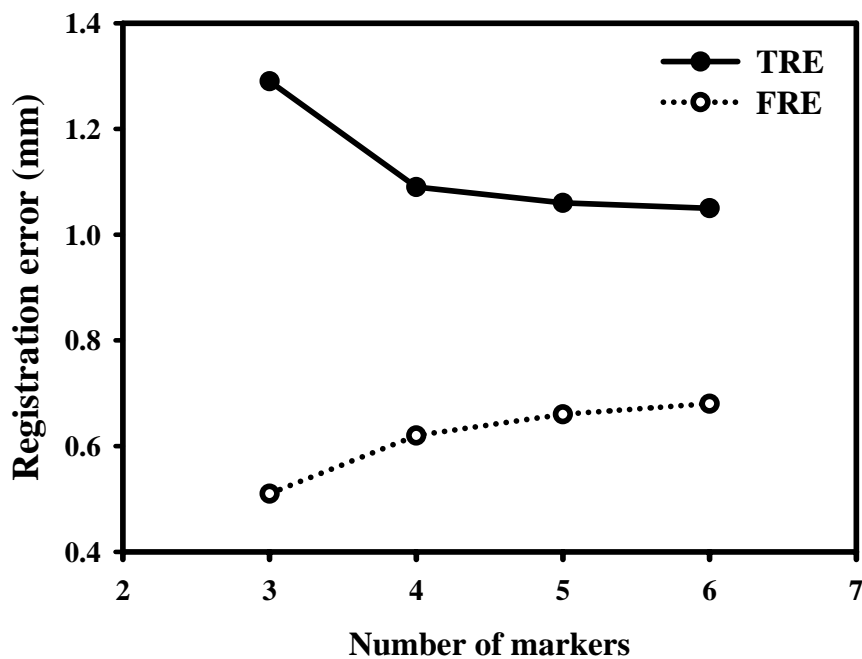


Fig. 2-10. FRE and TRE values as functions of the number of markers used in registration.

2.7 Discussions

Several factors influence the performance of our proposed method. First, the [^{18}F]FDG may have diffused into the surrounding agarose, which would affect the results of contour detection in microPET imaging. Second, in microUS, because the transducer had a fixed geometric focus and this was where the tumor was placed, the markers were out of focus and hence exhibited a degraded point spread function. Image deconvolution could be applied to improve the point spread function and the registration performance [39]. Similarly, ordered-subset expectation maximization could be used instead of the filter backprojection technique for microPET imaging. However, although alternative image reconstruction methods may improve the imaging of the markers, the additional benefits are limited by only the center of gravity being used to define the marker positions.

Third, the registration error (0.31 mm) is less than the image resolution of microPET system (1.6–2.5 mm) and more than the image resolution of microUS (0.15 mm). It seems that the resolution limits the usefulness of the registration system. However, the fused image can help us to observe the accurate position of the tumor. It can improve the limits of the image resolution of microPET. Fourth, observed error is an important factor which would magnify the experimental errors. To mechanize the constructed process of the registration system is a way to reduce the observed errors. On the other hand, the accurate of the measuring instrument is important as mechanization.

Fifth, the markers should ideally be distributed around the tumor, whereas in practice they can be placed only on one side of the tumor and between the transducer surface and the tumor, which resulted in lower TRE values in our simulations. Finally, the minimum distance between any two markers needs to be set whilst considering the

finite marker size and the resolution of the imaging systems. Moreover, interference will occur if the markers are placed too close to a tumor. These factors together limit the number of markers that can be placed in the registration phantom. In our method there are six unknowns to solve, and hence there should be at least six markers to ensure that the problem is not underdetermined. The use of smaller markers would allow more markers to be included, and if the signal intensity remains sufficient this should improve the performance (see Fig. 2-10).

We have developed an effective method for the 3D registration of combined microUS and microPET imaging. The distinct differences between the natures of these two imaging methods makes it necessary to utilize external markers. In addition, rigid-body transformation is employed to ensure adequate performance. FRE can be used to quantify the effectiveness of the method, and we constructed test phantoms with a known image target so that TRE values could also be determined. Such methods could also be applied for the registration of other small-animal imaging modalities.

The primary application of the proposed method is in cancer research on small-animal models. In such applications microUS provides excellent anatomical information, whereas microPET provides information on glucose metabolism. Future studies could add ultrasonic color Doppler imaging to evaluate angiogenesis. Since cancer drugs are delivered to the tumors via the vessels, such a multimodality approach represents an effective tool for both drug development and cancer research.

CH 3. NONINVASIVE TUMOR IMAGING WITH HIGH FREQUENCY ULTRASOUND AND MICROPET IN SMALL ANIMALS

Small-animal models have been widely used in the biomedical sciences to study human diseases and evaluate treatment effectiveness. Conducting small-animal experiments more efficiently has also become a key factor to the success and timeliness of the related studies. For example, the periodic caliper measurement is frequently used for the evaluation of treatment efficacy for superficial tumors. However, overestimation of tumor size was a disadvantage of manual caliper measurements [40]. Recently, multimodalities of molecular imaging for non-invasive tumor volume analysis have been of research interest [41]-[43]. Such methods can be used to assess tumor growth and treatment effectiveness.

High frequency ultrasound refers to the frequency range higher than 20 MHz.[9]-[11] High frequency ultrasonic micro-imaging (microUS) is an important tool for obtaining non-invasive real-time images of small animals. A spatial resolution of less than 100 μm can be achieved when high-frequency ultrasound is used. The center frequency used in this study was 40 MHz and the corresponding spatial resolution is around 75 μm at the focus [12]. Three dimensional (3D) microUS imaging and segmentation were reported and shown to be a reliable tool in the early detection and longitudinal growth analysis of xenograft tumor in mice [40]. A biomicroscopy system (VS40, Visualsonics Inc., Toronto, Ontario, CA) was used. Ellipsoidal formulas are typically used for the volume estimation. The application of 3D microUS to prostate cancer in mice showed advantages, such as high spatial

resolution and contrast in soft tissue. 3D microUS also may be particularly well suited for the quantitative assessment of metastatic progression and the evaluation of chemotherapeutics in preclinical liver metastasis models [44]-[46].

Optical imaging, such as fluorescent or bioluminescent imaging, is another alternative for monitoring tumor growth and progression [43], [47] In vivo confocal microscopy and bioluminescent imaging systems are able to monitor the molecular processes associated with carcinogenesis. They have also been used to study the role of specific genes in cancer progression and viral vector targeting of metastasis. In spite of these advantages, these methods are difficult to be applied in clinics and thus are limited to preclinical research.

Positron-emission tomography (PET) provides 3D distribution of positron-emitting radiopharmaceuticals. Using radiolabeled biomolecules and kinetics models, PET can be used for quantitative measurements of many metabolic functions in living animals, such as brain, heart and tumors. For small animal studies, microPET [13]-[14] was designed with improved spatial resolution over clinical PET. The spatial resolution of microPET used in this study (R4, Concord Microsystems, Knoxville, TN, USA) is about 1.8 mm at the center of the field of view and dropped to 2.5 mm (radial component) at 25 mm off-center. Such resolution is inferior to that of microUS. Although microPET is unable to obtain anatomical information of small animals, it is an ideal tool for assessing tumor metabolism. The purpose of this study is to explore the potential of combining microUS and microPET for small animal tumor imaging. The microUS system was developed in-house. MicroUS and [¹⁸F]FDG microPET imaging were performed on C57BL/6J black mice bearing WF-3 ovarian carcinoma. For each mouse, tumor growth was monitored in vivo by traditional caliper measurement, microUS and [¹⁸F]FDG microPET. 3 D tumor segmentation and volume estimation were applied on tumors from 2 to 8 weeks. The intercomparison

between the three modalities was performed.

3.1 Small-Animal Model

All animal experiments were performed under an approved animal care protocol of the National Animal Center of R.O.C. MicroUS (n=5) and microPET (n=3) female C57BL/6 mice weighting 18–22 g were used in this study. Detailed methods to construct the small animal model have been described previously (Section 2.1). The tumor cells were injected subcutaneously into the right shoulder of the mouse. After 2 weeks, microUS and [¹⁸F]FDG microPET imaging were performed on a weekly basis. Vernier caliper measurements were also made before microUS, in which we measured the lengths of the three dimensions of the tumor and the tumor volume was calculated according to the ellipsoid model [40]:

$$V = \frac{\pi}{6} w^2 l, \quad (\text{Eq. 3-1})$$

where V is the tumor volume, w is the short axis, and l is the long axis along the three spatial coordinates.

3.2 Small-Animal High-Frequency Ultrasound Imaging

MicroUS was performed 2 weeks after tumor implantation. C57BL/6J black mice bearing WF-3 mouse ovarian carcinoma cells were anesthetized and laid down in warm water (38°C). The 8-bit, 200-Msamples/s arbitrary-function generator (DAC200, Signatec, CA, USA) was used to generate the desired transmit waveform, which then was sent to a power amplifier (25A250A, Amplifier Research, PA, USA) to drive the lithium-niobate focused transducer. The scan-line data acquired at each position were

sent to an ultrasonic receiver (5900 PR, Panametrics, MA, USA). Finally, the signal was sampled with a 500-MHz digitizer (PDA500, Signatec). The center frequency of the single-crystal lithium niobate transducer (NIH Resource Center for Medical Ultrasonic Transducer Technology, PA, USA) was 45 MHz. The -6dB beam width at the focus at this frequency is $75\ \mu\text{m}$ [9], [12]. The focus was placed in the centre of the tumour. All experiments employed the transmission of three cycles of a 40-MHz sinusoid. The transducer had a fixed focus at 12 mm. The lateral scanning range of 2 cm was controlled by a 4-axis mechanical scanning system (CSI, Taipei, Taiwan). The spacing between scan lines was $40\ \mu\text{m}$, and the pulse repetition interval was 1 ms. The elevational spacing between frames was $200\ \mu\text{m}$, and the tumor volume was measured after 3D image reconstruction.

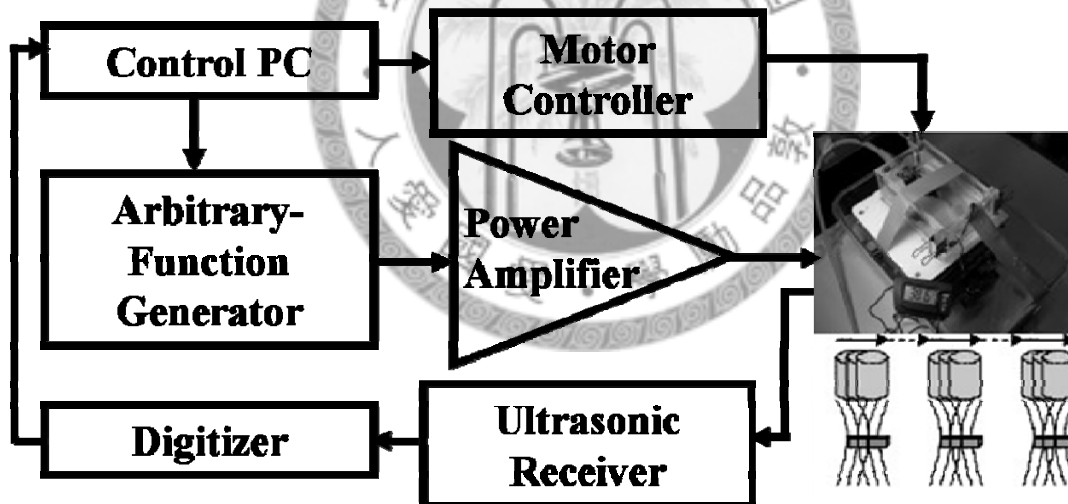


Fig. 3-1. MicroUS system block diagram.

3.3 Small-Animal MicroPET Imaging

After microUS was performed, the mice were sent to the National PET and Cyclotron Center in Taipei Veterans General Hospital for microPET scanning. The microPET Primate four-ring system (R4, Concord Microsystems, Knoxville, TN, USA) is an animal PET device with a 7.8-cm axial extent, a 9.4-cm field of view, and a 12-cm-diameter animal port. The system consisted of 96 detector modules, each comprising an 8×8 array of 2.2×2.2×10 mm³ lutetium oxyorthosilicate crystals, arranged as 32 crystal rings in a 14.8-cm diameter. The peak system sensitivity is 2.1% at the center of the field of view with a 250–750 keV energy window [34]. For microPET scans, each tumor-bearing mouse was anesthetized with halothane vapor using a vaporizer system (Fluosorber, Market Supply, UK) and laid on a table. About 200–300 μCi of [¹⁸F]FDG was injected through the lateral tail vein, and then microPET scans were performed continuously for 2 hours. All images were reconstructed using a filtered back-projection method¹⁷ with a 256×256 matrix. Data acquisition by microPET scanning was initiated at the first minute after drug injection. Dynamic microPET imaging data were acquired using one 15-min frames, three 10-min frames and nine 5-min frames, followed by 10-min frames up to 2 h after injection. Finally, time-activity curves (TACs) were derived from the mean values in the region of interest in the tumor and the contralateral normal tissue by ASIpro VMTM (Concorde Microsystems).

3.4 MicroUS/microPET Data Acquisition, 3D Tumor Reconstruction, and Volume Measurement

The microUS/microPET image acquisition/processing technique is outlined in Fig. 3-2. It was less than one day between microUS scanning and microPET scanning. The microPET system was operated in full 3D mode, permitting coincidences between any two detector rings. The list-mode data can be sorted into full 3D sinograms, or rebinned with single-slice rebinning or Fourier rebinning algorithms [35]. A rebinned data set mimics the data from a conventional 2D system, resulting in a total of 63 sinogram planes with an axial sampling distance of 1.2 mm that can be reconstructed by standard 2D filtered back-projection.

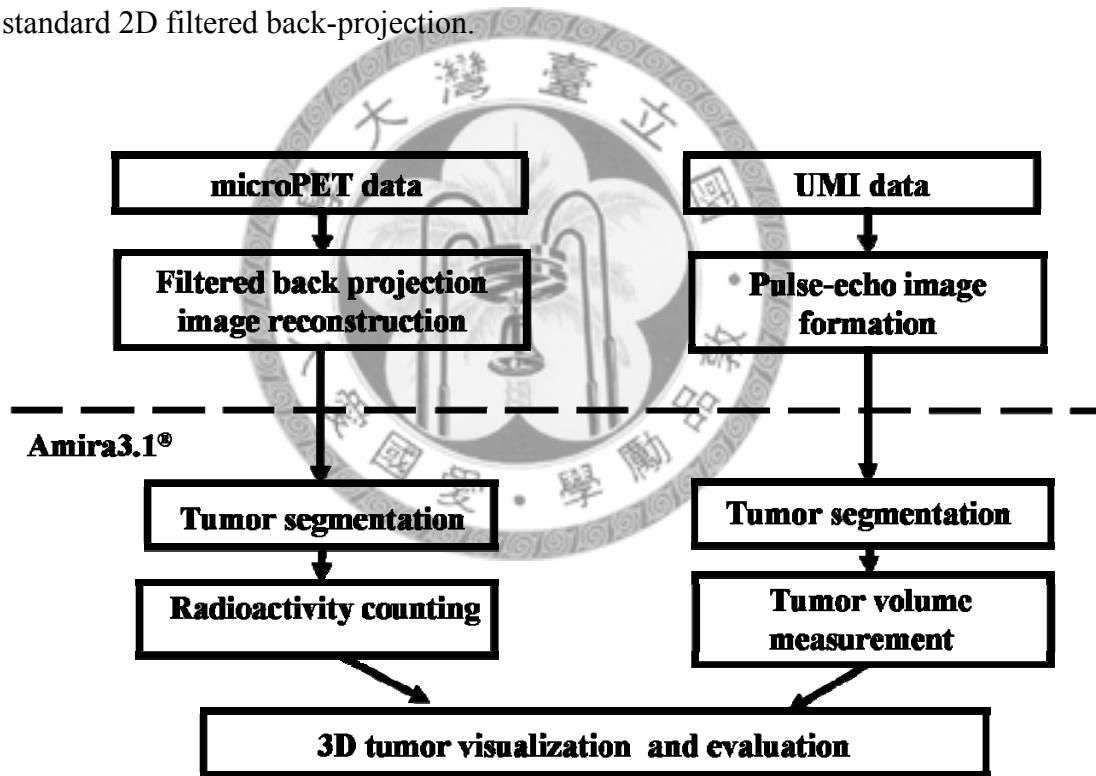


Fig. 3-2. MicroUS/microPET image acquisition and processing.

Pulse-echo image formation was used for microUS, with the same transducer used for both transmission and detection. The received echo signals were sampled and stored in a personal computer. The envelope signal was detected, and the B-mode

image was displayed using MATLAB (MathWorks, MA, USA).

The tumors in microUS 3D small-animal images were segmented and 3D volume data were reconstructed. The volume of the tumor was measured by Amira3.1 software (Template Graphics Software, CA, USA), which required manual contour detection on each 2D image. The central slices for three orientations were selected, and the tumor boundary was contoured by a radiologist. A typical example is shown in Fig. 3-3. Fig. 3-3(a) shows a microPET cross-sectional image and three projections on the x - y , y - z , and x - z planes, and Fig. 3-3(b) shows the corresponding results for contour detection (red). Fig. 3-3(c) shows the selection of central slices for the three orientations in microUS, and Fig. 3-3(d) shows the detection of the contours of the tumor boundary (red).

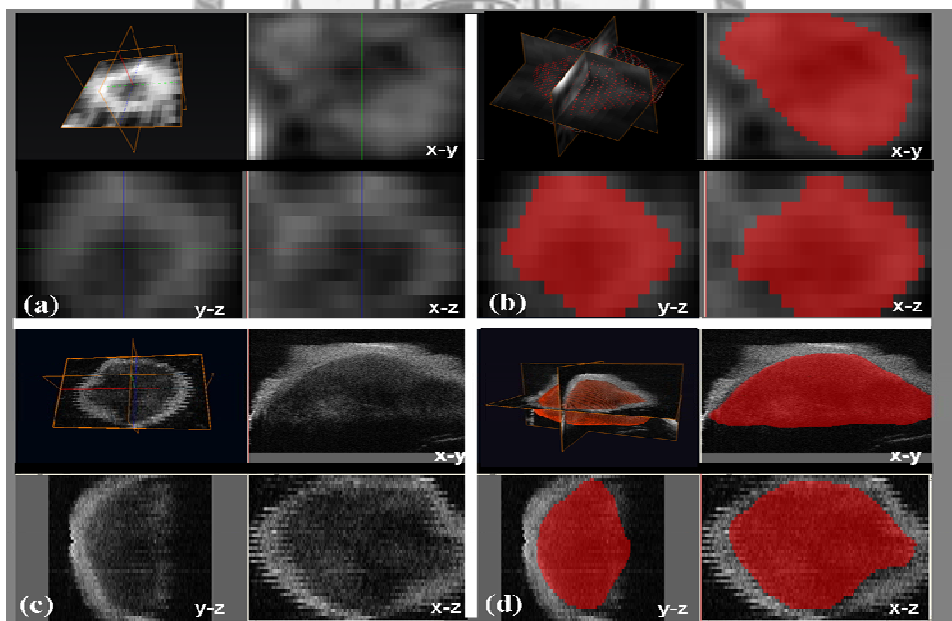
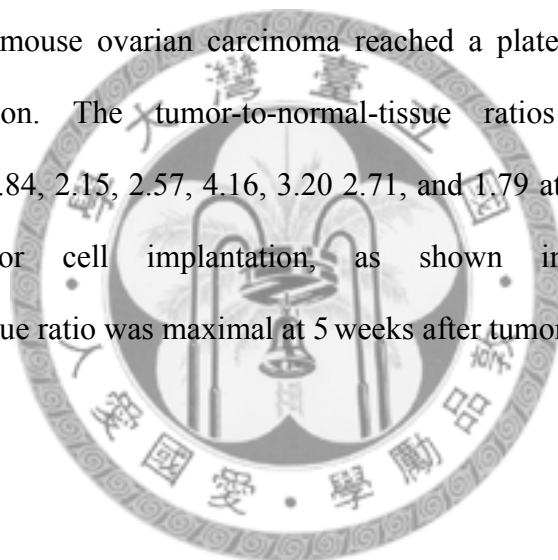


Fig. 3-3. 3D image reconstruction using Amira software: (a) selection of central slices for the three orientations in microPET, and (b) detection of the contours of the tumor boundary (red). (c) selection of central slices for the three orientations in microUS, and (d) detection of the contours of the tumor boundary (red).

Fig. 3-4(a) shows the parenchyma of an 8th-week tumor. Fig. 3-4(b) shows a B-mode high-frequency ultrasound image, tumor segmentation, and the 3D volume reconstruction of a tumor. This image was also obtained at the 8th week after tumor cells implantation. Since this method is noninvasive, the tumor volume was measured every week after tumor implantation. Fig. 3-4(c) shows a microPET image, tumor segmentation, and the corresponding 3D reconstruction. To allow comparisons, the image was again obtained at the 8th week after tumor cells implantation. With microPET, the TACs of [^{18}F]FDG in the tumor and the normal tissue were also obtained for 2 hours after the injection of [^{18}F]FDG (Fig. 3-5). The uptake of [^{18}F]FDG in WF-3 mouse ovarian carcinoma reached a plateau before or at 4000 seconds postinjection. The tumor-to-normal-tissue ratios at 4000 seconds postinjection were 1.84, 2.15, 2.57, 4.16, 3.20, 2.71, and 1.79 at 2, 3, 4, 5, 6, 7 and 8 weeks after tumor cell implantation, as shown in Table 3-1; the tumor-to-normal-tissue ratio was maximal at 5 weeks after tumor implantation.



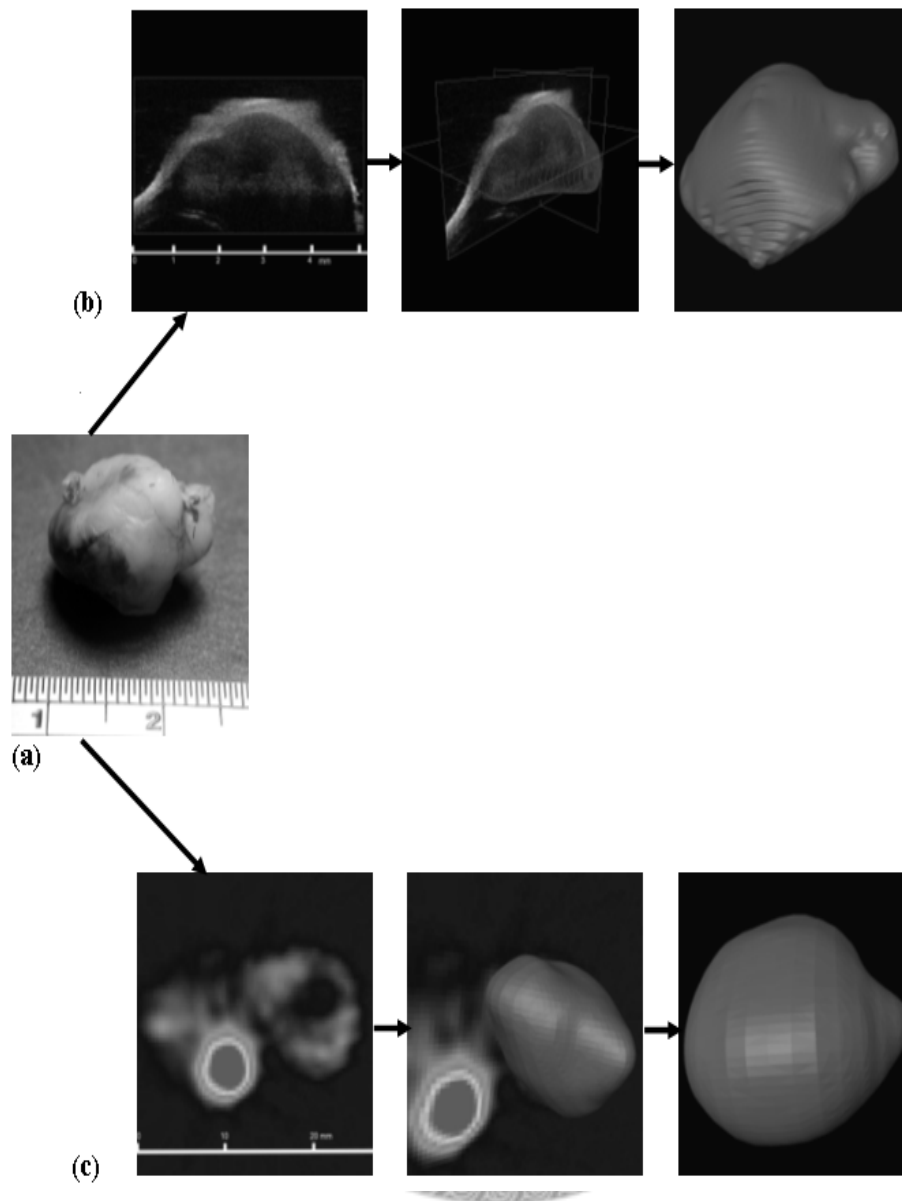


Fig. 3-4. (a) Parenchyma of a tumor at the 8th week after tumor implantation. (b) B-mode microUS image (left, partial transverse section), tumor segmentation (middle), and the corresponding 3D representation (right) at the 8th week. (c) MicroPET image (left, whole-body transverse section), tumor segmentation (middle), and the corresponding 3D representation (right) of the 8th-week tumor.

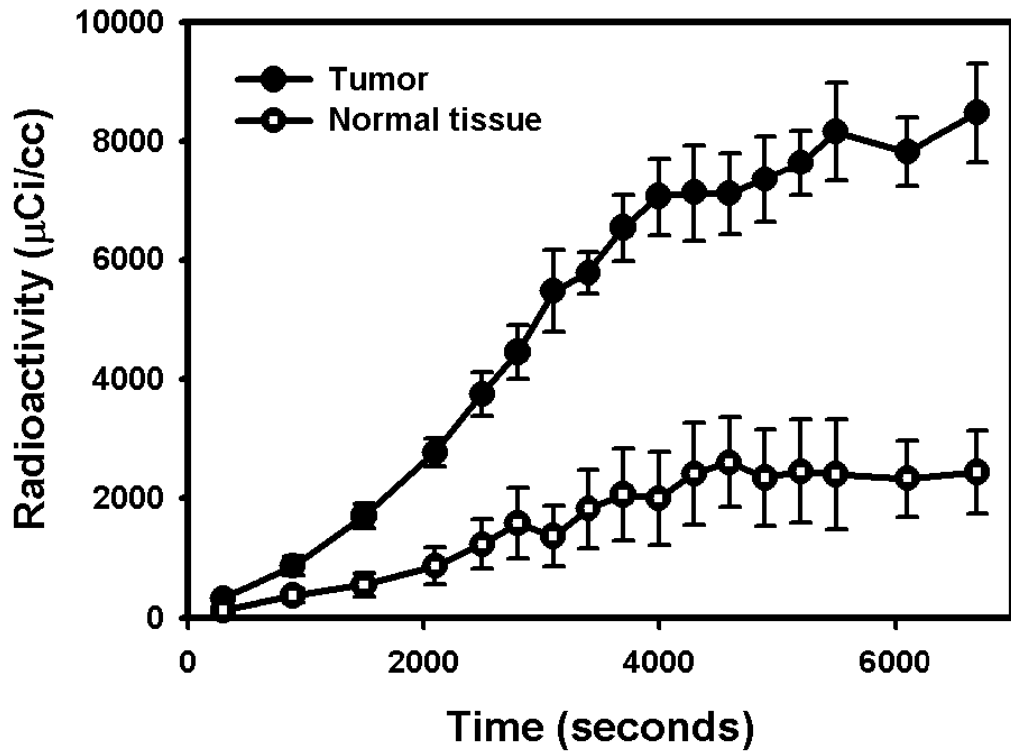


Fig. 3-5. Time-activity curves obtained by microPET of [¹⁸F]FDG for C57BL/6J mice bearing WF-3 mouse ovarian carcinoma.

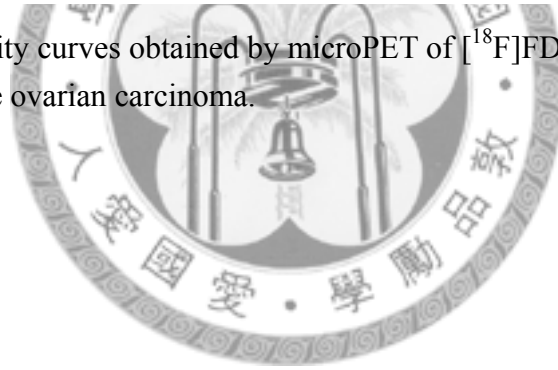


Table 3-1. Tumor volumes and radioactivity measurements.

Time (weeks)	Caliper		MicroUS imaging			MicroPET imaging			
	<i>n</i>	Tumor volume (mm ³)	<i>n</i>	Tumor volume (mm ³)	MicroUS to caliper ratio (%)	<i>n</i>	3D reconstruction of radioactive region (mm ³)	microPET to caliper ratio (%)	Tumor-to-normal-tissue ratio
2	5	28.74±6.99	5	16.79±4.75	58.42	3	33.96±7.65	118.16	1.84±0.27
3	5	45.66±13.16	5	31.09±12.94	68.09	3	46.78±5.93	102.45	2.15±0.36
4	5	65.92±19.33	5	50.21±19.52	76.17	3	90.68±17	137.56	2.57±0.40
5	5	326.80±58.22	5	225.55±21.62	69.02	3	245.12±47.03	75.01	4.16±0.63
6	5	476.18±22.99	5	264.98±28.44	55.64	3	400.44±100.66	84.09	3.20±0.39
7	5	554.89±54.36	5	428.06±22.36	77.14	3	427.99±90.4	77.13	2.71±0.44
8	5	724.38±44.63	5	530.95±13.53	73.30	3	478.29±88.6	66.03	1.79±0.58



3.5 In Vivo Growth Curve

The growth curve of the WF-3 mouse ovarian carcinoma was obtained by microUS and compared with the microPET radioactivity data. The lag time, population doubling time, and plateau level were determined from the growth curve [48]-[49].

The doubling time (T) of WF-3 ovarian carcinoma cells in vivo was calculated as [48]

$$T = \frac{(t-t_0) \times \log 2}{\log N - \log N_0}, \quad (\text{Eq. 3-2})$$

where t is a time point during the exponential phase, N is the tumor volume at time t , and N_0 is the tumor volume at another time point t_0 .

The typical growth curve shown in Fig. 3-6 (data in Table 3-1) exhibits a lag period (2–4 weeks) and an exponential phase (4–8 weeks). This was possibly followed by a plateau phase, resulting in a sigmoid-shaped curve (data not shown). In Fig. 3-6, the in vivo tumor growth curves by microUS and vernier caliper are shown. Means and standard deviations are also shown in this figure. The average tumor volume doubling time as determined during the exponential phase was 7.5 days by microUS. The result was compared with 7.8 days calculated by caliper measurement. In Fig. 3-7, 3D tumor volume reconstruction by microPET imaging based on the radioactivity at various stages is shown. The caliper measurement, microUS and microPET imaging data are compared in Fig. 3-6, Fig. 3-7 and Table 3-1. In Fig. 3-6 and Fig. 3-7, the slopes of the curves are parallel before 6 weeks after tumor cell injection. During 6 to 8 weeks, the slope of the curve in Fig. 3-7 decreases, and the standard deviations increase at this period. In Table 3-1, the tumor volumes obtained from vernier caliper measurements were used as the denominator for tumor volume comparisons. The ratios of tumor volumes obtained from microUS and caliper varied from 58 %-76 %, but were 102 %-138 % for microPET, from week 2-4. From the results, the tumor

volume obtained from microPET was larger than caliper measurements at early stages. At late stages (5-8 weeks), standard deviations of microUS and caliper tumor volume measurements were from 14-58 mm³, but were 47-101 mm³ for microPET. In our study, tumor-bearing mice begin to die after 7 weeks.

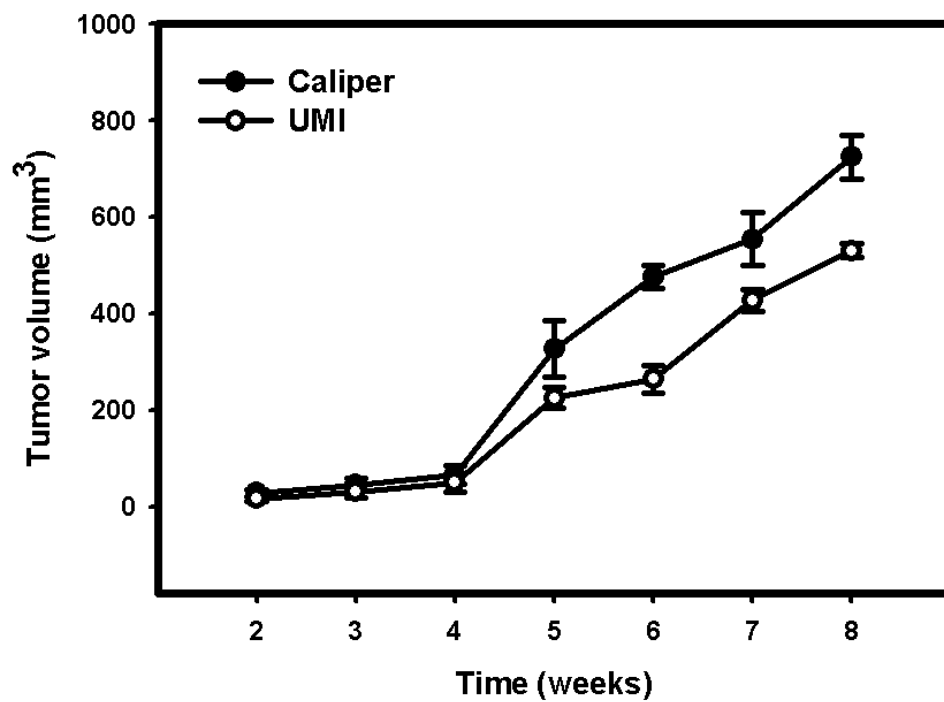


Fig. 3-6. In vivo tumor growth curve by microUS and vernier caliper. Means and standard deviations are shown.

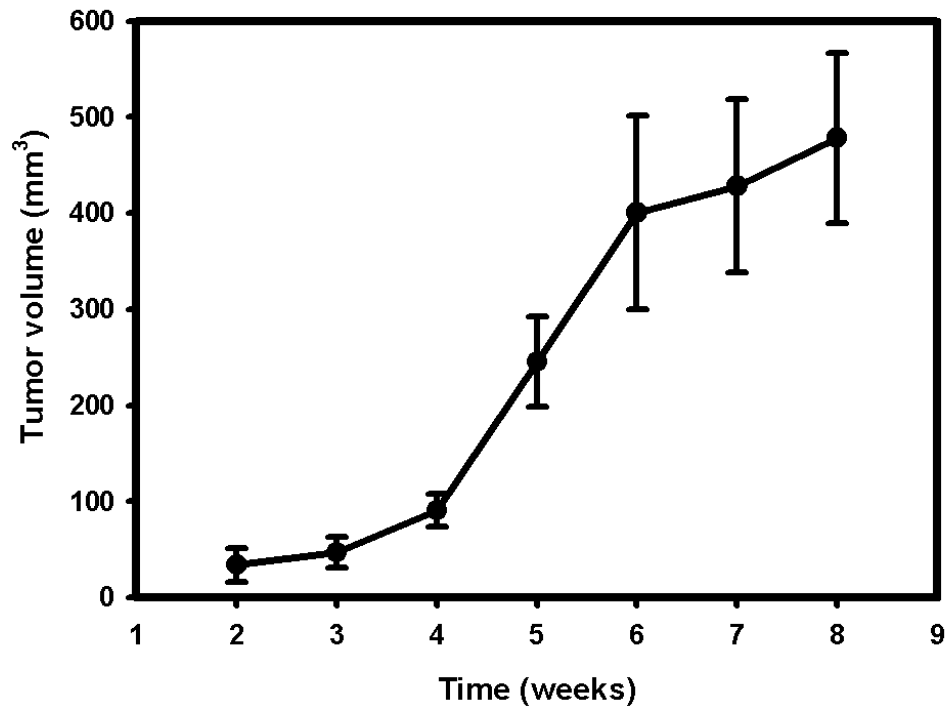


Fig. 3-7. 3D tumor volume reconstruction by microPET imaging based on the radioactivity.

3.6 Discussions

The vernier caliper technique is noninvasive and commonly adopted for tumor volume measurements in the literature. Although “overestimation” is a disadvantage of this technique, the measurement errors are generally consistent. An actual measurement of tumor volume after excision is invasive and thus cannot be used in the longitudinal study as reported in our manuscript. Furthermore, actual measurements of tumor volume after excision may also be inaccurate when the tumor is not removed completely. Recently, some researchers have done through comparisons of 3D microUS and 3D histology [44]-[46] The histological correlations with microUS and microPET may improve the measurement errors.

The evaluation for cancer treatment efficacy using tumor volume measurements is

often impeded by the irregular shape of tumors and necrosis, such as the caliper measurement; or due to the invasive nature of the analysis, such as tumor incision. MicroUS and microPET are two non-invasive imaging techniques developed recently for long-term observation and quantitation of tumor treatment efficacy based on tumor volume or metabolism in small animal studies. We combined each modality with the caliper measurement, respectively, in order to compare these two imaging methods [41]. In table 1, the ratios of tumor volumes obtained from microUS and caliper were varied from 58 %-76 %, but were 102 %-138 % for microPET, from week 2-4. Manual caliper measurements were affected by skin layers and surrounding nontumoral tissue, leading to an overestimation of tumor size. Nonetheless, the tumor volumes obtained from microPET imaging were even larger due to its insufficient spatial resolution. The over-estimation was primarily due to inadequate spatial resolution. In other words, the large extent of the point spread function of the imaging system caused the over-estimation. These results suggest that microUS is more reliable than microPET in tumor volume measurements at early stages. Moreover, at late stages (5-8 weeks), standard deviations of microPET tumor volume measurements were large. The tumor boundary in microPET imaging is generally not clear after 5 weeks, possibly due to the hypoxia and/or necrosis when the tumor grows bigger. The hypoxic or necrotic tumor areas do not uptake radiopharmaceuticals, thus making it difficult to define the contour in microPET imaging [50]. The tumor-to-normal-tissue ratio from microPET was maximal at 5 weeks after tumor implantation and decreased after the fifth week. It was obvious that the tumor volume measurement before this time point was not significantly affected by the factors of tumor hypoxia or necrosis.

Non-invasive imaging using various modalities, including PET, ultrasound and optical imaging, is playing an increasing important role in understating disease

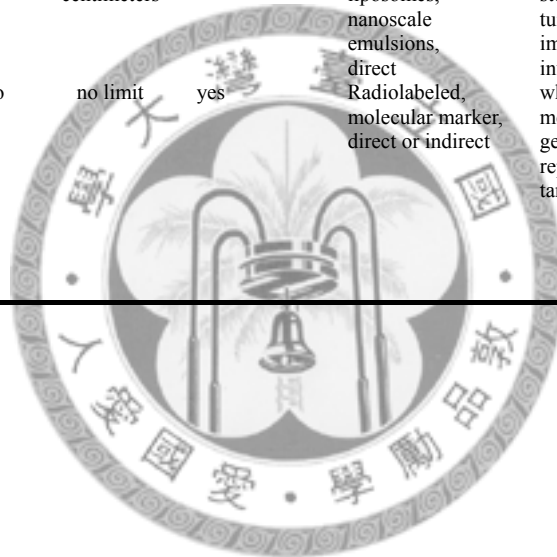
progression, physiology and pathology. The characteristics of microUS and microPET are tabulated in Table 3-2 [51]-[52]. MicroPET imaging allows both the temporal and the spatial biodistribution of a molecular probe to be determined in a single living animal model. [¹⁸F]FDG, a PET reporter probe, has been able to provide both functional and metabolic information for the process of tumor growth in oncology [53]. However, a PET cyclotron is required to produce radioisotope. The radiation needs to be carefully shielded. The real-time nature of microUS, on the other hand, is facilitating in anatomical and hemodynamic studies on small animals, such as mouse embryonic development, *in vivo* transgenic mouse disease models, and image-guided interventions on mice [9]-[11]. Targeted contrast ultrasound may be a particularly effective method for studying the processes of tumor angiogenesis [52]. It detects the molecular imaging of vessel phenotype with information on both perfusion and microvascular blood volume. Bioluminescent imaging has introduced a sensitive, rapid and high throughput alternative for monitoring and tracking tumor development and metastasis in small animals [43]. Bioluminescent imaging is good with very high sensitivity for low levels of signals. However, it is limited mainly for translational research and difficult to be applied in clinical settings. In addition, the tumor volume obtained from bioluminescent imaging is relatively surface weighted and not appropriate to be compared with microUS and microPET.

There are several factors that need to be taken into consideration when using microPET for tumor volume measurements. Firstly, the tumor contour for 3D reconstruction in microPET imaging is difficult to be defined due to tumor necrosis which does not uptake [¹⁸F]FDG. Secondly, the spatial resolution (1.8-2.5 mm) of microPET limits the tumor volume accuracy. Both factors resulted in large tumor volume variations in microPET imaging approach as shown in Fig. 7. Although [¹⁸F]FDG microPET is not adequate for tumor volume measurements under the

situation of hypoxia and/or necrosis developed in large tumor, it does provide information on whole-body metabolism. In addition, high-frequency ultrasonic blood flow measurements, which provide information on tumor vascularity, will allow the applications of microUS/microPET imaging to be extended from the morphological level to the functional and molecular levels.

Table 3-2. Characteristics of microUS and microPET imaging modalities.

Imaging methods	Image generation	Spatial resolution	Temporal resolution	Depth	Translational	Probe for molecular imaging	Application	Advantage	Disadvantage
microUS	high frequency sound	50–500 μm	seconds to minutes	millimeters to centimeters	yes	microbubbles, acoustically active liposomes, nanoscale emulsions, direct	morphological, hemodynamic studies, tumor angiogenesis, image-guided interventions	Real time, hemodynamic	limited spatial resolution, mostly morphological
microPET	high energy γ rays	1–2 mm	10 sec to minutes	no limit	yes	Radiolabeled, molecular marker, direct or indirect	whole body metabolism, gene expression, reporter enzyme targeting	high sensitivity, isotopes can substitute naturally occurring atoms, quantitative translational research	PET cyclotron or generator needed, relatively low spatial resolution, radiation to subject



CH 4. CHARACTERIZATION OF MALIGNANT FOCAL LIVER LESIONS WITH CONTRAST-ENHANCED 40 MHZ ULTRASOUND IMAGING IN HEPATITIS B VIRUS X TRANSGENIC MICE: A FEASIBILITY STUDY

4.1 Hepatocellular Carcinomas in Human

Hepatocellular carcinoma most often occurs in association with cirrhosis or chronic hepatitis. The Hepatitis B virus (HBV) infection is one of the major risk factors for the development of HCC in humans. Given the wide range of treatment options currently available for cirrhotic patients affected with HCC, including surgical resection, transplantation, transarterial chemoembolization (TACE) and percutaneous methods such as ethanol injection, laser and radiofrequency (RF) ablation, timely detection and accurate staging are mandatory so as to determine the best therapeutic outcome. The clinical case shows significant variability, and prognosis is affected by tumor features (such as number and size of nodules, presence of capsule, degree of differentiation, vascular invasion) as well as severity of the underlying chronic liver disease and portal hypertension.

4.1.1 Pathology and Hepatocarcinogenesis

It is currently accepted that hepatic carcinogenesis in the cirrhotic liver is a stepwise process in clinical study [24]. Pathology studies have identified a spectrum

of nodular hepatocellular lesions that occupy an intermediate position between regenerative nodules and well-differentiated HCC. A regenerative nodule is a well-defined region of parenchyma that has enlarged in response to necrosis, altered circulation, or other stimuli. The blood supply is nearly identical to the normal hepatic tissue in the regenerative nodule. Dysplastic nodules are lesions arising in the cirrhotic liver and may be single or multiple. The histological features are cellular atypia without frank malignant changes and development of small arteries without accompanying bile ducts. The premalignant nature of dysplastic nodules has been extensively demonstrated. In pathology, dysplastic nodules are identified at about 8-10 mm and may sometimes reach 15-20 mm. During the process of hepatocarcinogenesis, intranodular hemodynamic changes also occur: whereas regenerative and dysplastic lesions maintain portal blood supply (in normal liver, the portal vein carries most of the afferent blood volume), development of HCC means the appearance of arterialization of the liver parenchyma and capillarization of the sinusoids. In Fig. 4-1, the contrast-enhanced ultrasound can detect hypervascular period of HCC and the histopathology can confirm the features of HCC development. The histopathology can help us to understand the stages of HCC development.

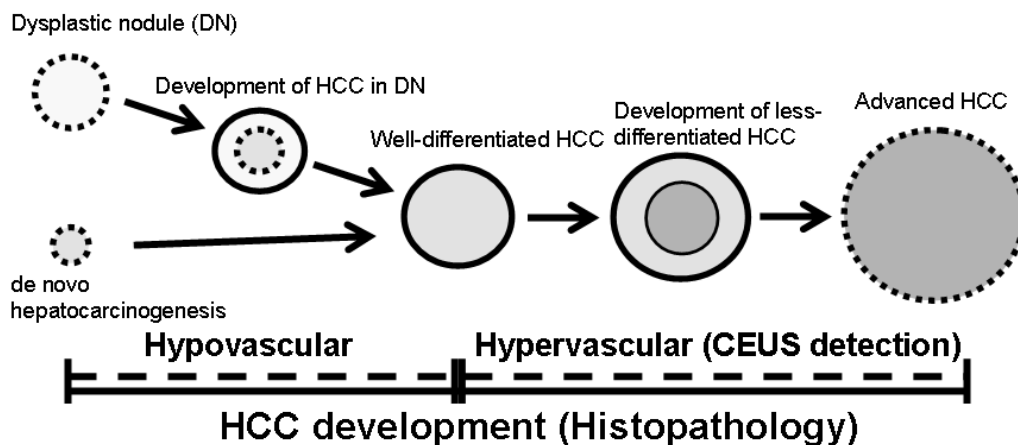


Fig. 4-1. The features of HCC development.

4.1.2 Unenhanced Sonography

Ultrasound (US) is the most common examination in screening of patients at high risk of developing hepatocellular carcinomas such as alcoholic, hepatitis B and C patients. Small tumors (< 3 cm in diameter) in liver are hypoechoic and uniform in appearance, but some lesions may appear hyperechoic due to fatty change. Larger HCCs are usually heterogeneous with mixed hyper- and hypoechogenicity. The reported detection rate of HCCs measuring less than 2 cm in diameter has been variable, ranging from 46% to 95% [54]-[55], with accurate detection of 82%–93% of HCCs measuring between 2 and 3 cm. For HCCs smaller than 1 cm, the detection rate by US is considerably lower and ranges between 13% and 37% [55].

4.1.3 Contrast Enhanced Sonography

Contrast-enhanced ultrasound (CEUS) has been used to evaluate known or suspected focal liver lesions. In this technique, the contrast between the lesion and normal liver parenchyma was evaluated during three vascular contrast phases, i.e. arterial, portal-venous and late phase [22]. Hepatocellular carcinoma (HCC) is a primary liver malignancy in humans that most often occurs in association with cirrhosis or chronic hepatitis [21]. The portal vein carries most (75%) of the afferent blood volume in the normal liver, where HCC results in cirrhosis-induced arterial neoangiogenesis [23] and thus hypervascularity. The increased arterial supply in HCC is proportional to its size and grade. In contrast, the blood supply of the portal vein decreases during the early steps of carcinogenesis [24]-[25]. CEUS imaging plays an important role in the clinical diagnosis of this disease, providing information on the hemodynamic changes of the HCC and aiding detection of the blood supply peculiar to HCC. The real-time scanning capabilities of ultrasound also allow the evaluation of

small lesions that are unclear on computed tomography or magnetic resonance imaging [26]-[27]. Previous studies have found that HCC can be characterized by rapid intensity enhancement in the arterial phase (15–25 seconds after contrast injection), a rapid washout in the portal phase (45–90 seconds after contrast injection), and intensity enhancement of liver parenchyma in the parenchyma phase (90–240 seconds after contrast injection) [21].

High-frequency ultrasound (i.e., higher than 20 MHz) [9]-[11] has been used for noninvasive real-time imaging of small animals, and can achieve a spatial resolution of less than 100 μm . In preclinical liver metastasis models, high-frequency ultrasound imaging has been used to measure the tumor volume, assess metastatic progression, and evaluate chemotherapeutics [45]-[46]. The main purpose of this study was to determine the potential of assessing malignant focal liver lesion using contrast enhanced high-frequency ultrasound imaging on small animals for preclinical research. Moreover, three vascular contrast phases were characterized and identified. The center frequency used in this study was 40 MHz, for which the spatial resolution is approximately 75 μm at the focus [12]. Albumin-shelled microbubbles were used as the contrast agent and imaging was done at low MI (0.14-0.18). The imaging system and contrast agent were used to characterize focal liver lesions in Hepatitis B virus X (HBx) transgenic mice.

After injecting microbubbles, the intensity enhancement in the vessels within a suspected malignant focal lesion during the arterial phase is potentially for the detection of HCC angiogenesis. In addition, the decrease in the intensity of the suspected HCC lesion during the venous phase is also an important characteristic of HCC because typical tumors lack a portal venous supply [27]. It has also been shown that microbubbles with albumin shells were likely to be phagocytosed by Kupffer cells, and hence the delayed parenchymal-phase images of CEUS imaging can also

reflect the number and function of Kupffer cells in cirrhosis [56]. The time–intensity curve (TIC) has been used with CEUS imaging in clinical settings [57]. In the present study, the TICs were acquired for 30 minutes after contrast injection for identifying and characterizing malignant focal liver lesions in HBx transgenic mice. TICs of suspected HCC lesions and liver parenchyma were calculated. The results were also arranged according to the guidelines of European Federation of Societies for Ultrasound in Medicine and Biology (EFSUMB) [58] and histopathology findings. According to the guidelines of EFSUMB, the arterial phase is important for demonstrating hypervascularity of HCC and hypervascular metastases. Benign solid lesions are characterized by persistence of contrast enhancement during the portal-venous and late phase. The typical enhancement patterns are summarized according the features in different types of lesions in the guidelines of EFSUMB.

4.2 Transgenic Mouse Model

The generation of HBx transgenic mice that develop HCC has been described previously [59]. A liver-specific transgenic vector, pAlb-In-pA-HS4, containing the mouse albumin promoter, a 0.33-kb synthetic intron, and a 0.28-kb bovine growth hormone poly(A) signal was constructed. The albumin-HBx transgenic plasmid was constructed by placing the X gene of the HBV ayw subtype into the *Sall* and *PmeI* sites of the pAlb-In-pA-HS4 vector. The albumin-HBx transgenic mice were made by microinjecting the DNA into the pronucleus of fertilized eggs of C57BL/6 mice. The HBx transgenic mice started to develop HCC at around 14 to 16 months of age. At 19-20 months, the incidence of HCC in HBx transgenic male mice was about 90-100%. Pathological examination revealed that HCC was present in 27% of the female HBx transgenic mice [59]. The suspected focal liver lesions in the livers were

imaged in ten male, HBx transgenic mice using a 40 MHz ultrasound imaging system and confirmed by surgery inspection. To investigate gender differences, 40 MHz ultrasound imaging was also performed for the suspected focal liver lesions in three female, HBx transgenic mice. The CEUS imaging was performed on the HBx transgenic mice between 13 and 22 months of age. During 16-22 months of age, the suspected focal liver lesions were detected.

4.3 Microbubbles for High-Frequency Ultrasound Imaging

The ultrasound contrast agent used in this study comprised microbubbles with albumin shells, and is similar to the commercial ultrasound contrast media Optison™ [60]-[61]. The gas enclosed in the microbubbles is perfluoropropane (C_3F_8). The homemade albumin-based microbubbles were produced by sonication of 10-mL solution containing 0.9% sodium chloride, 6.6% human serum albumin (Octopharma AG, Switzerland) and perfluorocarbon (C_3F_8) gas. The solution was sonicated by ultrasound sonicator (Branson, USA) for 2 min. The number of microbubbles in each solution was measured with MultiSizer III (Beckman Coulter) with 30 μ m aperture probe, whose measurement boundary is between 0.6 to 20 μ m. The concentration of the microspheres ranges 4.24–8.43 $\times 10^8$ /ml. The mean diameter number size is 0.7–2.0 μ m. Phantom experiments were performed to characterize the microbubbles. The cylindrical phantom was made of 2% agarose gel (2 g of agarose powder mixed with 98ml of pure water in a beaker) with a chamber to load the contrast agents and at its center contained a region of $2 \times 2 \times 20$ mm³ with injected microbubbles that were diluted to a concentration of 1% by volume in saline. The 8-bit, 200-M samples/s arbitrary-function generator (DAC200, Signatec, CA, USA) was used to generate the

desired transmit waveform, which then was sent to a power amplifier (25A250A, Amplifier Research, PA, USA) to drive the lithium-niobate focused transducer. The scan-line data acquired at each position were sent to an ultrasonic receiver (5900 PR, Panametrics, MA, USA). Finally, the signal was sampled with a 500-MHz digitizer (PDA500, Signatec). The center frequency of the single-crystal lithium niobate transducer (NIH Resource Center for Medical Ultrasonic Transducer Technology, PA, USA) was 45 MHz. The -6dB beam width at the focus at this frequency is $75\ \mu\text{m}$ [9, 12]. All experiments employed the transmission of three cycles of 20, 25, 40, and 50 MHz sinusoid. The transducer had a fixed focus at 12 mm. The acquired signals were recorded on the hard disk of a personal computer and processed using Matlab (Mathworks, Natick, MA, USA). The RF data were processed and were used to calculate the image intensity before the images were normalized. The contrast between the background (phantom) and the microbubble region was measured to determine the optimal imaging frequency for *in vivo* studies.

Images obtained using high-frequency ultrasound imaging with the contrast phantom at 20, 25, 40, and 50 MHz are shown in Fig. 4-2(a), (b), (c), and (d), respectively. The contrast values of the 100-fold-diluted microbubbles relative to the background were 16.1, 18.8, 24.8, and 20.2 dB at 20, 25, 40, and 50 MHz, respectively, and hence 40 MHz was used in subsequent *in vivo* imaging.

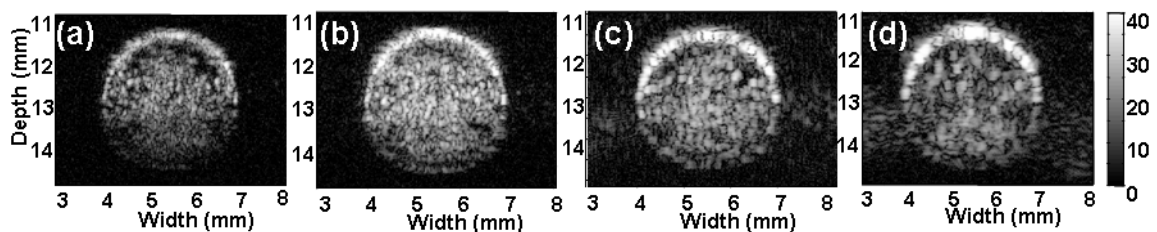


Fig. 4-2. Ultrasound B-mode images of the region in the agarose phantom containing albumin-shelled microbubbles using ultrasound at 50 MHz (a), 40 MHz (b), 25 MHz

(c), and 20 MHz (d).

4.4 Small-Animal High-Frequency Ultrasound Imaging

Figure 4-3 shows a block diagram of the custom-made real time high frequency ultrasound scanner consists of a scanning head, a pulser/receiver, ADC/DAC and FPGA. The center frequency of the system can be varied from 20 to 50MHz and frame rate from 1 Hz to 10 Hz. In our experiments, 3-cycle pulse wave with center frequency of 40 MHz was used, and the frame rate was 2 to 5 Hz. For real time ultrasound system, 400 images were recorded as a binary data set. Images were obtained before and after contrast agent administered. The RF data were processed and were used to calculate the image intensity before the images were normalized by Matlab (Mathworks, Natick, MA, USA).

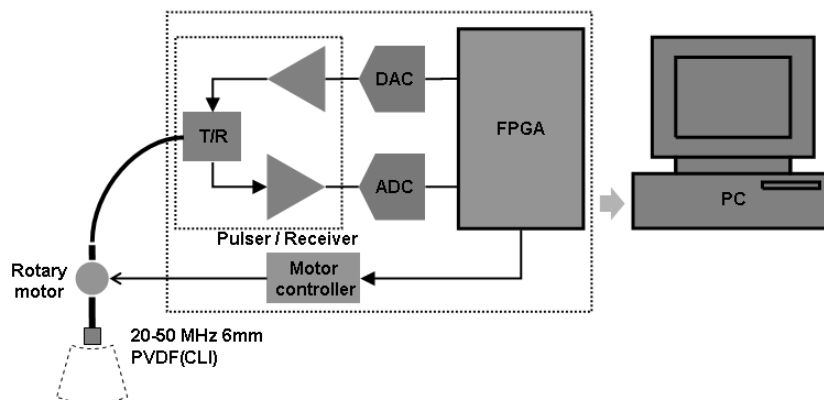


Fig. 4-3. Block diagram of the 40 MHz ultrasound imaging system.

The protocol of the high-frequency ultrasound imaging is illustrated in Fig. 4-4. HBx transgenic mice bearing focal liver lesions were anesthetized and laid down in an animal holder. The abdominal hair of the HBx mouse was clipped, and acoustic gel

was applied to the abdomen. High-frequency ultrasound imaging was applied to the entire livers of HBx mice. After identifying suspected focal liver lesions by a radiologist, about $0.85\text{-}1.69 \times 10^8$ (0.15-0.2 ml) microbubbles were injected through the lateral tail vein, and post-contrast-injection imaging of the suspected focal liver lesions was immediately performed for 30 minutes. All of the data were used for the measurement of TICs and characterization of suspected focal liver lesions.

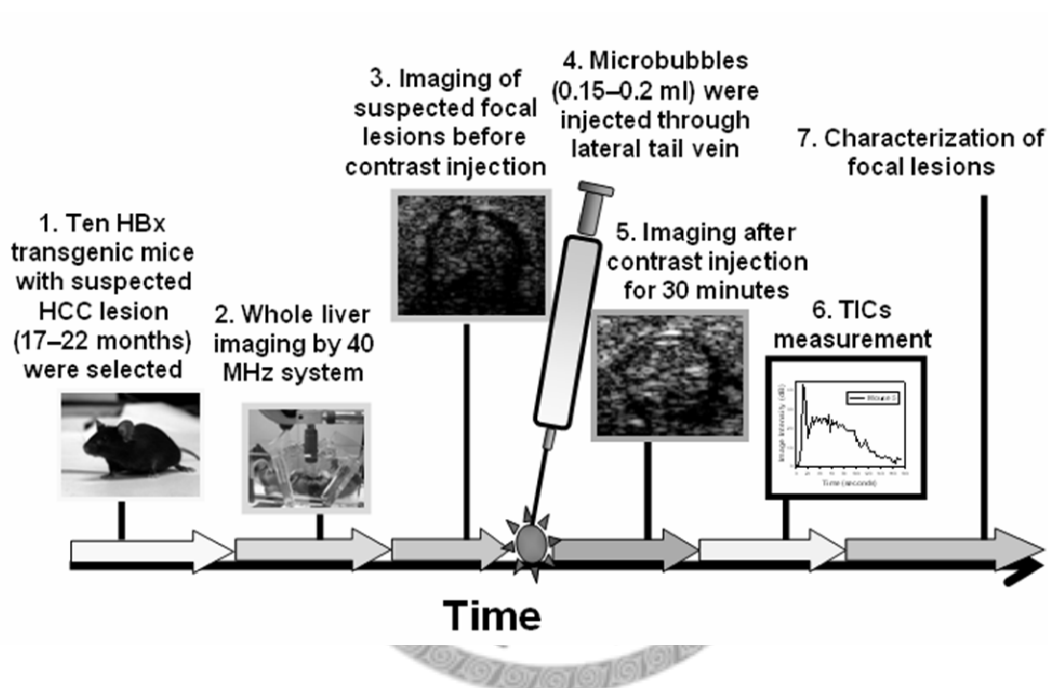


Fig. 4-4. Protocol for CEUS imaging of HBx transgenic mice.

4.5 Contrast-Enhanced Ultrasound Imaging at 40 MHz

Contrast-enhanced 40 MHz ultrasound B-mode imaging was applied to the thirteen mice. The mechanical index (MI) was measured from the equation as following:

$$MI = \frac{P_{0.3}}{\sqrt{f_c}}$$

where $P_{0.3}$ is the peak rarefactional pressure derated by 0.3 dB/cm/MHz and f_c is

the center frequency. The acoustic pressure of the transducer was calibrated by a needle-type hydrophone (MHA150, FORCE Technology, Brøndby, Denmark). The acoustic peak pressure induced by the 40-MHz transducer was measured at 1.19 MPa in water. In this study, the MI was 0.188 used to perform contrast enhanced imaging. Hence, no microbubble destruction was expected during imaging. Each mouse was anesthetized with halothane vapor using an anesthesia system (Surgivet, WI, USA). B-mode imaging was first performed before injecting the microbubbles. One transverse section of the suspected focal lesion in the liver was selected. Image acquisition started within 1 second of microbubble injection. Regions of interest (ROIs) were selected in the suspected focal lesions (shown in figure 4-5(a)), vessels within the lesions (shown in figure 4-5(b)), and liver parenchyma (shown in figure 4-5(c)) by a radiologist. The image intensity was calculated in each ROI using Matlab (Mathworks, Natick, MA, USA), with the mean constituting a data point in the TIC.

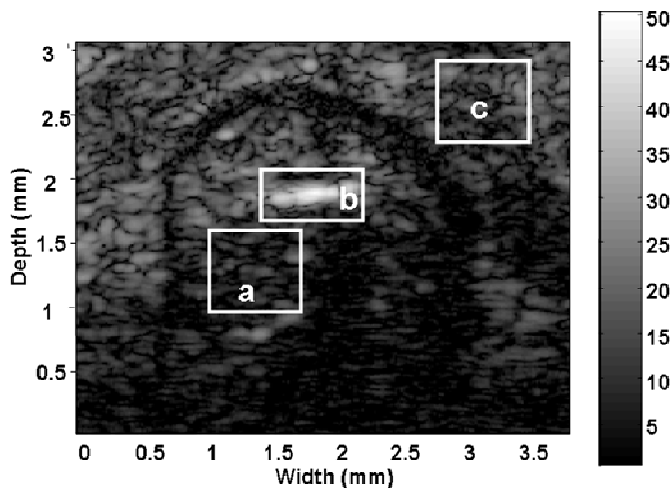


Fig. 4-5. Regions of interest (ROIs) were selected in the suspected focal lesions (a), vessels within the lesions (b), and liver parenchyma (c).

The size of ROIs depended on the lesion size, and ranged from 1×1 to 1×0.5 mm^2 . In this study, the arterial phase was defined as the time period in which the TIC

in the suspected focal lesion exhibited a distinct peak within 90 seconds after contrast injection. The image intensity within 30 minutes of contrast injection was calculated for suspected focal lesions, vessels within the lesions, and liver parenchyma. And finally, the contrast between the suspected focal lesion and liver parenchyma within 30 minutes was measured.

The mean image intensity of focal liver lesions in the ten male mice increased by 5.4 dB during the arterial phase. Characteristics of liver lesions in the thirteen mice were summarized in table 4-1. In table 4-1, CEUS of the liver provides different parenchymal or tumoral enhancement on the different phases of contrast enhancement of the liver, which are summarized. The incidence of malignant lesions in HBx transgenic male mice was about 90-100%. However, only one of the three female HBx transgenic male mice developed HCC. In Fig. 4-6(b), the image intensity of the hypervascular metastases lesion in mouse 2 increased to a peak at 19 seconds. The surrounding vessels of the suspected HCC lesion were enhanced at 61 seconds, as shown in Fig. 4-6(c). Figure 4-6(d) shows that the washout phase was reached at about 2 minutes, and also that the image intensity of the liver parenchyma began to increase. Figure 4-7(a) and 4-7(b) show images of mouse 2 acquired before and 3 minutes after contrast injection, respectively. The arrows in Fig. 4-7(c) point to the margin of the tumor, with enhancement clearly evident at 30 minutes after contrast injection. The box in Fig. 4-7(c) shows that enhancement of the vessels in the malignant lesion was clearly evident at 30 minutes after contrast injection. And it is compared with the histology results shown in Fig. 4-7(d). In table 4-1, the complete chaotic vessels were revealed during the arterial phase in mouse 2. The chaotic vessels were shown in different area of HCC lesion during the three vascular contrast phases. During arterial phase, the focal liver lesion shows hyper-enhancing. The iso-enhancing and hypo-enhancing properties were shown during portal and late

phase. The tumor entity was defined as the hypervascular metastases lesion by the image property and histology.

Figure 4-8 shows images of a HCC lesion (mouse 5) before contrast injection (a) and at 14 seconds (b), 16 seconds (c) and 2 minutes (d) after contrast injection. Panels (c) and (d) also show characteristics of chaotic vessels. In table 4-1, the uncomplete chaotic vessels were revealed during the three phase in mouse 5. During the three phases, the hyper-enhancing, iso-enhancing and hypo-enhancing were also shown. The tumor entity was defined as the typical hepatocellular carcinoma by the image properties and histology. Figure 4-9(a) shows the HCC lesion in mouse 6 before contrast injection and Fig. 4-9(b) shows the hyper-enhancing feature in HCC lesion after contrast injection at 13 seconds. In Fig. 4-9(c), the HCC lesion shows the hypo-enhancing feature at 30 minutes after contrast injection. In table 4-1, no chaotic vessels were revealed during the three phase in mouse 6. However, during the three phases, the hyper-enhancing, iso-enhancing and hypo-enhancing properties were shown. The tumor entity was defined as the hepatocellular carcinoma by the image properties and histology. Figure 4-10(a) shows the hypovascular metastases lesion in mouse 9 before contrast injection. In Fig. 4-10(b) and table 4-1, the hyper-enhancing and rim enhancing features were shown during arterial phase. The hypo-enhancing feature at 30 minutes after contrast injection is shown in Fig. 4-10(c). The tumor entity was defined as the hypovascular metastases lesion by the image properties and histology. In three female HBx transgenic mice, the malignant lesion was detected only on mouse 13 (Fig. 4-11). Figure 4-11(a) shows the HCC lesion before contrast injection and Fig. 4-11(b) shows the hyper-enhancing feature in HCC lesion after contrast injection at 10 seconds. In mouse 13, the uncomplete chaotic vessels were revealed during the three phase and were arranged in table 1. During the three phases, the typical properties of hyper-enhancing, iso-enhancing and hypo-enhancing were

shown. The tumor entity was defined as the hepatocellular carcinoma by the image properties and histology. Figure 4-12 shows non-enhancing features in focal lesion of mouse 11 before (Fig. 4-12(a)) and after (Fig. 4-12(b)) contrast injection. In mouse 11, the enhancement patterns were similar during the three phases. The tumor entity was defined as the focal nodular hyperplasia (FNH) by the image properties and histology.

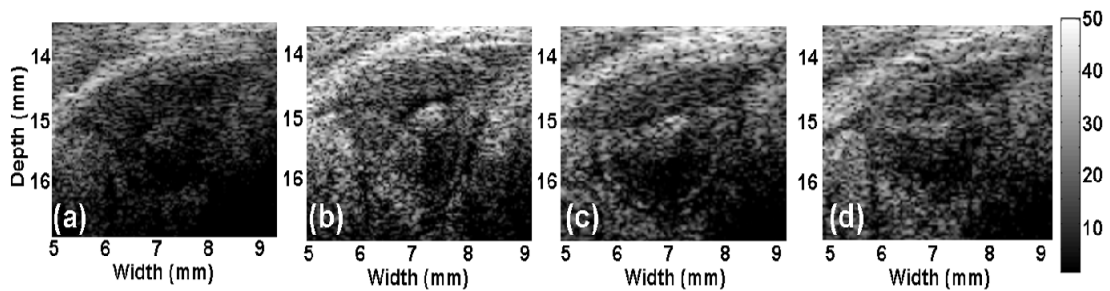


Fig. 4-6. Hypervascular metastases lesion in mouse 2 before contrast injection (a), at 19 seconds (b), at 61 seconds (c), and 2 minutes (d) after contrast injection.

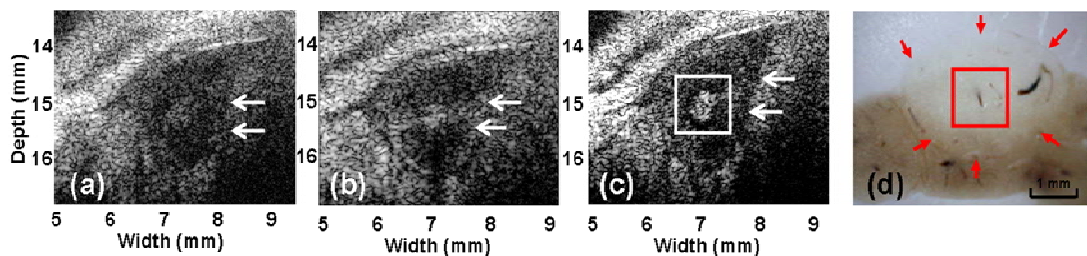


Fig. 4-7. Hypervascular metastases lesion in mouse 2 before contrast injection (a) and at 2 minutes (b) and 30 minutes (c) after contrast injection. Arrows point to margins of lesion enhancement as clearly evident at 30 minutes after contrast injection. Box indicates the vessels in the hypervascular metastases lesion. Panel (d) shows the anatomy of the hypervascular metastases lesion after fixation in 10% formalin.

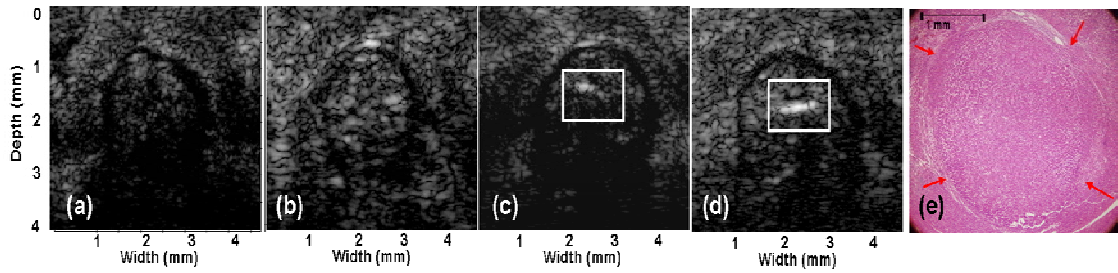


Fig. 4-8. Images of HCC lesion in mouse 5 before contrast injection (a) and at 14 seconds (b), 16 seconds (c) and 2 minutes (d) after contrast injection. Panels (c) and (d) show the characteristics of chaotic vessels. Panel (d) shows the histology result of the HCC lesion.

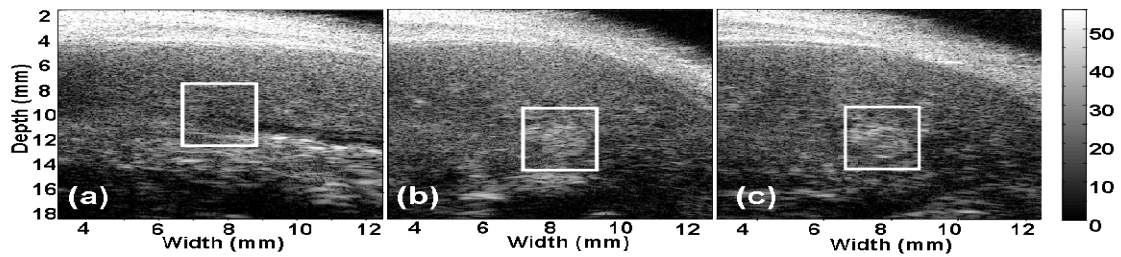


Fig. 4-9. HCC lesion in mouse 6 before contrast injection (a) and the hyper-enhancing feature during the arterial phase (b). Panel (c) shows the hypo-enhancing feature at 30 minutes after contrast injection.

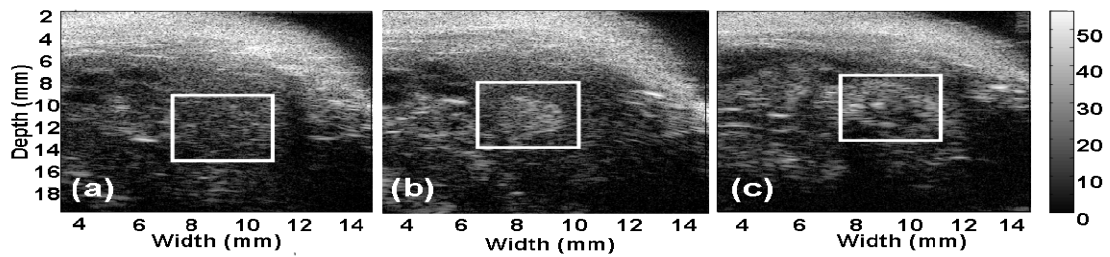


Fig. 4-10. The hypovascular metastases lesion in mouse 9 before contrast injection is shown in panel (a). Panel (b) shows the hyper-enhancing, rim enhancing, and non-enhancing (necrosis) features during the arterial phase. Panel (c) is the hypo-enhancing feature at 30 minutes after contrast injection.

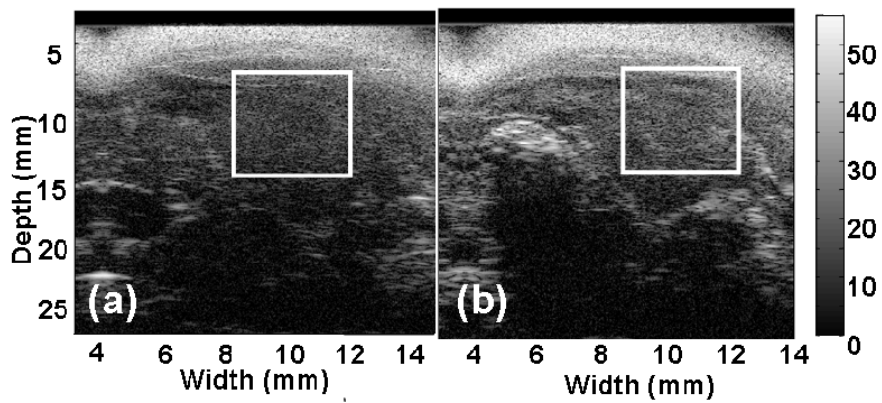


Fig. 4-11. HCC lesion in mouse 13 before contrast injection (a) and the hyper-enhancing feature during arterial phase (b).

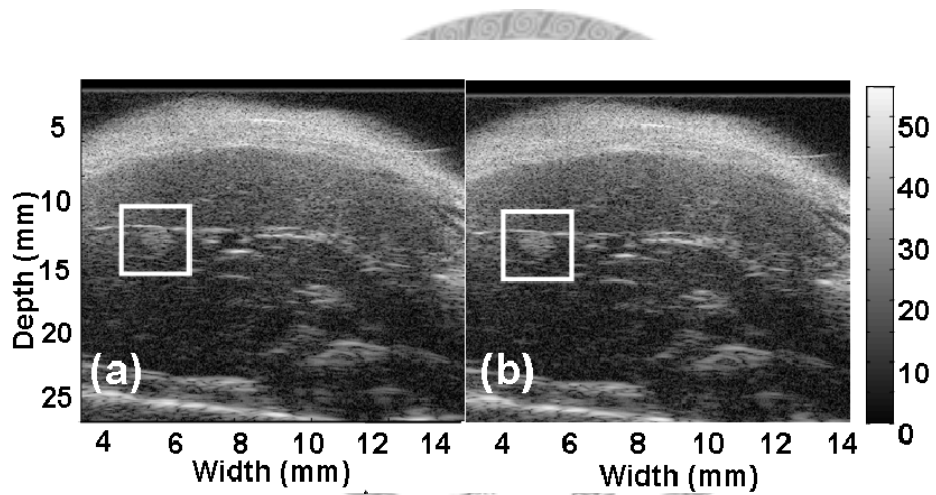


Fig. 4-12. The focal nodular hyperplasia (FNH) lesion in mouse 11 before (a) and after (b) contrast injection.

Table 4-1. Characterization of focal liver lesions according to the guidelines of EFSUMB (E: Enhancement).

Mouse	Age / gender (month/ male (M), Female (F))	Lesion Diameter (mm)	Vessels in Tumor	Arterial Phase		Portal Phase		Late Phase		Tumor Entity
				Time period	Enhancement pattern	Time period	Enhancement pattern	Time period	Enhancement pattern	
1	18/M	2.3	no	5-40s	hyper-enhancing	40s-10min	iso-enhancing	10-30min	hypo-enhancing	HCC
2	18/M	3.2	yes	5-40s	hyper-enhancing, complete chaotic vessels	40s-10min	iso-enhancing chaotic vessels	10-30min	hypo-enhancing chaotic vessels	Hypervascular metastases
3	22/M	2.5	no	8-25s	hyper-enhancing	25s-10min	iso-enhancing	10-30min	hypo-enhancing	HCC
4	20/M	2.5	no	no	iso-enhancing	no	iso-enhancing	no	hypo-enhancing	DN
5	18/M	2.2	yes	14-60s	hyper-enhancing, chaotic vessels	60s-10min	iso-enhancing chaotic vessels	10-30min	hypo-enhancing chaotic vessels	HCC
6	16/M	3	no	2-40s	hyper-enhancing	40s-10min	iso-enhancing	10-30min	hypo-enhancing	HCC
7	17/M	2.15	yes	11-21s	hyper-enhancing, chaotic vessels	21s-10min	iso-enhancing chaotic vessels	10-30min	hypo-enhancing chaotic vessels	HCC
8	18/M	1.2	no	4-40s	complete E, rim E	40s-10min	hypo-enhancing	10-30min	hypo-enhancing	Hypovascular metastases
9	16/M	3.2	no	2-43s	complete E, rim E, non-enhancing areas (necrosis)	43s-10min	hypo-enhancing	10-30min	hypo-enhancing	Hypovascular metastases
10	16/M	3	yes	2-34s	hyper-enhancing, chaotic vessels	34s-10min	iso-enhancing chaotic vessels	10-30min	hypo-enhancing chaotic vessels	HCC
11	17/F	0.8	no	no	hyper-enhancing	no	hyper-enhancing	no	hyper-enhancing	FNH
12	17/F	2.1	no	no	no	no	no	no	no	Cyst
13	17/F	3.5	yes	4-51s	hyper-enhancing, chaotic vessels	51s-10min	iso-enhancing chaotic vessels	10-30min	hypo-enhancing chaotic vessels	HCC

4.6 Time–Intensity Curves

In this study, the TICs were acquired for short-time observation (90 seconds) and long-time observation (30 minutes). The 90-second TICs of the ten male HBx transgenic mice are shown in Fig. 4-13. The enhancement in the arterial phase was calculated by subtracted the baseline value (i.e., mean value of the baseline image) 60 seconds before injection from the peak value. In the arterial phase, a distinct peak in image intensity is observed. In Fig. 4-13, the peak intensity of mouse 1, mouse 2, mouse 3, mouse 5, mouse 6, mouse 7, mouse 8, mouse 9 and mouse 10 was 1.29, 2.17, 16.1, 7.15, 7.96, 4.56, 12.56, 10 and 4.59 dB higher than the baseline, respectively. However, the peak intensity cannot be observed in mouse 4. For malignant focal liver lesion, the TICs rise and reach the peak during artery phase. The portal phase initiates when the TICs start to fall back to the base line. Two minutes after contrast injection, the image intensity of liver parenchyma noticeably increased. The mean intensity of the liver parenchyma image peaked at 30 minutes after contrast injection. Figure 4-14 shows the contrast of suspected focal lesions and liver parenchyma using data from the nine mice (not including mouse 4). Within 10 minutes after contrast injection, the contrast increased gradually. During 10 to 30 minutes, the contrast increased more significantly so that the lesion boundary became clear. The time period from 10 to 30 minutes post contrast injection was defined as the late (parenchyma) phase. The mean contrast between the liver parenchyma and the suspected focal lesion reached the maximum at 30 minutes after contrast injection, as shown in Fig. 4-14. The mean contrast was 7.74 dB higher at 30 minutes after contrast injection than before contrast injection. Figure 4-15 shows the mean image intensity of the vessels within suspected focal lesions. The image intensity of the vessels within suspected focal lesions increased gradually from 10 to 30 minutes.

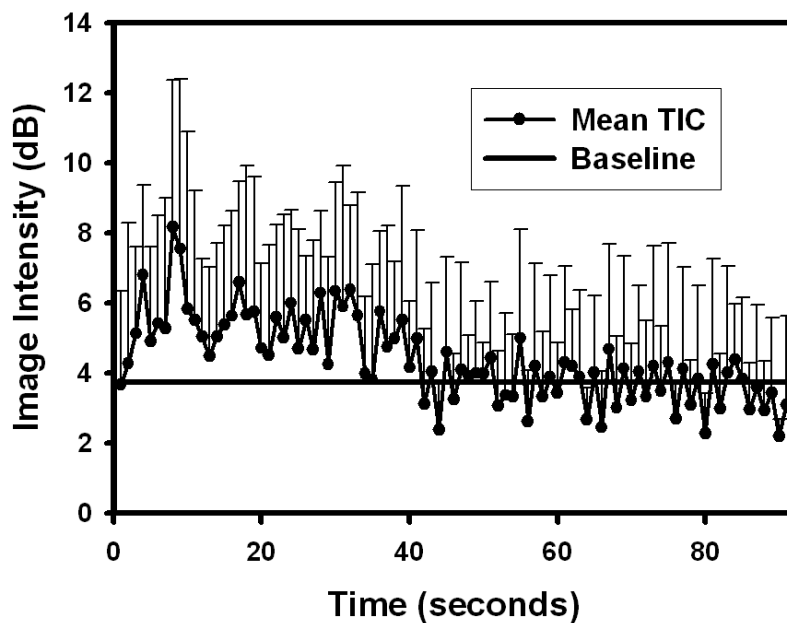


Fig. 4-13. Mean TICs of the focal liver lesions in the ten male mice were drawn within 90 seconds after contrast injection. The baseline value was calculated by the mean value of the baseline image from the ten mice. The arterial phase was defined as the time period that the image intensity increases and recovers to the baseline.

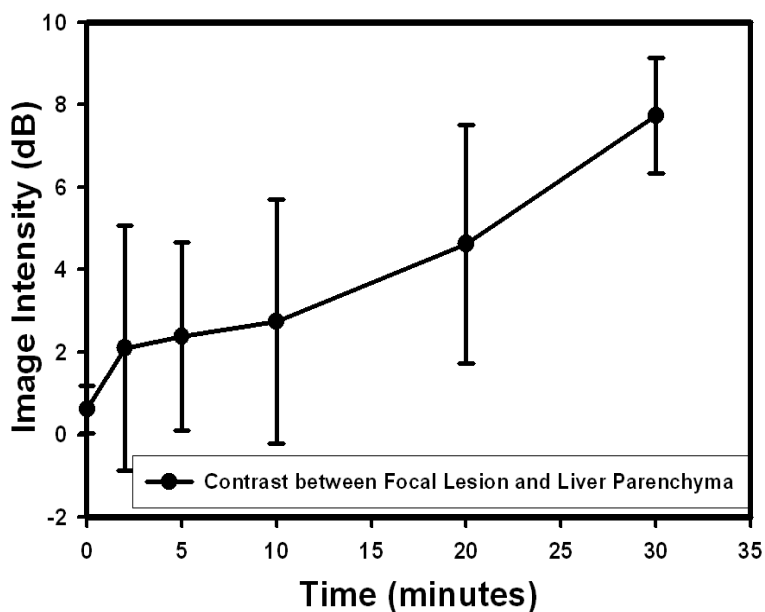


Fig. 4-14. This figure shows that the mean contrast between focal lesion and liver parenchyma reached the maximum at 30 minutes after contrast injection. During 10 to 30 minutes, the slope increases and is defined as the late phase in this study.

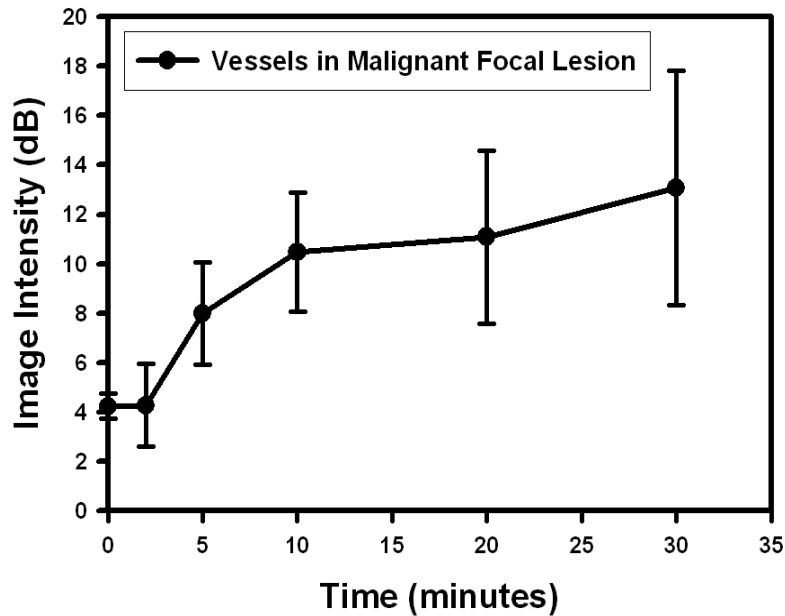


Fig. 4-15. This figure shows the mean image intensity of vessels in focal lesion in mouse 2, 5, 7, 10 within 30 minutes after contrast injection. The image intensity increases within 30 minutes.

4.7 Histopathology

The mice were euthanized after performing ultrasound imaging, and the suspected focal nodules were removed *en bloc* and fixed in 10% formalin. Sections were prepared for light-microscopy evaluation. Hematoxylin and eosin stain was applied to assess overall tumor morphology and regional viability. Blood vessels were also identified by a pathologist. Small malignant lesion is characterized histopathologically by the disappearance of portal tracts and an increased number of unpaired arteries [21].

4.8 Characterization of Focal Liver Lesion

Table 1 summarizes the main ultrasound image features of liver lesions during the three contrast phases. Histopathology was used to confirm the benign and malignant

features in the thirteen mice. The incidence of malignant focal lesion development is up to 90% in male HBx transgenic mice. Specifically, the suspected focal liver lesions in mouse 1, 2, 3, 5, 6, 7, 8, 9 and 10 were confirmed as malignant. Only the mouse 4 was confirmed as a premalignant focal lesion, dysplastic nodule (DN). In the three female HBx transgenic mice, only mouse 13 showed malignant features in the focal lesion. A focal nodular hyperplasia (FNH) and a cyst lesion were observed in mouse 11 and 12, respectively. In this study, pathology was characterized as a gold standard by a pathologist. Comparing the imaging and the pathology results, the sensitivity, specificity and accuracy of CEUS for the detection of malignant focal liver lesion in HBx transgenic mice were 91%, 100% and 92%.

4.9 Discussions

Detection of arterial hypervascularity is very important to diagnosing HCC and malignant lesions in the liver because it is one of the most reliable characteristics of nodular HCC. In clinical settings, most CEUS images show classic arterial-phase hypervascularity in HCC, with the TIC rapidly reaching a maximum. Washout during the venous phase is also an important characteristic of HCC because typical tumors lack a portal venous supply. Previous results were all from human (i.e., clinical studies), the main purpose of this study was to extend this to small animals and to investigate the feasibility of using CEUS in preclinical research. It was found that CEUS imaging was an effective technique for detecting the intensity enhancement in the arterial phase and the late phase in the presence of a malignant lesion.

Goertz and colleagues have demonstrated conclusively that subharmonic contrast imaging can suppress the tissue signal and enhance the detection of blood area [62, 63]. However, the knowledge of the resonant behavior of the homemade

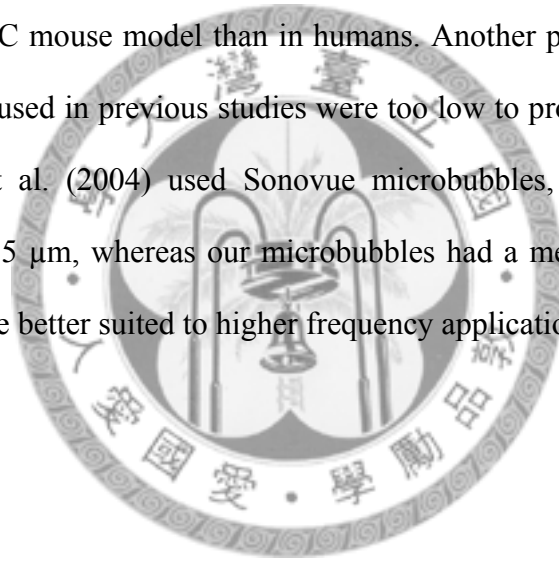
albumin-based microbubbles is limited. In our study, the nonlinear scattering of the homemade albumin-based microbubbles is not obvious. The effects of the subharmonic contrast imaging are not clear and the suppression of the tissue signal is not performed well.

In Fig 4-13, the peak of mean image intensity for the malignant lesion in mice 1, 2, 3, 5, 6, 7, 8, 9 and 10 increased by about 7.36 dB during first 40 seconds after contrast injection, whereas the enhancement was -0.02 dB during this time period in mouse 4. The mouse 4 at 20 months was not easy to identify the characteristic enhancement in the arterial phase by TICs, and the suspected focal liver lesion in this mouse 4 was confirmed histopathologically as a dysplastic nodule, which is defined as a nodule lesion of hepatocytes at least 1 mm in diameter with dysplasia but without definite histologic criteria of malignancy [64]. A dysplastic nodule is hypovascular, and most HCCs develop from premalignant lesions such as dysplastic nodules.

In Fig. 4-14, the mean contrast between the HCC lesion and liver parenchyma increased 7.74 dB at 30 minutes after contrast administration. In Fig. 4-15, the image intensities of vessels within malignant focal lesion increased to maxima at 30 minutes after contrast administration. Nonetheless, the chaotic vessels were not shown in the portal and late phase in the guidelines of EFSUMB. In Fig. 4-7, arrows point to the margin of the tumor and enhancement is clearly evident at 30 minutes after contrast injection. These results show that the image intensity of liver parenchyma peaked at this time point. The albumin-shelled microbubbles are thought to be phagocytosed by the Kupffer cells in the liver parenchyma of the HBx transgenic mice [56]. In previous report, about 1.2×10^6 microbubbles were injected into the mouse. In this study, the concentration of homemade albumin-based microbubbles ranges $0.85\text{-}1.69 \times 10^8$ (0.2 ml) were injected through the lateral tail vein in the mouse. The dose of the microbubbles may be too much to metabolize in the liver. Otherwise, most

albumin (40%-60%) is degraded in muscle, liver, and kidney [65]. The albumin-based microbubbles were metabolized by liver and the remaining microbubbles may accumulate in the vessels of liver. CEUS imaging can reflect the number and function of Kupffer cells in cirrhosis and the function of the HCC liver are not as well as the cells in normal liver. Therefore, the parenchymal enhancement (Fig. 4-14) is not significant and the vessel enhancement (Fig. 4-15) continuing for 30 minutes.

Contrast harmonic ultrasound imaging has been widely applied at lower frequencies, but at 15 MHz this did not improve the identification of HCC lesions in a transgenic mice model [66]. One possible reason is that the hypervascularity is less important in the HCC mouse model than in humans. Another possible explanation is that the frequencies used in previous studies were too low to provide adequate spatial resolution – Mai et al. (2004) used Sonovue microbubbles, which have a mean diameter of about 2.5 μm , whereas our microbubbles had a mean diameter of about 1.2 μm and hence are better suited to higher frequency applications [67].



CH 5. CONTRAST IMPROVEMENT IN ULTRASOUND NONLINEAR IMAGING USING EEMD

Ultrasound harmonic imaging is a method in which the higher harmonic echoes (usually the second harmonic) are selectively used for imaging. In ultrasound harmonic imaging, ultrasound contrast agent enclosed gas produces strong backscattered signal from blood because of the acoustic-impedance mismatch between blood and air [68, 69]. Clinically, harmonic signals from ultrasound contrast agent is used routinely to enhance the image contrast between blood flow and tissue. According to the advantage of the nonlinear response of the contrast agent, contrast harmonic imaging increases the contrast-to-tissue ratio (CTR). However, the surrounding tissue produces significant harmonic echoes and the improvement of contrast harmonic imaging is limited.

Ultrasound contrast imaging modalities include fundamental, second harmonic, subharmonic, harmonic power Doppler and pulse-inversion (PI). Fundamental B-mode imaging results in poor contrast agent detectability in the presence of tissue [70]. Second harmonic (B-mode) imaging is based on contrast agent-specific properties and is a method where the ultrasound system separates the harmonic frequencies of the received signal from the fundamental frequencies and then processes the harmonic signal alone [71]. It utilizes the significant nonlinear response exhibited by microbubble oscillation when the frequency of the impinging sound wave is near the resonance frequency of the bubble [72]. Although second harmonic imaging generally exhibits better contrast detection than does linear imaging, its performance is still often limited by the tissue also exhibiting a significant nonlinear response associated with finite amplitude distortion, especially with high mechanical index. Unlike with second harmonic imaging, advantage of subharmonic imaging is

that, the contribution of tissue is minimal at acoustic pressures currently used in diagnostic ultrasound, which will result in a high CTR [73]. However, narrow-band signals are needed because the generated subharmonic components will be more dominant when the numbers of periods increase. [74] Harmonic power Doppler is a more sensitive method in terms of signal-to-noise ratio and low flow detectability [75]. But tissue motion generates Doppler signals (clutter) that can be even stronger than the contrast-enhanced signals with the same Doppler shift frequencies, such as the signals from blood.

Instead of conventional filtering, the PI technique is an alternative method to extract the contrast harmonic signal [76]–[78]. In PI technique, a pulse is transmitted in the first firing, and then, the same pulse is inverted and transmitted again in the second firing. The echoes in both firings are summed together to obtain a beam. Briefly, the original type of PI imaging involves extracting the second-harmonic component of the received echo whereas PI fundamental imaging extracts the contrast nonlinear signal in the fundamental band. In both cases, a pair of inverted pulses is transmitted and the corresponding echoes are summed. For tissue, the received echo can be modeled as a polynomial function of the fundamental signal such that only even harmonics are kept. For contrast agents, however, it has been shown that the echoes change from inverted to time-shifted versions of each other as the driving amplitude increases [79]–[80]. Therefore, an uncanceled component exists in the fundamental band of the summed signal. Note that although this component is used to form an image, it remains a nonlinear imaging method because the component is generated due to the nonlinear response of the microbubbles. In previous study, the use of Levovist® increases the contrast by up to 20 dB compared with conventional linear imaging was demonstrated [76]. Following the success of the previous study, the present study investigated the efficacies of using ensemble empirical mode

decomposition (EEMD) in PI fundamental imaging.

Hilbert-Huang transform (HHT) has recently been applied as an innovative signal processing technique in many diverse applications with success. It is a data analysis designed specifically for analyzing nonlinear and non-stationary signal. HHT consists of empirical mode decomposition (EMD) and the Hilbert spectral analysis parts. EMD is the key part of HHT proposed as an adaptive time–frequency analysis method for nonlinear and non-stationary data. EMD use yardstick change of time within signals to resolve signals into the combination of several intrinsic mode functions (IMFs). IMFs contain different characteristics of signals and can express the physical characteristics in signals. Several applications of EMD in biomedical nonlinear and non-stationary signal processing were demonstrated. Nimunkar et al. used EMD for filtering power line noise in electrocardiogram signals [81]. Torres et al. used EMD to analyze respiratory mechanomyographic signals of the diaphragm muscle, acquired by means of a capacitive accelerometer applied on the costal wall [82]. Bennett et al. used EMD to be the bandpass filtering method and produce superior results of tissue harmonic imaging [83]. Zhang et al. used EMD to remove the wall components in Doppler ultrasound signals [84]. However, the major drawback of the EMD is scale (frequency) mixing which consists of signals of widely disparate scales, or a signal of a similar scale residing in different IMF components [85]. Nevertheless, a new EEMD method consists of an ensemble of decompositions of data with added white noise, and then treats the resultant mean as the final true result [86]. The effect of the added white noise is to present a uniform reference frame in the time-frequency (time-scale) space and to provide natural filter windows for the signals of comparable scale to collate in one component, essentially eliminating the scale (frequency) mixing problem in the EMD. The EEMD fully utilizes the statistical characteristics of white noise to perturb the data in its true solution neighborhood, and then cancel itself out

(via ensemble averaging). In this paper, we use a new nonlinear signal analysis method, EEMD, to explore the efficacy of nonlinear ultrasound signal processing. For nonlinear ultrasound imaging, EEMD is an alternative technique for ultrasound contrast imaging and extracts the contrast agent components from the harmonic echoes.

5.1 Empirical Mode Decomposition (EMD)

The starting point of the EMD is to consider signals at the level of their local oscillations. The EMD algorithm extracts the oscillatory mode that exhibits the highest local frequency from the data, leaving the remainder as a “residual”. Ultrasound nonlinear signals were decomposed into IMF by EMD method and the starting point of the EMD is the identification of all the local maxima and minima of the signals. All the local maxima are then connected by a cubic spline curve as the upper envelop. Similarly, all the local minima are connected by a spline curve as the lower envelop. The mean of the two envelopes is denoted and is subtracted from the original signal. The sifting process can be stopped by any of the following predetermined criteria: either when the output signal or the residue becomes so small that it is less than the predetermined value, or when the residue becomes a monotonic function from which no more IMF can be extracted. The name “intrinsic mode function” is adopted because it represents the oscillation mode imbedded in the data. Given a tissue-microbubble mixed ultrasound signal $y(x)$, the IMF are obtained using the EMD algorithm called sifting. Briefly, the sifting process is resumed as follows [87]–[88]:

1. Set $h = y(x)$, where $y(x)$ is the input signal.
2. Find all local maxima and all local minima value of h .
3. Connect all the local maxima to create the upper envelope and similarly for the

lower envelope.

4. Compute the function *Envmean*, which is the mean of the maxima and minima envelopes.

5. Subtract the mean value function from the signal, $h = h - \text{Envmean}$.

6. Repeat the process until the stop criterion is met, so that h is an IMF.

The IMF h is subtracted out from the input signal and the residue which is obtained is used as the new input signal to repeat the sifting process. This procedure is repeated until the difference in the standard deviation of successive estimates of the IMF function falls below a critical threshold. Therefore, a signal $y(x)$ decomposed with the EMD can be expressed as the sum of the c_j and the last residue r_n as

$$y(x) = \sum_{j=1}^n c_j(x) + r_n(x), \quad (\text{Eq. 5-1})$$

Thus, we achieved a decomposition of the data into n -empirical modes, and a residue, r_n , which can be either the mean trend or a constant. The decomposed components $c_j(x)$ contain the nonlinear and oscillation components of the original tissue-microbubble mixed ultrasound signal. The EMD is an adaptive data analysis method that is based on local characteristics of the data, and hence, it catches nonlinear, non-stationary oscillations more effectively. However, when the scales of the tissue and microbubble components were closed, the neighboring components might contain oscillations of the same scale.

5.2 Ensemble Empirical Mode Decomposition (EEMD)

To overcome the scale separation problem in EMD, a noise-assisted data analysis (EEMD) method is proposed. A new EEMD method consists of an ensemble of decompositions of data with added white noise, and then treats the resultant mean as

the final true result [86]. The principle of the EEMD is to add white noise which would populate the whole time-frequency space uniformly with the constituting components of different scales separated by the filter bank [89]–[90]. The EEMD process is resumed as follows:

1. Add a white noise series to the targeted data.
2. Decompose the data with added white noise into IMFs.
3. Repeat step 1 and step 2 again and again, but with different white noise series each time.
4. Obtain the (ensemble) means of corresponding IMFs of the decompositions as the final result.

In this study, when tissue-microbubble mixed signal is added to this uniformly distributed white background, the bits of signal of different scales are automatically projected onto proper scales of reference established by the white noise in the background. The truth defined by EEMD is given by the number in the ensemble approaching infinity, i.e.

$$c_j(x) = \lim_{N \rightarrow \infty} \frac{1}{N} \sum_{k=1}^N \{c_j(x) + \alpha r_k(x)\}, \quad (\text{Eq. 5-2})$$

in which

$$c_j(x) + \alpha r_k(x) \quad (\text{Eq. 5-3})$$

is the k^{th} trial of the j^{th} IMF in the noise-added signal, and the magnitude of the added noise, α , is not necessarily small. But the number of the trials in the ensemble, N , has to be large. In this paper, the added noise α was set by 0.2 and the number of the trials in the ensemble N was set by 200.

5.3 Simulation

The simulation model used to simulate the tissue harmonic signal is obtained from

numerical solutions of the Khokhlov–Zabolotskaya–Kuznetsov (KZK) nonlinear parabolic wave equation [91]. The tissue signals are based on the time-domain solution to KZK equation, which is an approximation of the nonlinear sound field produced by a piston source. The KZK equation can be written in the following form [92]:

$$\frac{\partial^2 P}{\partial \sigma \partial \tau} = \alpha r_0 \frac{\partial^3 P}{\partial \tau^3} + \frac{r_0}{2l_d} \frac{\partial^2 P^2}{\partial \tau^2} + \frac{1}{4} \nabla_{\perp}^2 P, \quad (\text{Eq. 5-4})$$

where $r_0 = w_0 a^2 / 2c_0$, $l_d = \rho_0 c_0^3 / \beta \omega_0 p_0$, $\tau = \omega_0(t - z/c_0)$, $P = p/p_0$; $\nabla_{\perp}^2 = \frac{1}{\xi} \frac{\partial}{\partial \xi} \xi \frac{\partial}{\partial \xi}$;

and a is the radius of the piston. The diameter of piston is assumed 25.4 mm and a focal length is 70 mm. The first, second and third terms on the right-hand side of Eq. (4) correspond to the attenuation, nonlinear distortion and diffraction, respectively. Pressure is normalized in the KZK equation as $P = p/p_0$, where p is actual pressure and p_0 is the pressure on the piston surface. The term $r_0 = w_0 a^2 / 2c_0$ is the Rayleigh distance, and $l_d = \rho_0 c_0^3 / \beta \omega_0 p_0$ is the shock formation distance, where $\beta = 1 + B/2A$ is the nonlinear parameter of the propagation media. The β is 3.5, approximating the nonlinear properties of water [93].

For contrast agents, a bubble-simulation tool (BubbleSim) was used for calculating the echo from a single microbubble (the tool is downloaded from the website of the IEEE UFFC society: <http://www.ieee-uffc.org>). The instantaneous radius of bubble is approximated numerically by solving the Rayleigh-Plesset equation with an arbitrary impinging acoustic wave. Echoes from the bubble can be formulated from the bubble radius, wall velocity, and wall acceleration [94]. In the bubble simulations, the use of sonazoid was assumed. For sonazoid, the shell thickness is 4 nm, the shear modulus of the shell is 50 MPa, and the shell viscosity is 0.8 Pas. To simulate the harmonic signal from contrast agents, the focal waveforms in the KZK simulations were used as

the driving acoustic waveforms in the bubble simulator. Therefore, the bubble-simulation signal is a tissue-microbubble mixed signals. In this study, PI technique was used to obtain the output beam.

For tissue signal, the transmit pulse has a pressure amplitude of 20 kPa at source. The original simulated tissue (left column) and tissue-microbubble mixed (right column) PI signals and shifting of 1–5 IMFs components are shown in Fig. 5-1. The shifting is repeated and stopped at 5 IMFs because the component becomes smaller than a pre-determined value. We can see different characteristics of the signals clearly as the second component (2 IMF) in tissue and tissue-microbubble mixed PI signals. The amplitudes of the simulated tissue and tissue-microbubble mixed PI signals are different in 2 IMF.

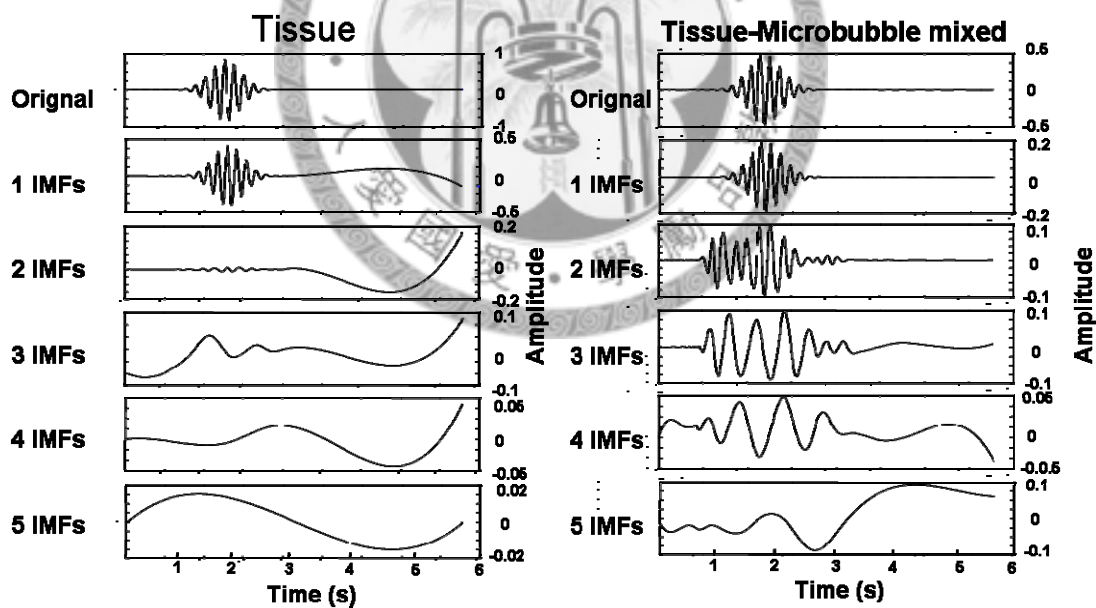


Fig. 5-1. Original tissue harmonic and 1-5 IMFs components of simulated PI signals (left column). Original tissue-microbubble mixed harmonic and 1-5 IMFs components of PI simulated signals (right column).

In Fig. 5-2 (a), spectra of focal waveforms show the simulated PI spectra of tissue (solid line) and tissue-microbubble mixed (dashed line). The simulated PI spectra of tissue (solid line) and tissue-microbubble mixed (dashed line) with 2 IMF are shown in Fig. 5-2 (b). All amplitudes were normalized to the focal fundamental amplitudes in tissue and tissue-microbubble mixed PI signals. In Fig. 5-2 (a), the amplitudes of tissue and tissue-microbubble mixed PI signals are closed either in fundamental band (2.25MHz) or in second band (4.5MHz). Nevertheless, the scales of amplitudes of tissue and tissue-microbubble mixed spectra with IMF2 are large different either in fundamental band (2.25MHz) or in second band (4.5MHz) (Fig. 5-2 (b)).

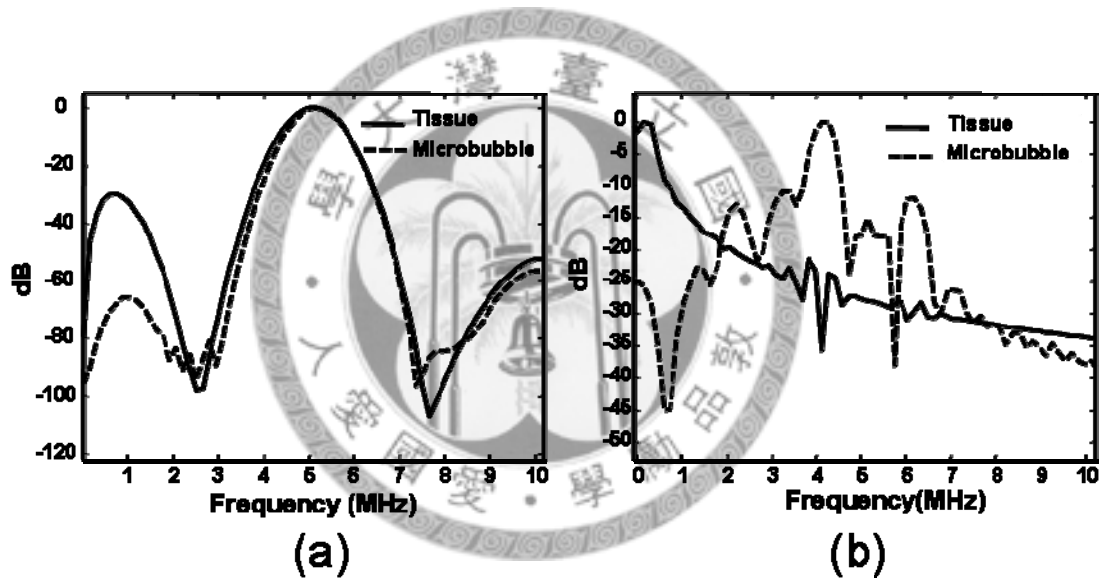


Fig. 5-2. (a) shows the spectra from the original tissue harmonic (solid line) and tissue-microbubble mixed (dashed line) simulated PI signals. (b) shows the spectra from 2 IMFs component. All amplitudes were normalized to the focal fundamental amplitudes in tissue and tissue-microbubble mixed PI signals.

5.4 Experiments

Fig. 5-3 shows the schematic diagram of the experimental setup for measurement of M-mode harmonic signal. The system consists of a single-element transducer used for transmitting Gaussian pulses at 2.5 MHz (Panametrics V304, Waltham, MA, USA), and for receiving fundamental and second harmonic echoes at 2.5 and 5 MHz. The diameter and focal length of both transducers are 25.4 mm and 70 mm, respectively. The transducer was posited by a motor controller. An arbitrary function generator (model 2571, Tabor Electronics, Tel Hanan, Israel) was used to generate the designed transmit pulse. The waveform was then sent to a power amplifier (Amplifier Research 25A250A, Souderton, PA, USA) to drive the transmit transducer. A speckle-generating phantom with uniform distribution of glass beads (Sigma G4649, St. Louis, MO, USA) was used as the tissue background in the image. A tubular void of about 7-mm diameter was fabricated inside the phantom as a microbubble container. The container was imaged by mechanically scanning the transducers. With the short PRI and the relatively slow speed of the motion stage (about 5 mm/s), the change of microbubbles in the sample volume between the two transmit phases can also be neglected for M-mode images. In this study, hydrophone measurements of acoustic field in water were also performed with a PVDF needle hydrophone (Force Technology, MH28-6, Brøndby, Denmark).

In the experiments, Sonovue microbubbles (Bracco Diagnostics, Inc., Milan, Italy) were used. The microbubbles were prepared according to the manufacturer's instructions and were diluted to a volume concentration of 1.5%. The Sonovue microbubbles have a mean diameter of 3 μ m, which correspond to a resonance frequency of about 2.5 MHz. To prolong the life of the encapsulated bubbles, the gain of the power amplifier is kept at a low level. The mechanical index at the focus is limited to below 0.13. The received signals were then sent to an ultrasonic receiver

(Panametrics Model 5072). Finally, an analog-to-digital converter was used to digitize the signal at 14-bit resolution and a sampling rate of 20 Msamples/s (model PCI-9820, Adlink, Taipei, Taiwan). The second harmonic signal was filtered out by low-pass filtering the demodulated echo signal with a 1-MHz cutoff frequency.

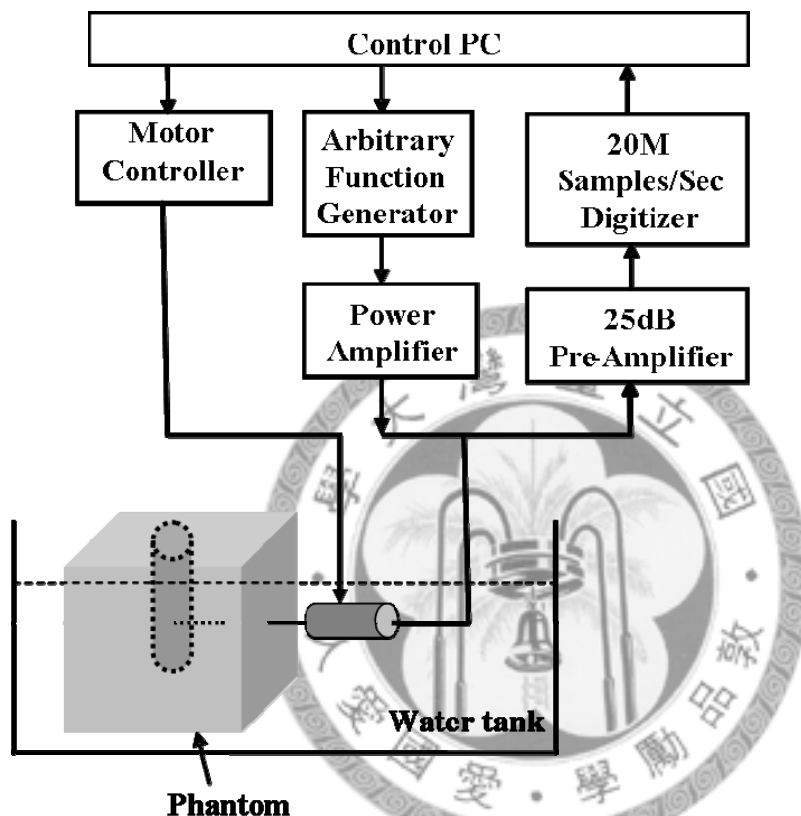


Fig. 5-3. Schematic diagram of the experimental setup for measurement of M-mode harmonic signal.

PI observations can be made using M-mode images. In Fig. 5-4 (a) and (b), M-mode PI images in fundamental and second harmonic mode are shown with a display dynamic range of 40 dB and all 1–5 IMFs were extracted with EMD algorithm. In Fig. 5-4 (a), the CTR of original M-mode PI image in fundamental mode is 17.2 dB and the CTRs of 1–5 IMFs in the same mode are 21.8, 15.6, 7.0, 12.3 and 9 dB. In Fig. 5-4 (b), the CTR of original M-mode PI image in second harmonic mode is 14.9 dB and the CTRs of 1–5 IMFs in the same mode are 15, 7.8,

11.7, 9.5 and 7.1 dB. With EMD, the CTR of 1–5 IMFs in M-mode PI image in fundamental mode increases by 4.6 dB at 1 IMF and the CTR in second harmonic mode only increases by 0.1 dB at 1 IMF. And then, the CTRs decrease at 2–3 IMFs in fundamental mode and decrease proportionally at 3–5 IMFs in second harmonic mode.

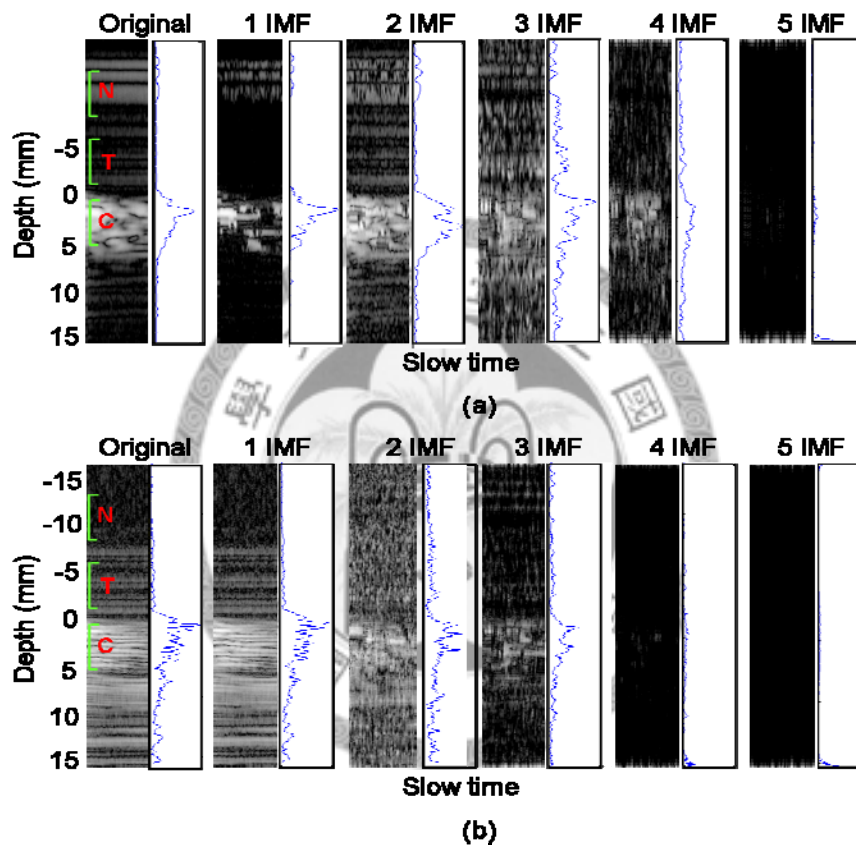


Fig. 5-4. (a) M-mode PI images and axial projections in fundamental mode, all 5 IMFs were extracted with EMD algorithm. (b) M-mode PI images and axial projections in second harmonic mode, all 5 IMFs were also extracted with EMD algorithm.

In Fig. 5-5 (a) and (b), M-mode PI images in fundamental and second harmonic mode are also shown with a display dynamic range of 40 dB and all 1–5 IMFs were extracted with EEMD algorithm. In Fig. 5-5 (a), the CTR of original M-mode PI image in fundamental mode is 17.2 dB and the CTRs of 1–5 IMFs in the same mode

are 22.4, 15.9, 7.3, 19.4 and 9.6 dB. In Fig. 5-5 (b), the CTR of original M-mode PI image in second harmonic mode is 14.9 dB and the CTRs of 1–5 IMFs in the same mode are 15.3, 9.5, 21.4, 14.5 and 8.7 dB. With EEMD, the CTR of 1-5 IMFs in M-mode PI image in fundamental mode increases by 5.2 dB at 1 IMF and the CTR in second harmonic mode increases by 6.5 dB at 3 IMF. And then, the CTRs decrease at 2–3 IMFs in fundamental mode and decrease at 4–5 IMFs in second harmonic mode.

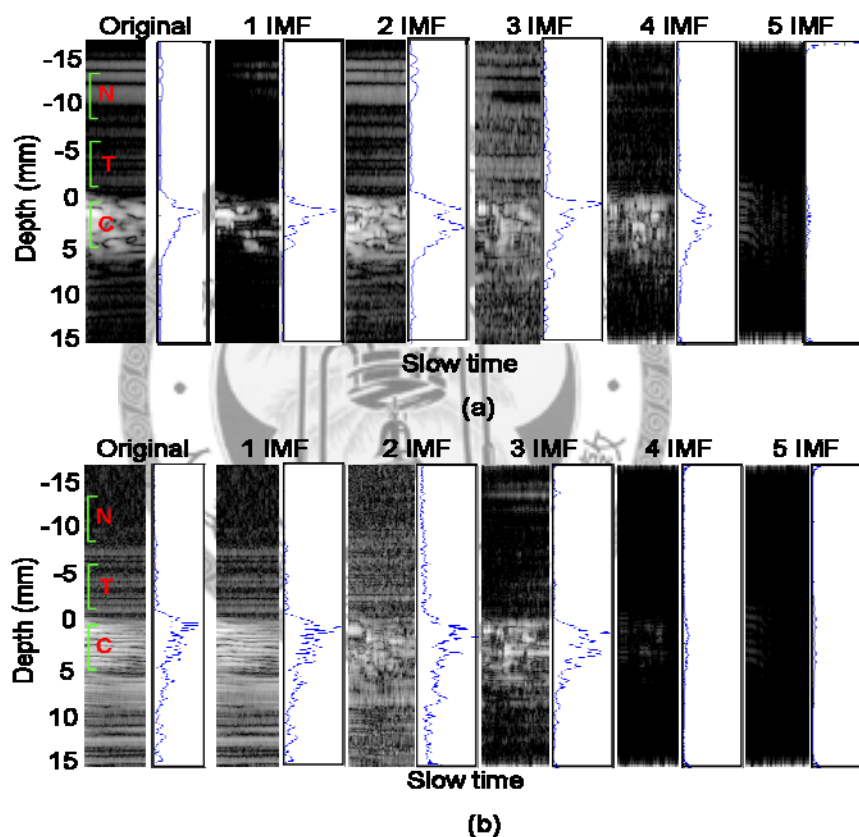


Fig. 5-5. (a) M-mode PI images and axial projections in fundamental mode, all 5 IMFs were extracted with de-noising EEMD algorithm. (b) M-mode PI images and axial projections in second harmonic mode, all 5 IMFs were also extracted with de-noising EEMD algorithm.

Fig. 5-6 (a) shows the comparison of CTR values in experimental results by PI fundamental (1 IMF), PI second harmonic (1 IMF) groups with EMD algorithm. With EMD, the CTR was improved obviously in fundamental but was not improved in

second harmonic mode. The comparison of CTR values in experimental results by PI fundamental (1 IMF), PI second harmonic (3 IMF) groups with EEMD algorithm is shown in Fig. 5-6 (b). With EEMD, the CTRs were improved obviously either in PI fundamental or PI second harmonic groups.

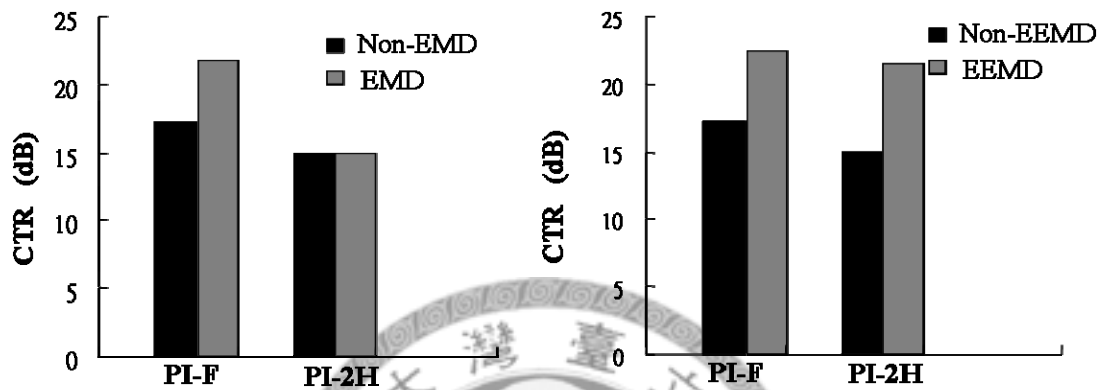


Fig. 5-6. (a) Comparison of CTR values in M-mode PI images by PI fundamental (1 IMF) and PI second harmonic (1 IMF) and groups with EMD algorithm. (b) Comparison of CTR values in M-mode PI images by PI fundamental (1 IMF) and PI second harmonic (3 IMF) and groups with EEMD algorithm.

5.5 Denoising

Fig. 5-7 (a) shows CTR and contrast-to-noise ratio (CNR) improvements in 1-5 IMFs PI fundamental mode images with EMD. With EMD, the CTR was improved only in 1 IMF but the CNR was improved in 1 IMF and 3 IMF. In 1 IMF and 3 IMF, the CNR was only improved by 1.7 and 0.8 dB. Nevertheless, with EEMD, the CNR was improved by 9, 6.2 and 1.7 dB in 1 IMF, 4 IMF and 5 IMF with EEMD in Fig. 5-7 (b). Fig. 5-7 (b) shows CTR and CNR improvements in 1-5 IMFs PI fundamental mode images. The CTR was improved obviously in 1 IMF and 4 IMF with EEMD. With EMD, in PI second harmonic mode images, the CTR and CNR were only improved by 0.1 and 0.25 dB in IMF1 (Fig. 5-8 (a)). In Fig. 5-8 (a), the CTR and CNR decreased proportionally in 3-5 IMFs. With EEMD, Fig. 5-8 (b) shows the CTR

and CNR improvements in 1-5 IMFs PI second harmonic mode images with EEMD. The CTR was improved by 0.4 dB in 1 IMF and 6.5 dB in 3 IMF. The CNR was improved by 0.5 dB only in 1 IMF. The CNR was improved obviously in PI fundamental groups with EEMD. The effectiveness of CTR and CNR improvements with denoising EEMD was observed in Fig. 5-7 and Fig. 5-8.

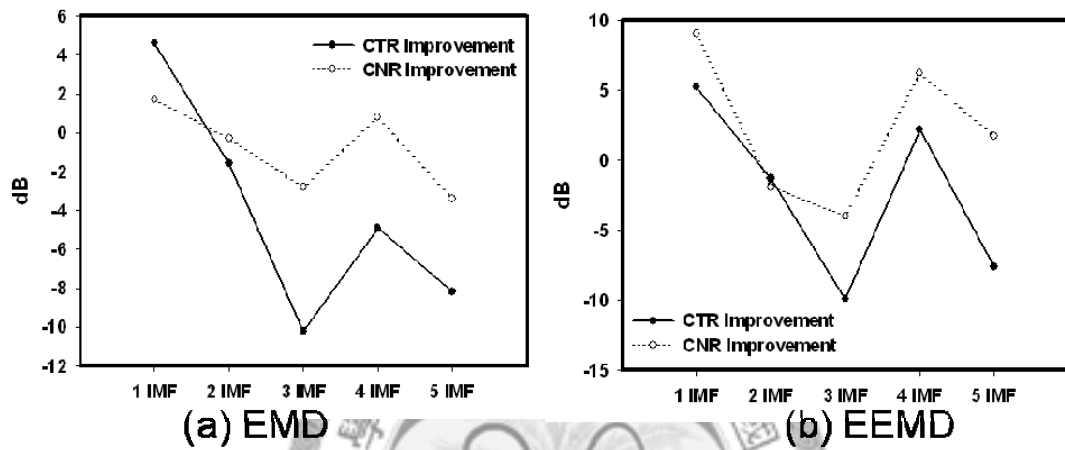


Fig. 5-7. (a) Comparison of CTR and CNR improvement values in PI M-mode images in fundamental mode with EMD algorithm. 1-5 IMFs were extracted with EMD algorithm. (b) Comparison of CTR and CNR improvement values in PI M-mode images in fundamental mode with EEMD algorithm. 1-5 IMFs were extracted with EEMD algorithm.

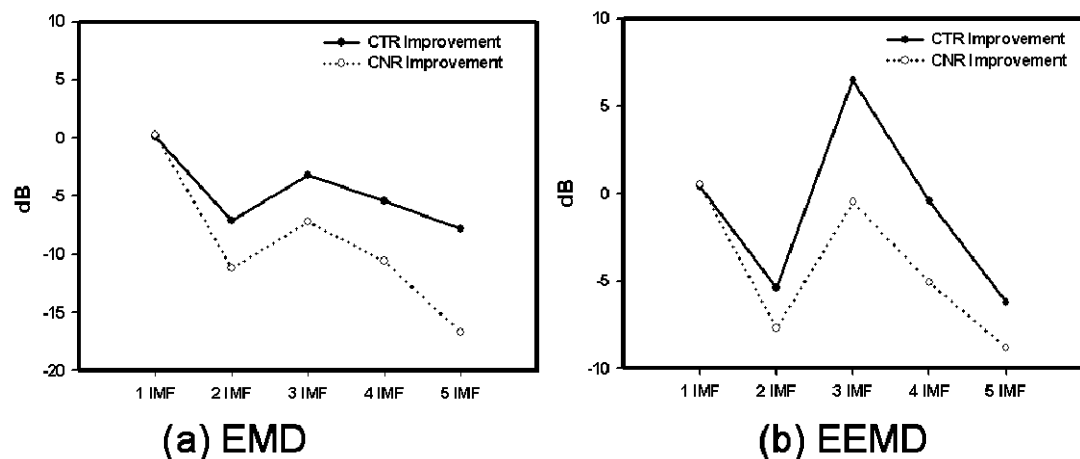


Fig. 5-8. (a) Comparison of CTR and CNR improvement values in PI M-mode images in second harmonic mode with EMD algorithm. 1-5 IMFs were extracted with EMD algorithm. (b) Comparison of CTR and CNR improvement values in PI M-mode images in second harmonic mode with EEMD algorithm. 1-5 IMFs were extracted

with EEMD algorithm.

5.6 Discussions

In this study, PI technique was used to obtain the output beam. With EMD, in conventional output beam (positive wave), original tissue harmonic, tissue-microbubble mixed harmonic and 1-5 IMFs components of simulated signals are shown in Fig. 5-9. The shifting components seem not recovered to the original waveform and the amplitude of original tissue harmonic signal was not suppressed in 1-5 IMFs components. With EEMD, in Fig. 5-10, tissue harmonic signal was recovered to the original waveform in 2 IMF and the waveforms were convergence in 5 IMFs either in tissue harmonic signal or in tissue-microbubble mixed harmonic signal.

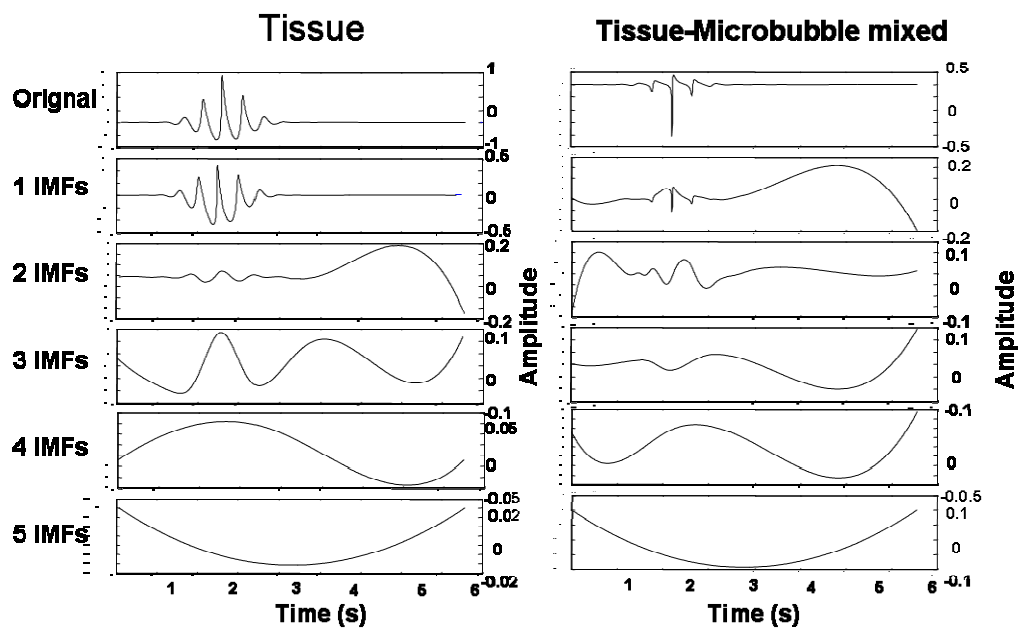


Fig. 5-9. With EMD, original tissue harmonic and 1-5 IMFs components of conventional simulated signals are shown in left column. Original tissue-microbubble mixed harmonic and 1-5 IMFs components of conventional simulated signals are shown in right column.

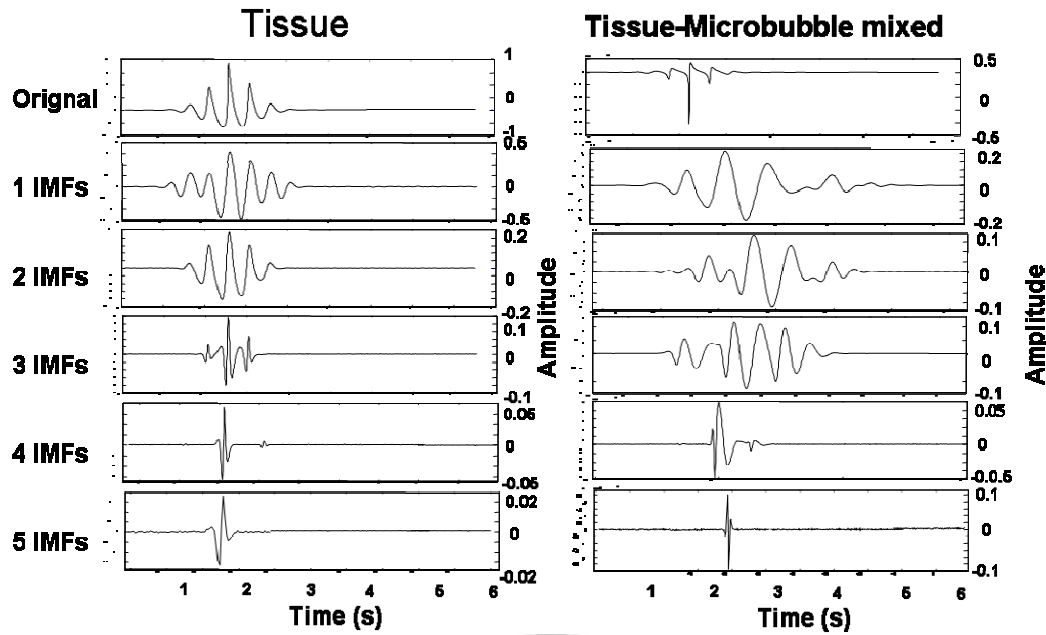


Fig. 5-10. With EEMD, original tissue harmonic and 1-5 IMFs components of conventional simulated signals are shown in left column. Original tissue-microbubble mixed harmonic and 1-5 IMFs components of conventional simulated signals are shown in right column.

After adding uniform noise in conventional simulated signal (Fig. 5-11 and Fig. 5-12), the shifting is repeated and stopped at 10 IMFs because the 11 IMF component becomes smaller than a pre-determined value. With EMD, the tissue-microbubble mixed harmonic signal was recovered to the original waveform in 4 IMF (Fig. 5-11). With EEMD, the tissue harmonic and tissue-microbubble mixed harmonic signals were both recovered to the original waveform in 4 IMF (Fig. 5-12). However, the amplitude of the tissue harmonic signal was still not suppressed and the features in the various components of tissue harmonic signal and tissue-microbubble mixed harmonic signal were not different. It seems the PI technique can suppress the component of tissue harmonic signal firstly.

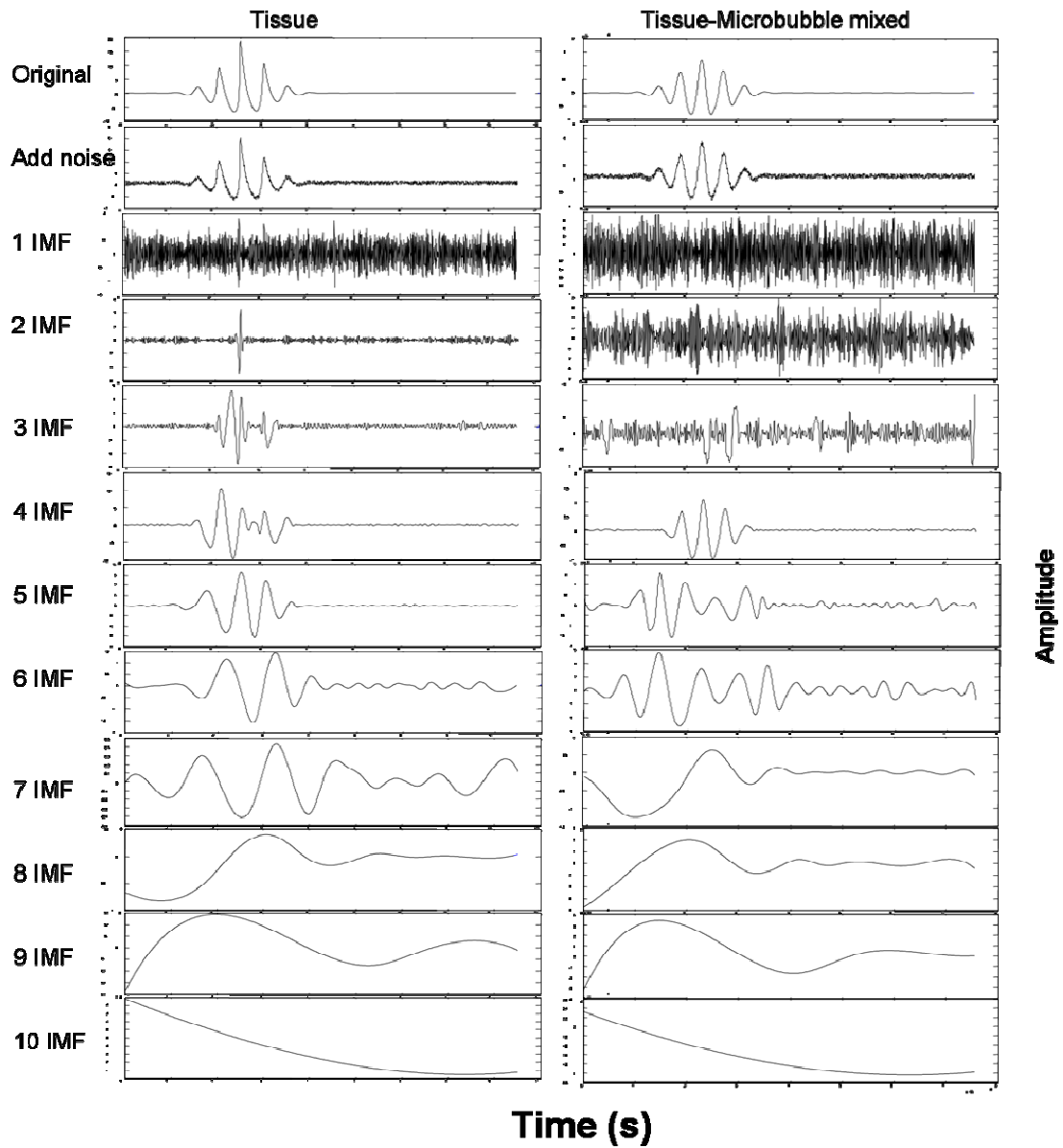


Fig. 5-11. With EMD, original tissue harmonic and 1-10 IMFs components of conventional simulated signals added uniform noise are shown in left column. Original tissue-microbubble mixed harmonic and 1-10 IMFs components of conventional simulated signals added uniform noise are shown in right column.

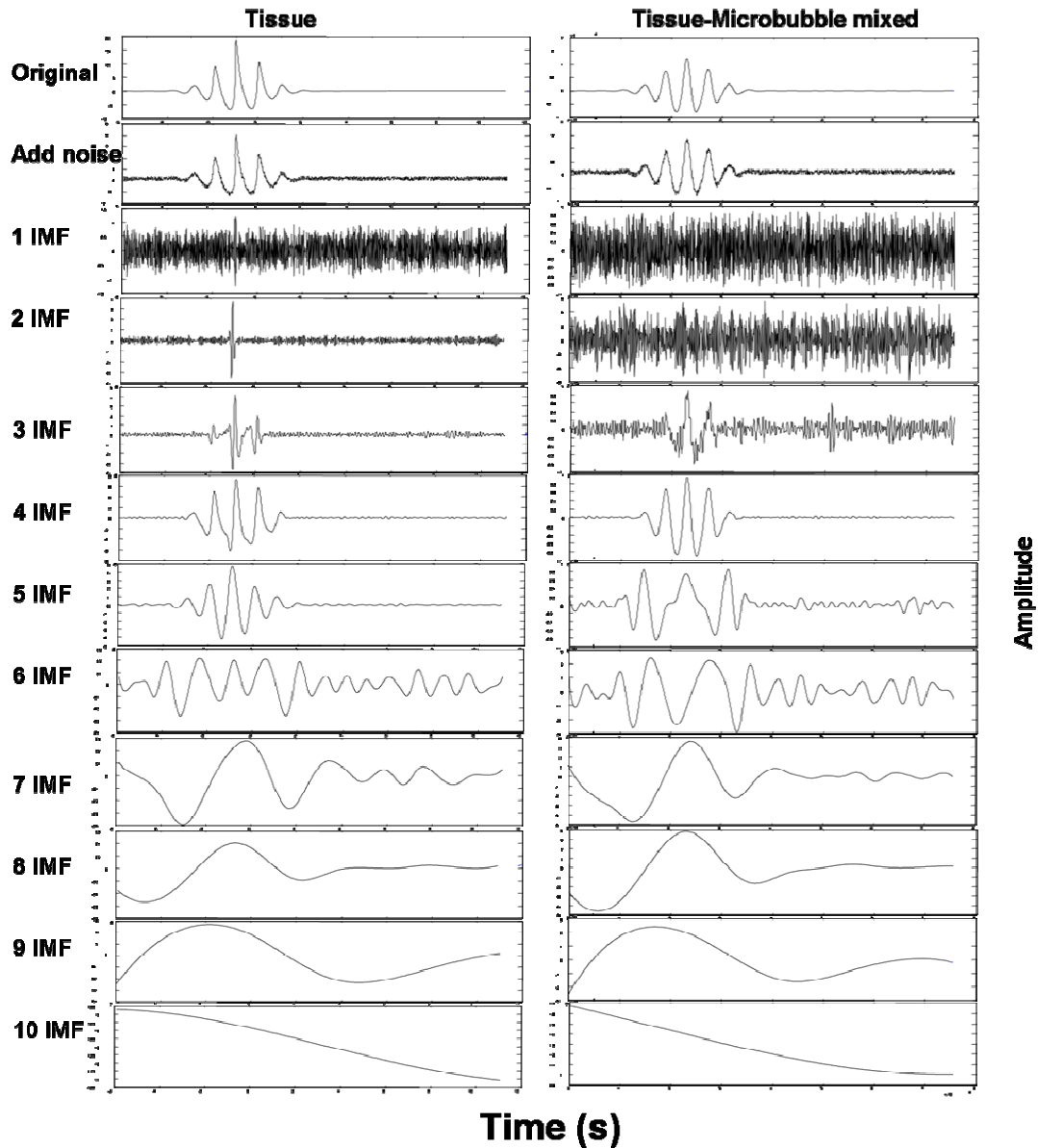


Fig. 5-12. With EEMD, original tissue harmonic and 1-10 IMFs components of conventional simulated signals added uniform noise are shown in left column. Original tissue-microbubble mixed harmonic and 1-10 IMFs components of conventional simulated signals added uniform noise are shown in right column.

Therefore, we investigated the performance of PI fundamental and second harmonic images with EMD and EEMD algorithms. We have evaluated the performance of separating the simulated tissue and tissue-microbubble mixed signals using EMD. The EMD picks out the oscillation amplitude in tissue-microbubble mixed signal in IMF 2. Thus, the determination of the number of the IMFs with the

maximum oscillation amplitudes differ from each other can be used for the separation of the tissue and the tissue-microbubble mixed signal components. Fig. 5-2 (b) gives the IMF 2 spectrograms of the tissue-microbubble mixed signals separated from the tissue signal with 8 and 20 dB in fundamental and second harmonic band by using the EMD method. Thus, the experimental tissue and tissue-microbubble mixed PI signals can be separated by EMD and reconstructed for the M mode image.

In the ideal case, the PI fundamental signal for tissue would be zero, but in practice, this is limited by the measurement noise [94]. This paper has demonstrated that the EMD method has a large effect on the performance of PI fundamental imaging. The results show that the CTR of microbubble and tissue is markedly different between the results with IMF decomposing and the results without IMF decomposing. However, the background noise increases through IMF decomposing. Because the major drawback of the EMD is mode mixing which consists of signals of widely disparate scales, or a signal of a similar scale residing in different IMF components [85], the EMD method has no effect on the performance of PI second harmonic imaging. For the experimental results in PI second harmonic image, Fig. 5-6 (a) and Fig. 5-8(a) show that the CTRs of microbubble and tissue with EMD in most groups are lower than non-EMD groups.

However, denoising EEMD represents a major improvement of the EMD method. In Fig. 5-6 (b), the CTRs were improved obviously either in PI fundamental and second harmonic mode images with EEMD. Although the improvement is not obvious in fundamental mode between EMD and EEMD, the CNR improvement is obvious shown in Fig. 5-7 (b). In Fig. 5-7, the trend of the CNR does not correspond to CTR in 1–5 IMFs in fundamental mode image. Nevertheless, in Fig. 5-8, the trend of the CNR corresponds to CTR in 1–5 IMFs in second harmonic mode image. It seems that the CNR improvement is related to the CTR improvement in second harmonic mode

image.

The results show that EEMD appears to provide effective enhancement in microbubble signals either in fundamental mode or in second harmonic mode. CNR improvement is obvious in second harmonic mode. However, the image features are different in different IMFs components. Although the CTR in M-mode PI image in fundamental mode increases by 5.2 dB at 1 IMF and the CTR in second harmonic mode increases by 6.5 dB at 3 IMF, the image features of contrast agent areas (fragmentary) in these components are different from the original images. Recently, EMD technique has been extended to analyze two dimensional data/images, which is known as bidimensional EMD (BEMD), image EMD (IEMD), 2D EMD etc. Both EMD and BEMD require finding local maxima and local minima points (jointly known as local extrema points) and subsequent interpolation of those points in each iteration of the process. In clinical images, a new analysis method of texture images based on BEMD was firstly presented in Ref. [95]. A BEMD method was used to reduce speckle noise in digital speckle pattern interferometry fringes [96]. The proposed denoising BEMD approach has higher performance and also runs much faster than the 1D EMD. Further work for contrast improvement in this area could be investigated.

CH 6. CONCLUSIONS AND FUTURE WORKS

6.1 MicroUS/MicroPET Multimodality Small Animal Imaging

We have developed an effective method for the 3D registration of combined microUS and microPET imaging. The distinct differences between the natures of these two imaging methods makes it necessary to utilize external markers. In addition, rigid-body transformation is employed to ensure adequate performance. FRE can be used to quantify the effectiveness of the method, and we constructed test phantoms with a known image target so that TRE values could also be determined. Such methods could also be applied for the registration of other small-animal imaging modalities.

The primary application of the proposed method is in cancer research on small-animal models. In such applications microUS provides excellent anatomical information, whereas microPET provides information on glucose metabolism. Future studies could add CEUS imaging to evaluate the vascular phase. Since cancer drugs are delivered to the tumors via the vessels, such a multimodality approach represents an effective tool for both drug development and cancer research.

In conclusion, microUS and microPET imaging techniques were applied for evaluating the tumor growth and progression. The results suggest that microUS is more reliable than microPET and traditional calipers in tumor volume analysis, especially when tumor volume is small. On the other hand, tumor hypoxia and necrosis can be detected by microPET when the tumor is at late stages. The anatomical information obtained from microUS complements with the metabolism information from microPET imaging, and the combination can be a valuable tool in

cancer research. Image registration and fusion methods are being developed as the next step in realizing potential of microUS/microPET multimodality imaging.

6.2 Feasibility of Using Contrast-Enhanced 40 MHz Ultrasound Imaging to Characterize Hepatocellular Carcinomas in Small Animal

Contrast harmonic ultrasound imaging has been widely applied at lower frequencies, but at 15 MHz this did not improve the identification of HCC lesions in a transgenic mice model [66]. One possible reason is that the hypervascularity is less important in the HCC mouse model than in humans. Another possible explanation is that the frequencies used in previous studies were too low to provide adequate spatial resolution – Mai et al. (2004) used Sonovue microbubbles, which have a mean diameter of about 2.5 μm , whereas our microbubbles had a mean diameter of about 1.2 μm and hence are better suited to higher frequency applications [67].

The results from the present study suggest that contrast-enhanced 40 MHz ultrasound imaging enhances the ability to detect three vascular phases and characterize malignant focal lesions, at least in mouse models, and would provide more information during experimental HCC treatments in small animal models. Moreover, we also have experimentally evaluated EMD method for contrast improvement in nonlinear imaging. This method is based on EMD and EEMD by extracting microbubble component and suppressing background noise. The presented simulated and experimental results demonstrate that the contrast enhancement was noticeably improved either in fundamental mode or second harmonic mode images investigated using EEMD.

6.3 Future Works

6.3.1 Applications of the Three-Dimensional Registration Method for MicroUS/MicroPET Multimodality Small Animal Imaging

In the future, the three-dimensional registration method for microUS/microPET multimodality imaging would be performed for non-invasive tumor volume analysis on a weekly basis. After microUS and [^{18}F]FDG microPET imaging have been performed by the registration method, the WF-3 ovarian carcinoma implanted subcutaneously in the right shoulder of the mouse would be removed. We will measure the lengths of the three dimensions of the tumor and the tumor volume was calculated. For this work, the removed tumor parenchyma volume can be the gold standard for comparing the results of registration imaging. The growth curve can be measured by the three-dimensional registration method.

Moreover, the construction of the registration marker can be improved. A new, multimodality registration marker will be produced. The glass bead containing positron isotope with a diameter of 0.43–0.60 mm is more suitable for the three-dimensional rigid body registration method.

6.3.2 Microbubbles for Therapeutic Application in Hepatocellular Carcinomas

In preclinical research, new strategies to detect tumor angiogenesis and monitor response of tumor vasculature to therapy are needed. In my recent research, high-frequency (40 MHz) CEUS imaging was applied to small animals. We sought to investigate whether the new anticancer drugs or the microbubble destruction

technique during arterial phase are able to produce tumor vascular changes in a mouse model of hepatocellular carcinoma.

HCC is a primary liver malignancy in humans that most often occurs in association with cirrhosis or chronic hepatitis. Despite alcohol injection, chemoembolization, or thermal ablation local recurrences are the rule and life expectancy is short. Because HCC is a typical chemotherapy-resistant hypervascular tumor, inhibition of angiogenesis could offer therapeutically important advantages [97].

Evaluation of the response to treatment is usually accomplished basing on clinics, laboratory tests and volume reduction of the tumor; however, the antiangiogenic activity can be assessed directly evaluating whether changes in tumor microvessels occur during the treatment. Very slow flows in the microvessels cannot be studied with Doppler techniques, but can now be evaluated non-invasively using CEUS. In CEUS, the intensity enhancement in the vessels within a suspected HCC lesion during the arterial phase is very useful for the detection of HCC angiogenesis.

Recently, there have been numerous reports on application of ultrasound energy for targeting or controlling drug release. This new concept of therapeutic ultrasound combined with drugs has induced excitement in various medical fields [98]. Destruction of microbubbles by ultrasound resulting in increased membrane permeability by shear stress, temperature rise and activation of reactive oxygen species. In Fig. 6-1, drug delivery mechanism was identified as the transient holes induced by microbubbles, increase in membrane permeability, endocytosis of microbubbles and fusion of the microbubbles membrane with cell membrane. Albumin microbubbles were first used to further enhance the effects of thrombolytic agents in conjunction with ultrasound [99].

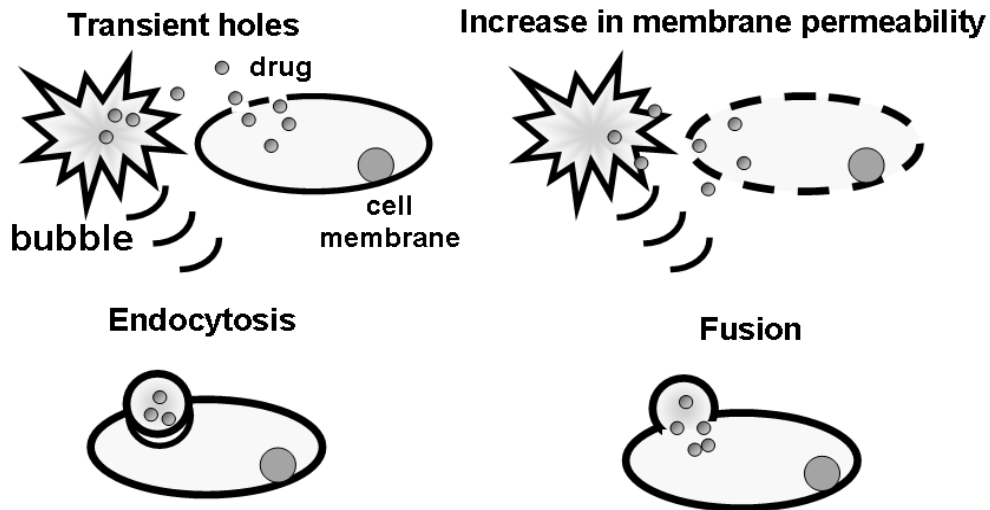


Fig. 6-1. Destruction of microbubbles by ultrasound.

When bubbles are destroyed by ultrasound while within the vessel, the variation of their diameters may be sufficient to rupture capillaries, and the pharmaceutical agent can exit the bloodstream and enter the tissue (Fig. 6-2). In this study, the time intensity curves were acquired for 30 minutes by 40 MHz high frequency ultrasound system after albumin microbubbles injection for identifying and characterizing the various phases of HCC in HBx transgenic mice. CEUS and Color Doppler imaging were performed in the arterial phase before and during anticancer drugs treatment. Besides, the microbubbles were destruction by 1 MHz ultrasound system during the arterial phase. The vascularity index was measured to evaluate the blood flow changes in HCC lesion. The damage after destruction the microbubbles during the arterial phase can be estimated. The effectiveness of the anticancer therapy in HCC can also be observed in the preclinical system.

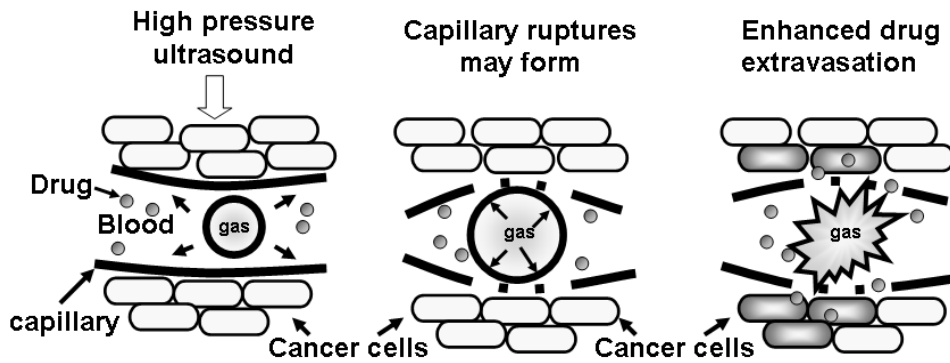


Fig. 6-2. Capillary rupture by microbubble expansion in the ultrasound field.

6.3.2.1 Production of Anticancer Microbubbles

Briefly, perfluorocarbon-exposed sonicated dextrose albumin microbubbles containing anticancer drugs were generated using a solution of 5% bovine serum albumin (Calbiochem, San Diego, CA), 5% dextrose (Sigma, St. Louis, MO) in PBS, and 1% anticancer drugs (Sorafenib, Sutent or PI-88) (Fig. 6-3). The solution of dextrose, bovine serum albumin, and anticancer drugs was mixed in the presence of perfluoropropane gas (C_3F_8) and sonicated at 20 kHz using an ultrasonic processor. The microbubbles were injected through the lateral tail vein and destructed during arterial phase.

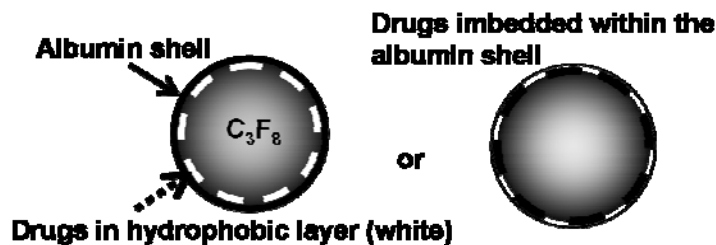


Fig. 6-3 Conception of anticancer-drug enclosed by microbubble.

6.3.2.2 Potential of Multimodality Microbubbles

The combining methods of microUS and microPET multimodality imaging systems could be extended and other imaging systems integrate into these new techniques. For example, the homemade microbubbles could be constructed a multimodality contrast agent. The homemade ultrasound contrast agent used in this study comprised microbubbles with albumin shells, and is similar to the commercial ultrasound contrast media Optison™ [60]–[61]. The homemade albumin-based microbubbles were produced by sonication of 10-mL solution containing 0.9% sodium chloride, 6.6% human serum albumin (Octopharma AG, Switzerland) and perfluorocarbon (C₃F₈) gas. The number of microbubbles in each solution was measured with MultiSizer III (Beckman Coulter) with 30 μm aperture probe, whose measurement boundary is between 0.6 to 20 μm. The concentration of the microbubbles ranges 4.24–8.43x10⁸/ml. The mean diameter number size is 0.7–2.0 μm. A multiplicity of ligands may be coupled to microbubbles directly via covalent bonds or indirectly through avidin-biotin interactions. Ultrasonically reflective particles can be complexed to paramagnetics for MR or radionuclide for nuclear or D-luciferin for bioluminescent or fluorescence for microscope multimodal imaging.

6.3.3 Evaluation Blood Flow Changes with Contrast Enhanced 40 MHz Ultrasound in HBx Transgenic Mice

High-frequency ultrasound B-mode and color Doppler imaging was applied to the entire livers of HBx mice. After identifying suspected HCC lesions, microbubbles were injected through the lateral tail vein, and post-contrast-injection imaging of the suspected HCC lesions was immediately performed for 30 minutes. Regions of interest (ROIs) were selected in the suspected HCC lesions. The vascularity index (VI₂) was calculated in each ROI according to the function $VI = \frac{\text{the number of the color pixels}}{\text{the number of the ROI pixels}}$. Image intensity in B-mode images was

also calculated. Besides, mean video intensity (VI) from averaged contrast-enhanced images was subtracted from that of the corresponding averaged precontrast images.



REFERENCES

- [1] <http://www.cancer.org>, American Cancer Society Global Cancer Facts & Figures, 2007.
- [2] K. Glunde, A. P. Pathak and Z. M. Bhujwala, “Molecular-functional imaging of cancer: to image and imagine,” *Trends Mol Med.*, vol. 13, no. 7, pp. 287–97, July 2007.
- [3] D. R. Aberle, C. Chiles, C. Gatsonis, B. J. Hillman, C. D. Johnson, B. L. McClennan, D. G. Mitchell, E. D. Pisano, M. D. Schnall, A. G. Sorensen and American College of Radiology Imaging Network, “Imaging and cancer: research strategy of the American College of Radiology Imaging Network,” *Radiology*. vol. 235, no. 3, pp. 741–51, June 2005.
- [4] R. G. Blasberg and J. G. Tjuvajev, “Molecular-genetic imaging: current and future perspectives,” *J. Clin. Invest.* vol. 111, pp. 1620–1629, 2003.
- [5] R. Weissleder and U. Mahmood, “Molecular imaging,” *Radiology*. vol. 219, pp. 316–333, 2001.
- [6] M.-L. Jan, K.-S. Chuang, G.-W. Chen, Y.-C. Ni, S. Chen, C.-H. Chang, J. Wu, T.-W. Lee and Y.-K. Fu, “A three-dimensional registration method for automated fusion of micro PET-CT-SPECT whole-body images,” *IEEE Trans. Med. Imaging*. vol. 24, pp. 886–893, 2005.
- [7] D. Townsend, T. Beyer and T. Blodgett, “PET/CT scanners: a hardware approach to image fusion,” *Semin. Nucl. Med.* vol. 3, pp. 193–204, 2003.
- [8] C. A. Piron, P. Causer, R. Jong, R. Shumak and D. B. Plewes, “A hybrid breast biopsy system combining ultrasound and MRI,” *IEEE Trans. Med. Imaging*. vol. 22, pp. 1100–1110, 2003.
- [9] F. S. Foster, C. J. Pavlin, K. A. Harasiewicz, D. A. Christopher and D. H. Turnbull,

- “Advances in ultrasound biomicroscopy,” *Ultrasound Med. Biol.* vol. 26, pp. 1–27, 2000.
- [10] D. A. Knapik, B. Starkoski, C. J. Pavlin and F. S. Foster, “A 100–200 MHz ultrasound biomicroscope,” *IEEE Trans. Ultrason. Ferroelectr. Freq. Control.* vol. 47, pp. 1540–1549, 2000.
- [11] D. E. Goertz, J. L. Yu, R. S. Kerbel, P. N. Burns and F. S. Foster, “High-frequency 3-D color-flow imaging of the microcirculation,” *Ultrasound Med. Biol.* vol. 29, pp. 39–51, 2003.
- [12] M.-L. Li, Y.-F. Chen, W.-J. Guan and P.-C. Li, “A digital ultrasonic system for small animal imaging,” *Ultrason. Imag.* vol. 26, pp. 85–99, 2004.
- [13] Y.-C. Tai, A. Chatziioannou, S. Siegel, J. Young, D. Newport, R. N. Goble, R. E. Nutt and S. R. Cherry, “Performance evaluation of the microPET P4: a PET system dedicated to animal imaging,” *Phys. Med. Biol.* vol. 46, pp. 1845–1862, 2001.
- [14] A. K. Singh, E. G. Moros, P. Novak, W. Straube, A. Zeug, J. E. Locke and R. J. Myerson, “MicroPET-compatible, small animal hyperthermia ultrasound system (SAHUS) for sustainable, collimated and controlled hyperthermia of subcutaneously implanted tumours,” *Int. J. Hyperthermia* vol. 20, pp. 32–44, 2004.
- [15] M. A. Audette, F. P. Ferrie and T. M. Peters, “An algorithmic overview of surface registration techniques for medical imaging,” *Med. Image Anal.* vol. 4, pp. 201–217, 2001.
- [16] J. V. Hajnal, D. L. G. Hill and D. J. Hawkes, “Medical image registration,” Boca Raton, FL: CRC Press, 2001.
- [17] J. P. W. Pluim, J. B. A. Maintz and M. A. Viergever, “Mutual-information-based

- registration of medical images: a survey,” *IEEE Trans. Med. Imaging*. vol. 22, pp. 986–1004, 2003.
- [18] F. Maes, F. Collignon, D. Vandermeulen, G. Marchal and P. Suetens, “Multimodality image registration by maximization of mutual information,” *IEEE Trans. Med. Imaging*. vol. 16, pp. 187–198, 1997.
- [19] R. C. Gonzalez and R. E. Woods, “Digital image processing,” 2nd edn., Upper Saddle River, NJ: Prentice Hall, 2002.
- [20] J. Ashburner and K. J. Friston, “Rigid body registration,” London, UK: The Wellcome Dept. of Imaging Neuroscience, Chap. 2, 2001.
- [21] L. Solbiati, A. Martegani, E. Leen, J. M. Correas, P. N. Burns and D. Becker, “Contrast-enhanced ultrasound of liver diseases,” Springer, Milan, Italy, 2003.
- [22] L. Bolondi, J. M. Correas, R. Lencioni, H. P. Weskott and F. Piscaglia, “New perspectives for the use of contrast-enhanced liver ultrasound in clinical practice,” *Dig. Liver Dis.* vol. 39, no. 2, pp. 187–195, 2007.
- [23] O. Matsui, M. Kadoya, T. Kameyama, J. Yoshikawa, T. Takashima, Y. Nakanuma, M. Unoura, K. Kobayashi, R. Izumi, M. Ida and K. Kitagawa, “Benign and malignant nodules in cirrhotic livers: distinction based on blood supply,” *Radiology*. vol. 178, pp. 493–497, 1991.
- [24] S. C. Efremidis and P. Hytiroglou, “The multistep process of hepatocarcinogenesis in cirrhosis with imaging correlation,” *Eur Radiol.* Vol. 12, pp. 753–764, 2002.
- [25] M. Kojiro and O. Nakashima, “Histopathologic evaluation of hepatocellular carcinoma with special reference to small early stage tumors,” *Semin Liver Dis.* vol. 19, pp. 287–296, 1999.
- [26] A. Giorgio, G. Ferraioli, L. Tarantino, G. de Stefano, V. Scala, F. Scarano, C.

- Coppola and L. Del Viscovo, "Contrast-enhanced sonographic appearance of hepatocellular carcinoma in patients with cirrhosis: comparison with contrast-enhanced helical CT appearance," *AJR Am J Roentgenol.* vol. 183, pp.1319–1326, 2004.
- [27] H.-J. Jang, T. K. Kim and S. R. Wilson, "Imaging of malignant liver masses: characterization and detection," *Ultrasound Q.* vol. 22, pp.19–29, 2006.
- [28] C. R. Meyer, B. A. Moffat, K. K. Kuszpit, P. L. Bland, P. E. Mckeever, T. D. Johnson, T. L. Chenevert, A. Rehemtulla and B. D. Ross, "A methodology for registration of a histological slide and in vivo MRI volume based on optimizing mutual information," *Mol. Imaging.* vol. 5, pp. 16–23, 2006.
- [29] I. Daftari, D. Barash, S. Lin and J. O'Brien, "Use of high-frequency ultrasound imaging to improve delineation of anterior uveal melanoma for proton irradiation," *Phys. Med. Biol.* vol. 46, pp. 579–590, 2001.
- [30] C.-X. Deng, F. L. Lizzi, R. H. Silverman, R. Ursea and D. J. Coleman, "Imaging and spectrum analysis of contrast agents in the in vivo rabbit eye using very-high-frequency ultrasound," *Ultrasound Med. Biol.* vol. 24, pp. 383–394, 1998.
- [31] C. Guittet, F. Ossant, J. P. Remenieras, L. Pourcelot and M. Berson, "High-frequency estimation of the ultrasonic attenuation coefficient slope obtained in human skin: simulation and in vivo results," *Ultrasound Med. Biol.* vol. 25, pp. 421–429, 1999.
- [32] S. Umeyama, "Least-squares estimation of transformation parameters between two point patterns," *IEEE Trans. Pattern Anal. Mach. Intell.* vol. 13, pp. 376–380, 1991.
- [33] C.-A. Chen, W.-F. Cheng, T.-C. Wu and C.-Y. Hsieh, "Generation of ovarian

- cancer animal model,” In: *Proceedings of the Ninth Biennial Meeting of the International Gynecologic Cancer Society*, pp. 526–527, 2002.
- [34] S. P. Mok, C.-H. Wang, J.-C. Chen and R.-S. Liu, “Performance evaluation of the high resolution small animal PET scanner,” *Biomed. Eng. Appl. Basis Comm.* vol. 15, pp. 143–149, 2003.
- [35] T. Frese, N. C. Rouze, C. A. Bouman, K. Sauer and G. D. Hutchins, “Quantitative comparison of FBP, EM, and Bayesian reconstruction algorithms for the IndyPET scanner,” *IEEE Trans. Med. Imaging.* vol. 22, pp. 258–276, 2003.
- [36] J. R. Hurley and R. B. Cattell, “The procrustes program: producing direct rotation to test a hypothesized factor structure,” *Behav. Sci.* vol. 7, pp. 258–262, 1962.
- [37] P. H. Schonemann, “A generalized solution of the orthogonal procrustes problem,” *Psychometrika.* vol. 31, pp. 1–10, 1966.
- [38] F. J. M. itzpatrick, J. B. West and C. R. Maurer, “Predicting error in rigid-body point-based registration,” *IEEE Trans. Med. Imaging.* vol. 17, pp. 694–702, 1998.
- [39] T. Taxt, “Restoration of medical ultrasound images using two-dimensional homomorphic deconvolution,” *IEEE Trans. Ultrason. Ferroelectr. Freq. Control.* vol. 42, pp. 543–554, 1995.
- [40] A. M. Cheung, A. S. Brown, L. A. Hastie, V. Cucevic, M. Roy, J. C. Lacefield, A. Fenster and F. S. Foster, “Three-dimensional ultrasound biomicroscopy for xenograft growth analysis,” *Ultrasound Med Biol.* vol. 31, pp. 865–870, 2005.
- [41] A.-H. Liao, L.-Y. Chen, W.-F. Cheng and P.-C. Li, “A three-dimensional registration method for microUS/ microPET multimodality small-animal imaging,” *Ultrason Imag.* vol. 29, pp. 155–166, 2007.
- [42] C. M. Deroose, A. De, A. M. Loening, P. L. Chow, P. Ray, A. F. Chatziioannou and S. S. Gambhir, “Multimodality imaging of tumor xenografts and metastases in

- mice with combined small-animal PET, small-animal CT, and bioluminescence imaging,” *J Nucl Med*. Vol. 48, pp. 295–303, 2007.
- [43] D. E. Jenkins, Y. Oei, Y. S. Hornig, S. F. Yu, J. Dusich, T. Purchio and P. R. Contag, “Bioluminescent imaging (BLI) to improve and refine traditional murine models of tumor growth and metastasis,” *Clin Exp Metastasis*. vol. 20, pp. 733–744, 2003.
- [44] L. A. Wirtzfeld, G. Wu, M. Bygrave, Y. Yamasaki, H. Sakai, M. Moussa, J. I. Izawa, D. B. Downey, N. M. Greenberg, A. Fenster, J. W. Xuan and J. C. Lacefield, “A new three-dimensional ultrasound microimaging technology for preclinical studies using a transgenic prostate cancer mouse model,” *Cancer Res*. vol. 65, pp. 6337–6345, 2005.
- [45] K. C. Graham, L. A. Wirtzfeld, L. T. MacKenzie, C. O. Postenka, A. C. Groom, I. C. MacDonald, A. Fenster, J. C. Lacefield and A. F. Chambers, “Three-dimensional high-frequency ultrasound imaging for longitudinal evaluation of liver metastases in preclinical models,” *Cancer Res*. vol. 65, pp. 5231–5237, 2005.
- [46] L. A. Wirtzfeld, K. C. Graham, A. C. Groom, I. C. Macdonald, A. F. Chambers, A. Fenster and J. C. Lacefield, “Volume measurement variability in three-dimensional high-frequency ultrasound images of murine liver metastases,” *Phys Med Biol*. vol. 51, pp. 2367–2381, 2006.
- [47] K. Sokolov, J. Aaron, B. Hsu, D. Nida, A. Gillenwater, M. Follen, C. MacAulay, K. Adler-Storthz, B. Korgel, M. Descour, R. Pasqualini, W. Arap, W. Lam and R. Richards-Kortum, “Optical systems for in vivo molecular imaging of cancer,” *Technol Cancer Res Treat*. vol. 2, pp. 491–504, 2003.
- [48] J. R. W. Masters, *Animal Cell Culture 3rd ed*. Academic Press, London, 2000.
- [49] C. Guiot, P. G. Degiorgis, P. P. Delsanto, P. Gabriele and T. S. Deisboeck, “Does

- tumor growth follow a "universal law"?,” *J Theor Biol.* vol. 225, pp. 147–151, 2003.
- [50] L. Bentzen, S. Keiding, M. R. Horsman, T. Grönroos, S. B. Hansen and J. Overgaard, “Assessment of hypoxia in experimental mice tumours by [¹⁸F]fluoromisonidazole PET and pO₂ electrode measurements. Influence of tumour volume and carbogen breathing,” *Acta Oncol.* vol. 41, pp. 304–312, 2002.
- [51] T. F. Massoud and S. S. Gambhir, “Molecular imaging in living subjects: seeing fundamental biological processes in a new light,” *Genes Dev.* vol. 17, pp. 545–580, 2003.
- [52] C. Z. Behm and J. R. Lindner, “Cellular and molecular imaging with targeted contrast ultrasound,” *Ultrasound Q.* vol. 22, pp. 67–72, 2006.
- [53] R. E. Coleman, “FDG imaging,” *Nucl Med Biol.* vol. 27, pp. 689–690, 2000.
- [54] B. I. Choi, J. H. Park, B. H. Kim, S. H. Kim, M. C. Han and C. W. Kim, “Small hepatocellular carcinoma: detection with sonography, computed tomography (CT), angiography and lipiodol-CT,” *Br J Radiol.* vol. 62, pp. 897–903, 1989.
- [55] O. Matsui and Y. Itai, “Diagnosis of primary liver cancer by computed tomography,” *Primary liver cancer in Japan*, Springer-Verlag, Tokyo, pp. 132–147, 1992.
- [56] K. Yanagisawa, F. Moriyasu, T. Miyahara, M. Yuki and H. Iijima, “Phagocytosis of ultrasound contrast agent microbubbles by Kupffer cells,” *Ultrasound Med Biol.* vol. 33, pp.318–325, 2007.
- [57] C. Huang-Wei, A. Bleuzen, P. Bourlier, J. Roumy, A. Bouakaz, L. Pourcelot and F. Tranquart, “Differential diagnosis of focal nodular hyperplasia with quantitative parametric analysis in contrast-enhanced sonography,” *Invest Radiol.* vol. 41, pp. 363–368, 2006.
- [58] T. Albrecht, M. Blomley, L. Bolondi, M. Claudon, J. M. Correas, D. Cosgrove, L.

- Greiner, K. Jäger, N. D. Jong, E. Leen, R. Lencioni, D. Lindsell, A. Martegani, L. Solbiati, L. Thorelius, F. Tranquart, H. P. Weskott, T. Whittingham and EFSUMB Study Group, “Guidelines for the use of contrast agents in ultrasound. January 2004,” *Ultraschall Med.* vol. 25, no. 4, pp. 249–256, 2004.
- [59] B.-K. Wu, C.-C. Li, H.-J. Chen, J.-L. Chang, K.-S. Jeng, C.-K. Chou, M.-T. Hsu and T.-F. Tsai, “Blocking of G1/S transition and cell death in the regenerating liver of Hepatitis B virus X protein transgenic mice,” *Biochem Biophys Res Commun.* vol. 340, pp. 916–928, 2006.
- [60] H. C. Dittrich, G. L. Bales, T. Kuvelas, R. M. Hunt, B. A. McFerran and Y. Greener, “Myocardial contrast echocardiography in experimental coronary artery occlusion with a new intravenously administered contrast agent,” *J Am Soc Echocardiogr.* vol. 8, pp. 465–474, 1995.
- [61] J. L. Cohen, J. Cheirif, D. S. Segar, L. D. Gillam, J. S. Gottdiener, E. Hausnerova and D. E. Bruns, “Improved left ventricular endocardial border delineation and opacification with OPTISON (FS069), a new echocardiographic contrast agent. Results of a phase III Multicenter Trial,” *J Am Coll Cardiol.* vol. 32, pp. 746–752, 1998.
- [62] D. E. Goertz, E. Cherin, A. Needles, R. Karshafian, A. S. Brown, P. N. Burns and F. S. Foster, “High Frequency Nonlinear B-Scan Imaging of Microbubble Contrast Agents,” *IEEE Trans. Ultrason. Ferroelectr. Freq. Control*, vol. 52, no. 1, pp. 65–79, 2005.
- [63] D. E. Goertz, Needles A, Burns PN and F. S. Foster, “High-frequency, nonlinear flow imaging of microbubble contrast agents,” *IEEE Trans. Ultrason. Ferroelectr. Freq. Control*, vol. 52, no. 3, pp. 495–503, 2005.
- [64] M. Kojiro, “Pathology of hepatocellular carcinoma,” Blackwell Pub, Malden, Mass, 2006.

- [65] G. J. Quinlan, G. S. Martin and T. W. Evans, "Albumin: biochemical properties and therapeutic potential," *Hepatology*, vol. 41, no. 6, pp. 1211–1219, 2005.
- [66] W. Mai, L. Barraud, L. Lefrancois, J. Y. Scoazec, S. Guerret, D. Vray, P. Merle, L. Vitvitski-Trepo, C. Trepo and M. F. Janier, "Ultrasound detection of spontaneous hepato-cellular carcinomas in X/myc bitransgenic mice," *Liver Int.* vol. 24, pp. 651–657, 2004.
- [67] O. Couture, P. D. Bevan, E. Cherin, K. Cheung, P. N. Burns and F. S. Foster, "Investigating perfluorohexane particles with high-frequency ultrasound," *Ultrasound Med Biol.* vol. 32, pp. 73–82, 2006.
- [68] B. B. Goldberg, *Ultrasound Contrast Agents*. London: M. Dunitz, 1997.
- [69] B. B. Goldberg, J. B. Liu, and F. Forsberg, "Ultrasound contrast agents: a review," *Ultrasound Med. Biol.*, vol. 20, no. 4, pp. 319–333, 1994.
- [70] P. Frinking, E. Cespedes, J. Kirkhorn, H. Torp and N. Jong, "A new ultrasound contrast imaging approach bases on the combination of multiple imaging pulse and a separate release burst," *IEEE Trans. Ultrason., Ferroelectr., Freq. Control*, vol. 48, pp. 643–645, 2001.
- [71] P. J. Frinking, A. Bouakaz, J. Kirkhorn, F. J. Ten Cate and N. de Jong, "Ultrasound contrast imaging: current and new potential methods," *Ultrasound Med. Biol.*, vol. 26, no. 6, pp. 965–975, 2000.
- [72] N. de Jong, "Improvements in ultrasound contrast agents," *IEEE Eng. Med. Biol. Mag.*, vol. 15, pp.72–82, 1996.
- [73] P. M. Shankar, P. Dala Krishna and V. L. Newhouse, "Advantages of subharmonic over second harmonic backscatter for contrast-to-tissue echo enhancement," *Ultrasound Med. Biol.*, vol. 24, no. 3, pp. 395–399, 1998.
- [74] A. Eller and H. G. Flynn, "Generation of subharmonics of order one-half by bubbles in a sound field," *J. Acoust. Soc. Am.*, vol. 46, no. 3II, pp. 722–727,

1969.

- [75] J. E. Powers, P. N. Burns and J. Souquet, *Imaging Instrumentation for Ultrasound Contrast Agents. Advances in Echo Imaging Using Contrast Enhancement*. Netherlands: Kluwer Academic, pp. 139–170, 1997.
- [76] C.-C. Shen and P.-C. Li, “Pulse-inversion-based fundamental imaging for contrast detection,” *IEEE Trans. Ultrason., Ferroelectr., Freq. Control*, vol. 50, no. 9, pp. 1124–1133, 2003.
- [77] D. H. Simpson and P. N. Burns, “Pulse inversion doppler: a new method for detecting nonlinear echoes from microbubble contrast agents,” *Proc. IEEE Ultrason. Symp.*, pp. 1597–1600, 1997.
- [78] D. H. Simpson, C. T. Chin, and P. N. Burns, “Pulse inversion doppler: a new method for detecting nonlinear echoes from microbubble contrast agents,” *IEEE Trans. Ultrason., Ferroelectr., Freq. Control*, vol. 46, no. 2, pp. 372–382, 1999.
- [79] L. Hoff, “Nonlinear response of sonazoid. numerical simulations of pulse-inversion and sub-harmonics,” *IEEE Ultrason. Symp.*, 2000, pp. 1885–1888.
- [80] K. E. Morgan, M. Averkiou and K. W. Ferrara, “The effect of the phase of transmission on contrast agent echoes,” *IEEE Trans. Ultrason., Ferroelectr., Freq. Control*, vol. 45, pp. 872–875, 1998.
- [81] A. J. Nimunkar and W. J. Tompkins, “EMD-based 60-Hz noise filtering of the ECG,” *Conf. Proc. IEEE Eng. Med. Biol. Soc.*, 2007, pp. 1904–1907.
- [82] A. Torres, J. A. Fiz, R. Jané, J. B. Galdiz, J. Gea and J. Morera, “Application of the empirical mode decomposition method to the analysis of respiratory mechanomyographic signals,” *Conf. Proc. IEEE Eng. Med. Biol. Soc.*, 2007, pp. 1566–1569.
- [83] M. Bennett, S. McLaughlin, T. Anderson and N. McDicken, “Empirical mode

- decomposition and tissue harmonic imaging,” *Ultrasound Med. Biol.*, vol. 31, no. 8, pp. 1051–1061, 2005.
- [84] Y. Zhang, Y. Gao, L. Wang, J. Chen, and X. Shi, “The removal of wall components in Doppler ultrasound signals by using the empirical mode decomposition algorithm,” *IEEE Trans. Biomed. Eng.*, vol. 54, no. 9, pp. 1631–1642, 2007.
- [85] N.-E. Huang, Z. Shen, and S.-R. Long, “A New View of Nonlinear Water Waves—The Hilbert Spectrum,” *Ann. Rev. Fluid Mech.*, vol. 31, pp. 417–457, 1999.
- [86] Z. Wu and N.-E. Huang, “Ensemble Empirical Mode Decomposition: a noise-assisted data analysis method,” *Advances in Adaptive Data Analysis*, vol. 1, no. 1, pp. 1–40, 2008.
- [87] N.-E. Huang, Z. Shen, S.-R. Long, M.-C. Wu, H.-H. Shih, Q. Zheng, N.-C. Yen, C.-C. Tung, and H.-H. Liu, “The empirical mode decomposition and the Hilbert spectrum for nonlinear and nonstationary time series analysis,” *Proc. R. Soc. London.*, vol. 454A, pp. 903–993, 1998.
- [88] G. Rilling, P. Flandrin, and P. Gonçalves, “On empirical mode decomposition and its algorithms,” in *IEEEURASIP Workshop on Nonlinear Signal and Image Processing.*, Grado., Italy, 2003.
- [89] P. Flandrin, G. Rilling, and P. Gonçalves, “Empirical mode decomposition as a filterbank,” *IEEE Signal Proc. Lett.*, vol. 11, pp. 112–114, 2004.
- [90] Z. Wu and N.-E. Huang, “A study of the characteristics of white noise using the empirical mode decomposition method,” *Proc. R. Soc. London.*, vol. 460A, pp. 1597–1611, 2004.
- [91] M. A. Averkiou and M. F. Hamilton, “Modeling of an electrohydraulic lithotripter with the KZK equation,” *J. Acoust. Soc. Am.*, vol. 106, no. 1, pp. 102–112, 1999.

- [92] Y. Li and J. A. Zagzebski, "Computer model for harmonic ultrasound imaging," *IEEE Trans. Ultrason., Ferroelectr., Freq. Control*, vol. 47, no. 5, pp. 1000–1013, 2000.
- [93] W. K. Law, L. A. Frizzell, and F. Dunn, "Determination of the nonlinearity parameter B/A of biological media," *Ultrasound Med. Biol.*, vol. 11, no. 2, pp. 307–318, 1985.
- [94] P.-C. Li, C.-C. Shen, and S.-W. Huang, "Waveform design for ultrasonic pulse-inversion fundamental imaging," *Ultrason. Imaging*, vol. 28, no. 3, pp. 129–143, 2006.
- [95] J. C. Nunes, Y. Bouaoune, E. Dele'chelle, S. Guyot, and Ph. Bunel, "Texture analysis based on the local analysis of bidimensional empirical mode decomposition," *Machine Vision and Applications*, vol. 16, no. 3, pp. 177–188, 2005.
- [96] M. B. Bernini, A. Federico, and G. H. Kaufmann, "Noise reduction in digital speckle pattern interferometry using bidimensional empirical mode decomposition," *Appl. Opt.*, vol. 47, no. 14, pp. 2592–2598, 2008.
- [97] M. Bertolotto, G. Pozzato, L. S. Crocè, F. Nascimben, C. Gasparini, M. A. Cova and C. Tiribelli, "Blood flow changes in hepatocellular carcinoma after the administration of thalidomide assessed by reperfusion kinetics during microbubble infusion: preliminary results," *Invest Radiol*, vol. 41, no. 1, pp. 15–21, 2006.
- [98] Y. Liu, H. Miyoshi and M. Nakamura, "Encapsulated ultrasound microbubbles: therapeutic application in drug/gene delivery," *J Control Release*, vol. 114, no. 1, pp. 89–99, 2006.
- [99] Y. Liu, H. Yang and A. Sakanishi, "Ultrasound: mechanical gene transfer into plant cells by sonoporation," *Biotechnol Adv*, vol. 24, pp. 1–16, 2006.

- [100] H. M. Hudson and R. S. Larkin, "Accelerated image reconstruction using ordered subsets of projection data," *IEEE Trans Med Imaging*, vol. 13, pp. 601–609, 1994.



APPENDIX

Positron Emission and Annihilation

Proton-rich isotopes may decay via positron emission, in which a proton in the nucleus decays to a neutron, a positron and a neutrino. The daughter isotope has an atomic number one less than the parent. Examples of isotopes which undergo decay via positron emission are shown in table A-1.

Table A-1. Properties of commonly used positron emitting radio-isotopes.

Isotope	half-life (min)	Maximum positron energy (MeV)	Positron range in water (FWHM in mm)	Production method
^{11}C	20.3	0.96	1.1	cyclotron
^{13}N	9.97	1.19	1.4	cyclotron
^{15}O	2.03	1.70	1.5	cyclotron
^{18}F	109.8	0.64	1.0	cyclotron
^{68}Ga	67.8	1.89	1.7	generator
^{82}Rb	1.26	3.15	1.7	generator

MicroPET Image Processing

Filtered Back Projection (FBP) algorithm is based on a Fourier Transform algorithm and is extremely fast, but the reconstructed image may suffer from annoying streak artifacts. FBP is straight-forward to implement but does have the property of amplifying noise in the signal. Recently, considerable interest has been shown in iterative reconstruction schema, such as the Ordered Subsets - Expectation Maximisation (OSEM) algorithm [100], which possess different noise properties to FBP. Moreover, Ordered Subsets Expectation Maximization (OS-EM) algorithm depresses the noise problem. In this section, the microPET image reconstruction algorithm used in this dissertation, OSEM and FBP, will be illustrated.

A-1 Ordered Subsets Expectation Maximization (OS-EM)

With OS-EM, the projection data is grouped in ordered subsets. The OS level is defined as the number of these subsets. The standard EM algorithm is then applied to each of the subsets in turn, using the rows of the design matrix corresponding to these ray sums. The resulting reconstruction becomes the starting value for use with the next subset. An iteration of OS-EM was defined as a single pass through all the specified subsets. Further iterations may be performed by passing through the same the same ordered subsets, using as a starting point the reconstruction provided by the previous iteration. With mutually exclusive subsets, each OS-EM iteration will have a similar computation time to one standard EM iteration. Photon recordings on gamma cameras are binned to provide counts y_t on detectors indexed by t . These recordings are the result of emitter activity (modeled as a Poisson point process in equation A-1)

within a region.

$$\Pr(y_i | \lambda) = \frac{e^{-\sum_j P_{ij} \lambda_j} (\sum_j P_{ij} \lambda_j)^{y_i}}{y_i!} \quad \text{Eq. (A-1)}$$

Let S_1, S_2, \dots, S_n denote the chosen detector subsets in the order selected. The algorithm is then as follows:

$$\lambda_j^{k+1} = \frac{1}{\sum_{i \in S_j} P_{ij}} \lambda_j^k \sum_{i \in S_j} P_{ij} \frac{y_i}{\sum_{m=1}^B P_{im} \lambda_m^k} \quad \text{Eq. (A-2)}$$

Currently, iterative algorithms based on OSEM have been widely deployed in clinical practice for providing high-quality PET imaging.

A-2 Filtered Back Projection (FBP)

An estimate of the original source distribution may be obtained by a process known as back-projection. In this process, the magnitude of each value in a projection is added to every point in image space corresponding to the relevant line of integration in object space. Back-projections for a single point-source are shown in Fig. A-1. When a small number of projections are used, the resultant image contains star-shaped artefacts.

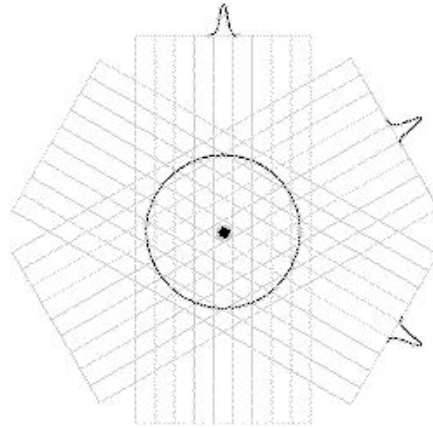


Fig. A-1. Projections generated from a single central point source (3 projections shown).

The filtered back projection algorithm can therefore be thought of as a three step process:

1. Finding the Fourier Transform (FT) in 1D of the projections.
2. Finding the filtered projections. This essentially means multiplying the results of step 1. with a response function in the frequency domain, and then finding the inverse Fourier Transform (IFFT). This step is essentially the same as carrying out convolution in the time domain. It can be represented mathematically as

$$Q_{\theta}(t) = \int_{-\infty}^{\infty} S_{\theta}(w) |w| e^{i2\pi wt} dw \quad \text{Eq. (A-3)}$$

3. Finding the back projections. This step is the smearing of the filtered projections back on to the object, and is mathematically represented by

$$f(x, y) = \int_0^{\pi} Q_{\theta}(x \cos \theta + y \sin \theta) d\theta \quad \text{Eq. (A-4)}$$

These three steps represent the filtered back projection algorithm.

Histology of Liver Focal Lesion in HBx Transgenic Mice

This section supplies the histology results in chapter 4. Figure A-2(d) is the histology result of mouse 6 (Fig. 4-9). Figure A-3(d) shows the histology result of mouse 9 (Fig. 4-10).

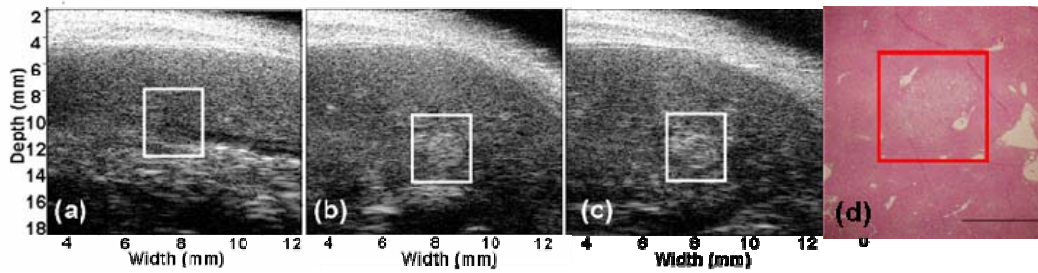


Fig. A-2. HCC lesion in mouse 6 before contrast injection (a) and the hyper-enhancing feature during the arterial phase (b). Panel (c) shows the hypo-enhancing feature at 30 minutes after contrast injection. (d) shows the histology result.

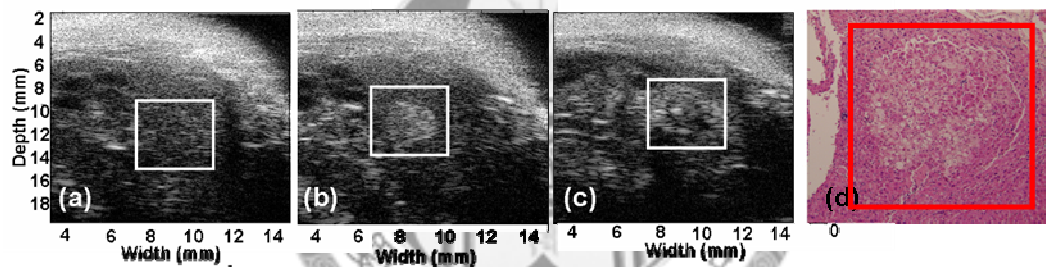


Fig. A-3. The hypervascular metastases lesion in mouse 9 before contrast injection is shown in panel (a). Panel (b) shows the hyper-enhancing, rim enhancing, and non-enhancing (necrosis) features during the arterial phase. Panel (c) is the hypo-enhancing feature at 30 minutes after contrast injection. (d) shows the histology result.

PUBLICATION LIST

Journal Articles

- [1] Ai-Ho Liao, Che-Chou Shen and Pai-Chi Li, “Contrast improvement in ultrasound nonlinear imaging using EEMD”. (Manuscript)
- [2] Ai-Ho Liao, Ya-Chien Cheng, Chien-Hsiu Weng, Wei-Hsiang Lin, Ting-Fen Tsai, Shiou-Hwei Yeh, Wen-Chun Yeh and Pai-Chi Li, Characterization of hepatocellular carcinomas with contrast-enhanced 40 MHz ultrasound imaging in hepatitis B virus X transgenic mice: a feasibility study”. (Revised)
- [3] Ai-Ho Liao, Jeng-Jong Hwang, Chen-Han Li, Wen-Fang Cheng and Pai-Chi Li, “Noninvasive Small-Animal-Tumor Imaging Combining High-Frequency Ultrasound and MicroPET”, *Ultrasonic Imaging* 29, 182-194, 2007.
- [4] Ai-Ho Liao, Li-Yen Chen, Wen-Fang Cheng and Pai-Chi Li, “A Three-Dimensional Registration Method for microUS/microPET Multimodality Small-Animal Imaging”, *Ultrasonic Imaging* 29(3), 155-166, 2007.
- [5] Hsin-Ell Wang, Ai-Ho Liao, Win-Ping Deng, Pi-Fang Chang, Jyh-Cheng Chen, Fu-Du Chen, Ren-Shen Liu, Jin-Shin Lee and Jeng-Jong Hwang, “Evaluation of 4-Borono-2-[18F]Fluoro-L-Phenylalanine –Fructose as a Probe for Boron Neutron Capture Therapy in a Glioma-Bearing Rat Model”, *Journal of Nuclear Medicine* 45, 302-308, 2004.

Conference Papers

- [1] Ai-Ho Liao, Che-Chou Shen and Pai-Chi Li, “Contrast improvement in ultrasound harmonic imaging using EMD”, *Symposium of Annual Conference of the Biomedical Engineering Society*, Tao-Yuan, Taiwan, R.O.C., December 12-13 2008.

- [2] Ai-Ho Liao, Ya-Chien, Cheng, Shiou-Hwei Yeh, Pai-Chi Li and Wen-Chun Yeh, "Identification and Detection Hepatocellular Carcinomas with Contrast Enhanced 40 MHz Ultrasound in Hepatitis B Virus X Protein Transgenic Mice", *Symposium of Annual Conference of the Biomedical Engineering Society*, Taichung, Taiwan, R.O.C., December 14-15 2007.
- [3] Jia-Ling Ruan, Po-Wen Cheng, Ai-Ho Liao, Chen-Wei Wei, Yi-Chung Chang, and P.-C. Li, "Assessment of Tumor Angiogenesis by Ultrasonic Molecular Imaging", *Symposium of Annual Conference of the Biomedical Engineering Society*, Taichung, Taiwan, R.O.C., December 14-15 2007.
- [4] Ai-Ho Liao, Ya-Chien Cheng, Shiou-Hwei Yeh, and Pai-Chi Li, "Identification of Hepatocellular Carcinomas with Contrast Enhanced 40 MHz Ultrasound in Hepatitis B Virus X Protein Transgenic Mice", *Ultrasonics Symposium*, New York, U.S.A., October 28-31, 2007.
- [5] Ai-Ho Liao, Li-Yen Chen, Wen-Fang Cheng and Pai-Chi Li, "A Three-dimensional Registration Method Combing MicroUS/microPET for Small Animal Tumors Imaging", *Symposium of Annual Conference of the Biomedical Engineering Society*, Taipei, Taiwan, R.O.C., December 15-16 2006.
- [6] Li-Yen Chen, Ai-Ho Liao, and Pai-Chi Li, "Image Registration for US/PET Multi-modality Small Animal Imaging", *Symposium of Annual Conference of the Biomedical Engineering Society*, Taipei, Taiwan, R.O.C., December 15-16 2006.
- [7] Ai-Ho Liao, Li-Yen Chen, Wen-Fang Cheng and Pai-Chi Li, A 3D Registration Method for US/PET Multi-Modality Small Animal Tumor Imaging, *Ultrasonics Symposium*, Vancouver, Canada, October 3-6, 2006.
- [8] Ai-Ho Liao, Chen-Han Li, Li-Yen Chen, Wen-Fang Cheng and Pai-Chi Li, "Non-invasive Small Animal Tumor Growth Imaging: High Frequency Ultrasound VS. MicroPET", *Symposium of Annual Conference of the Biomedical Engineering*

Society, Taoyuan, Taiwan, R.O.C., December 17-18 2005.

- [9] Li-Yen Chen, Ai-Ho Liao, and P.-C. Li, “Image registration for US/PET multi-modality small animal imaging”, *Symposium of Annual Conference of the Biomedical Engineering Society*, Taoyuan, Taiwan, R.O.C., December 17-18 2005.
- [10] Chen-Han Li, Ai-Ho Liao, Ja-An Ho and Pai-Chi Li, “Ultrasonic Pulse-Inversion Fundamental Imaging with Liposome Microbubbles at 25-50 MHz”, *Ultrasonics Symposium*, Rotterdam, Netherlands, September 18-21, 2005.
- [11] Pai-Chi Li, Chen-Han Li, Ai-Ho Liao and Ja-An Ho, “Pulse Inversion Fundamental Imaging for Ultrasonic Small Animal Molecular Imaging”, *The Fourth Annual Meeting of the Society for Molecular Imaging*, Cologne, Germany, September 7-10, 2005.
- [12] Ai-Ho Liao, Chen-Han Li, Wen-Fang Cheng and Pai-Chi Li, “Non-invasive Imaging of Small-animal Tumors: High-frequency Ultrasound vs. MicroPET”, *The 27th Annual International Conference of the IEEE Engineering in Medicine and Biology Society (EMBS)*, Shanghai, China, Sept. 1-4, 2005.
- [13] Ai-Ho Liao, Wen-Fang Cheng and Pai-Chi Li, “Multi-modality Small-animal Imaging: Combining High Frequency Ultrasound and MicroPET”, *Symposium of Annual Conference of the Biomedical Engineering Society*, Tainan, Taiwan, R.O.C., December 17-18 2004.
- [14] Ai-Ho Liao, Fong-In Chou, Fu-Du Chen and Jeng Jong Hwang, “Biodistribution of Phenylboric Acid Derivative Entrapped Lipiodol in Hepatoma-bearing Rat Model”, *American Association for Cancer Research (AACR)*, Toronto, Canada, April. 5-9, 2003.
- [15] Hsin-Ell Wang, Ai-Ho Liao, Pi-Fang Chang, Fu-Du Chen, Jyh-Cheng Chen,

Jang-Jong Hwang, Ho-Men Yu and Ren-Shen Liu, “Biological Characterization of 4-Borono-2-[¹⁸F]Fluoro-L-Phenylalanine-Fructose in Glioma-bearing Model”, *Research and Development in Neutron Capture Therapy, Essen, Germany, Sept. 8-13, 2002.*



